Drone-Based Optical Soiling Measurements for Photovoltaic Power Plants

Drohnenbasierte optische Verschmutzungsmessungen für Photovoltaik Kraftwerke

Von der Fakultät für Maschinenwesen der Rheinisch-Westfälischen Technischen Hochschule Aachen zur Erlangung des akademischen Grades eines Doktors der Naturwissenschaften genehmigte Dissertation

vorgelegt von

Peter Winkel

Berichter:

Univ.-Prof. Dr.-Ing. Robert Pitz-Paal Prof. Dr. rer. nat. Carsten Agert

Tag der mündlichen Prüfung: 4. Juli 2025

"Diese Dissertation ist auf den Internetseiten der Universitätsbibliothek online verfügbar."

Abstract

The monitoring of PV parks is important to optimize their operation in terms of yield and levelized cost of electricity. Defective modules and inverters must be detected and replaced promptly. The influence of environmental factors such as soiling must be kept in mind, as these can accelerate the degradation of the system. Every maintenance measure is associated with costs. For cleaning, these are working time, water consumption, and money. Measuring the electrical loss caused by soiling is an important parameter for the development of optimized cleaning strategies.

Even before this dissertation, there are several ways to measure the electrical power loss caused by soiling. The power of the park can be compared with the modeled power, considering operational conditions such as irradiance, temperature, and other sources of efficiency reduction. However, these other sources of efficiency reductions, i.e. aging are typically not known.

To obtain the most accurate and spatially resolved image of the soiling, it makes sense to develop a camera-based measurement method. This work aims to develop this camera-based method that can estimate the electrical losses of a PV park from drone images. The first method refers to the soiling type of mineral dust. The method is calibrated by taking several images of a clean PV module and a soiled module. It is then possible to evaluate third images. In the validations of the method, an RMSE of 0.93% (absolute) was achieved.

A second method was developed to evaluate coarse soiling such as leaves and bird droppings. Deep learning is used to first detect soiling and then segment it. By estimating the transmittances of the different types of soiling, it is then possible to estimate the electrical power loss caused. In the tests carried out on the method, a deviation of less than 1% absolute was always achieved, with an absolute soiling loss of approx. 15%.

Furthermore, an electrothermal model was developed that can determine the temperature of a PV module with cell resolution. In particular, it is possible to estimate which soiling pattern can lead to a hotspot and how high the corresponding hotspot temperature is. In addition, the model can determine the electrical mismatch losses of an inhomogeneously soiled module. The model can also be used to differentiate between soiling-based and defect-based hotspots. In the cases considered, this was always successful. The electrical power could be determined relatively accurately with an RMSE of 2.1 W. In the case of a clean module, the temperature could be determined with an RMSE of 2.6 K.

All in all, this thesis presents new methods for the measurement of soiling in PV parks. Advantages compared to the literature are in particular the high accuracy, the capability of analyzing various kinds of soiling, the spatial resolution, and the practicability that comes with the usage of drones.

Kurzfassung

Um den Betrieb von PV Parks bezüglich bezüglich des Ertrags und der Stromgestehungskosten zu optimieren ist ein gezieltes Monitoring wichtig. Defekte Module und Wechselrichter müssen zeitnah erkannt und ersetzt werden. Der Einfluss von Umweltfaktoren wie z.B. Verschmutzung muss im Auge behalten werden, da diese die Degradierung der Anlage beschleunigen können. Jede Instandhaltungsmaßnahme ist mit Kosten verbunden. Für eine Reinigung sind dies Arbeitszeit, Wasserverbrauch und Geld. Für die Entwicklung optimierter Reinigungsstrategien ist die Messung des durch Verschmutzung hervorgerufenen, elektrischen Verlustes ist dabei ein wichtiger Parameter.

Bereits vor dieser Dissertation gibt es einige Möglichkeit den durch Verschmutzung hervorgerufenen elektrischen Leistungsverlust zu messen. Die Leistung des Parks kann mit der modellierten Leistung verglichen werden, wobei Betriebsbedingungen wie Bestrahlungsstärke, Temperatur und andere Quellen für Effizienzminderungen berücksichtigt werden. Diese anderen Quellen für Effizienzminderungen, z.B. Alterung, sind jedoch in der Regel nicht bekannt.

Um ein möglichst genaues und räumlich aufgelöstes Bild von der Verschmutzung zu bekommen ist es sinnvoll eine kamerabasierte Messmethode zu entwickeln.

Das Ziel dieser Arbeit ist die Entwicklung einer solchen kamerabasierten Methode, welche die elektrischen Verluste eines PV Parks aus Drohnenbildern abschätzen kann. Dabei bezieht sich die erste Methode auf den Verschmutzungstyp Mineralstaub. Kalibriert wird die Methode durch Aufnahme einiger Bilder eines sauberen PV Moduls und eines verschmutzten Moduls. Im Anschluss ist die Auswertung dritter Bilder möglich. In den durchgeführten Validierungen der Methode wurde ein RMSE von 0.93% (absolut) erzielt.

Eine zweite Methode wurde entwickelt, um grobe Verschmutzungen wie Blätter und Vogelkot zu auszuwerten. Dabei wird Deep Learning benutzt, um zunächst Verschmutzungen zu detektieren und im Anschluss zu segmentieren. Durch Abschätzung der Transmittanzen der verschiedenen Verschmutzungstypen ist es dann möglich den hervorgerufenen elektrischen Leistungsverlust abzuschätzen. In den durchgeführten Tests der Methode konnte stets eine Abweichung von weniger als 1% absolut erzielt werden, bei einem absoluten Verschmutzungsverlust von ca. 15%.

Des Weiteren wurde ein elektrothermisches Model entwickelt, welches die Temperatur eines PV Moduls mit Zellauflösung bestimmen kann. Insbesondere kann abgeschätzt werden, welches Verschmutzungsmuster zu einem Hotspot führen kann und wie hoch die entsprechende Hotspottemperatur ist. Zudem kann das Model die elektrischen Mismatch Verluste eines inhomogen verschmutzten Moduls bestimmen. Das Model kann auch für die Unterscheidung von verschmutzungsbasierten und defektbasierten Hotspots genutzt werden. In den betrachteten Fällen ist dies immer gelungen. Die elektrische Leistung konnte bestimmt werden mit einem RMSE von 2.1 W und die Temperatur eines sauberen Moduls mit einem RMSE von 2.6 K.

Insgesamt werden in dieser Arbeit neue Methoden zur Messung von Verschmutzungen in PV-Parks vorgestellt. Die Vorteile gegenüber der Literatur liegen insbesondere in der hohen Genauigkeit, der Fähigkeit, verschiedene Arten von Verschmutzungen zu analysieren, der räumlichen Auflösung und der Praktikabilität, die durch den Einsatz von Drohnen entsteht.

Acknowledgements

This dissertation was prepared at the Institute of Solar Research of the German Aerospace Center (Deutsches Zentrum fur Luft- und Raumfahrt e.V., DLR) within the department Qualification. The work was carried out at DLR's offices on CIEMAT's (Centro de Investigaciones Energéticas, Medioambientales y Tecnológicas) Plataforma Solar de Almería. First of all, I would like to thank my adviser Prof. Dr. Robert Pitz-Paal, for giving me the opportunity to write my thesis. I highly appreciate his wise guidance for my work and his confidence in my research.

My sincere gratitude goes to my supervisor Dr. Stefan Wilbert. He encouraged me to work on a doctoral thesis with a strong physical emphasis. I am grateful for the trust he placed in me as a researcher and as a person. His continuous very methodical professional support, fruitful discussions, and thorough proofreading were essential for the preparation of this thesis.

I would also like to thank Dr. Fabian Wolfertstetter for his support during the first year of my thesis. His help was especially important for the conduction of all experiments.

Highlighted should also be the work of Niels Algner who provided great help by flying the drones with me and Dr. Julian Krauth who shared great knowledge in photogrammetry.

I also want to mention Dr. Bijan Nouri who is a great colleague in terms of professional work but also as a person with fantastic humor and very interesting world views.

Crucial was also the daily manual work of David Muruve without whom any operation of DLR in Almerá would be impossible.

My special thanks go to my parents and my brothers. They have constantly taken an important role model function in my life.

Contents

Al	bstrac	et		iii
Κι	urzfa	ssung		v
A	cknov	wledge	ments	vii
1	Intr	oductio	on	1
2	Stat	e of the	e Art	5
	2.1	Soilin	g of PV Plants	5
	2.2	Soilin	g Measurements	6
		2.2.1	Soiling Measurements With Device Pairs	7
		2.2.2	Optical Soiling Sensors	9
		2.2.3	Optical Soiling Sensors With Internal Light Source	
		2.2.4	Microscopy Soiling Measurements	10
	2.3	Image	e-based PV Monitoring Techniques	11
		2.3.1	RGB Imaging Techniques for Soiling Monitoring	11
		2.3.2	Electroluminescence Imaging Techniques for PV Monitoring	13
		2.3.3	Infrared Imaging Techniques for PV Monitoring	13
	2.4	Electr	ical Modeling of PV Modules	15
	2.5	Thern	nal Modeling of PV Modules	16
		2.5.1	Modeling of Clean, Intact Modules	
		2.5.2	Modeling of Hotspots	
	2.6	Statist	tics	19
3		•	Methods	21
	3.1		stbench	
	3.2	Came	ra Systems	24
		3.2.1	Gamma Correction	24
		3.2.2	Flat Field Correction	24
		3.2.3	Photogrammetry	24
4	Dro	ne-Bas	ed Optical Measurement of Dust-Like Soiling	27
	4.1	Optica	al Measurement Principle	27
	4.2	Optica	al Measurements Theory	
		4.2.1	Relation of the RGB Values to the Incoming Radiation	28
		4.2.2	Contributions to the Camera Signal According to the Interaction	
			at the Module's Surface	29
		4.2.3	Comparing the Camera Equation for the Clean and Soiled Case	30
		4.2.4	Analyze Different Scattering Pathways	32
	4.3	Calibi	ration Measurements	37
		4.3.1	Determination of Expected Background Signal Corresponding	
			to a Clean PV Module	37

		4.3.2	Determination of the Scattering Behavior	37
		4.3.3	Calculation of Soiling Loss	38
	4.4	Measu	rement Procedure and Data Processing	39
		4.4.1	Measurement Procedure	39
		4.4.2	Data Processing	39
	4.5	Result	s and Discussion	40
		4.5.1	First Campaign	40
		4.5.2	Second Campaign	43
		4.5.3	Third Campaign	44
		4.5.4	Summary	46
	4.6	Visual	ization of the Calibration Functions	48
		4.6.1	Clean Background Calibration	48
		4.6.2	Scattering Calibration	49
	4.7	Concl	usions	52
5	Ont	ical Ma	easurement of Spatially Inhomogeneous Soiling	53
J	5.1		odology	53 54
	5.1	5.1.1	Soiling Detection and Soiling Segmentation with YOLO and SAM	
		5.1.2	Classification of Different Soiling Types	55
		5.1.3	Determination of Cell-Resolved Transmittances	56
		5.1.4	Soiling Loss Calculation on Module Level	59
	5.2		plary Test of the Developed Method	60
	5.3	-	nary and Outlook	62
	0.0	Carrin	my mid outlook	~ <u>~</u>
6	Elec	trother	mal Modeling of Soiled PV Modules	63
	6.1		ical Model	65
	6.2	Therm	nal Model	66
		6.2.1	Material Properties of Layers	69
		6.2.2	Combination of Electrical and Thermal Model	70
		6.2.3	Non-Linear Set of Equations	71
		6.2.4	Thermal Inertia	71
	6.3	Result	S	73
		6.3.1	Experiments with Clean Modules	
		6.3.2	Experiments with Soiled Modules	75
	6.4	Concl	usions and Outlook	81
7	Sun	nmary a	and Outlook	83
A	Elec	trical R	Reference Measurements	85
	A.1	First C	Campaign, Dust-Like Soiling	86
			d Campaign, Dust-Like Soiling	90
			Campaign, Dust-Like Soiling	92
			iment with Inhomogeneous Soiling	94
В	Mea	sureme	ent Flights for the Measurement of Dust	97
_			Campaign	97
		B.1.1		97
		B.1.2		98
		B.1.3	Fourth Flight	99
	B.2		d Campaign	
	~	B.2.1	<u>. </u>	
		B.2.2	Third Flight	

C Further Validations of the Electrothermal Model	103
Bibliography	105

xi

List of Figures

2.1	Equivalent circuit diagram of the single-diode model	15
3.1	PV Testbench used for most experiments with this work. There are twelve modules in total, six different types, two of each type. There are six photogrammetry targets mounted on the setup. Multiple additional targets are placed around the setup. The numbers refer to an internal numbering. This numbering will be used in the following Chapters to clearly identify each module.	21
4.1	Sketch to describe the geometry of the measurement method. Shown are the sun position, a direct sun ray towards the PV module, the drone position, and the module position including its normal vector $\overrightarrow{n_{module}}$. Also, one exemplary ray contributing to the diffuse radiation received that is received by the module is shown. Additionally, the direct sun reflex is shown together with the reflex of the diffuse radiation of one	
4.2	Sketch to describe the scattering pathways relevant to the measurement method. The cover glass is shown as a gray surface with the soiling layer on top (dotted brown line) and the PV cell below (straight blue line). Shown is the direct radiation coming from the sun as a straight yellow arrow. The black arrow with a straight line shows in which direction the light leaves if it is scattered (camera direction). The dashed yellow or black arrows show the direction relative to which the scattering angle is defined. In the lower two sub-figures, the yellow	28
4.3	dashed arrow corresponds to the direct sun reflex	34 40
4.4	Results of the first flight performed on the 8 April 2022. The color marks the calculated soiling loss. The lower right module (1) was used as the clean calibration module while the upper right (2) was used as soiled reference module. The upper numbers label the modules. The number in the middle states the optically measured soiling loss using	
	the drone images while the lower number is the electrical reference loss.	41
4.5	Optically calculated soiling loss for every image of every module against the electrically measured reference soiling loss. The standard deviations for the soiling loss on module level for modules 1 to 4 are 0.14%, 0.22%, 0.20%, and 0.18%, respectively. The results belong to the	
1.		42
4.6	This figure show the setup during the second campaign	43

4.7	Result plot of the first measurement flight of the second campaign. The lower right module was chosen to be the clean reference module while the lower left module was chosen to be the soiled reference module. The upper numbers label the modules. The number in the middle states the optically measured soiling loss while the lower number is	
	the electrical reference loss.	43
4.8 4.9	This figure show shows the setup during the third campaign Result plot of the first measurement flight of the third campaign. The lower right module was chosen to be the clean reference module while the upper right module was chosen to be the soiled reference module.	44
	In this campaign, the modules were soiled artificially with gypsum. The artificial soiling was not as homogeneously distributed as was the case for the previous campaigns with natural soiling. The upper numbers label the modules. The number in the middle states the	
	optically measured soiling loss while the lower number is the electrical reference loss.	45
4.10	Optically measured soiling losses based on the images plotted against the electrically measured reference soiling losses for several modules	43
	and the three measurement campaigns performed. For some campaigns and modules, several identical markers are seen referring to different flights within the same campaign.	46
4.11	Clean background calibration for the first measurement flight of the first campaign. The x-axis shows the angle between camera and sun reflex vector $\theta_{cam,sunrefl}$ while the y-axis shows the angle between camera vector and panel normal vector α_{cam} . The calibration function is a polynomial of second order of the above-mentioned angles. The cali-	10
4.12	bration function gives basically the expected brightness normalized to GTI and exposure time, which explains the unit	48
	to create the clean background calibration and the expected values according to the fit.	49
4.13	Scattering calibration of the first flight of the first campaign. The x-axis shows the angle between camera vector and sun reflex vector $\theta_{cam,sunrefl}$ while the y-axis shows the angle between camera vector	
	and sun vector $\theta_{cam,sun}$. The color bar shows the scattering calibration parameter c_{scat} .	50
4.14	Relative difference between the discrete scattering values and the scattering values expected according to the scattering calibration function.	50
5.1	Flow chart illustrating the work flow of the proposed method. The two steps in the box are performed by the method developed by (Beuter,	Γ4
5.2	2023)	54
5.3	blue and detected stickers are colored red	56
	orthoimage on the left. Detected leaves are colored blue and detected stickers are colored red.	57

5.4	Calibration of the reference cells. Ratio of the GTIs of the reference cells over time. Averaging leads to a calibration factor of 0.9989. The increase of the calibration factor over time is caused by a small tilt of	
5.5	the reference cells towards each other. Transmittance of the bird droppings over time. Averaging leads to a transmittance of 3%. The calibration factor is already considered. The change over time is caused by a tilt of the reference cells towards each	57
5.6	other. Transmittance of the leaves over time. Averaging leads to a transmittance of 15%. The calibration factor is already considered. The measured transmittance slightly changes over time as the reference	58
5.7	cells are slightly tilted towards each other	58
5.8	losses. Scatter plot of the cell-resoled transmittances; referring to module 4 (left in Figure 5.7). Only the cells of the right sub-string are shown. Cell number starts at the upper left corner and is then counted downward. After finishing the first column, counting is continued in the second column.	60
6.1	Left: RGB image of a defective module. On the RGB image it appears clean and a potential hotspot is not observed. Right: IR image of the defective module. The IR image clearly shows 4 hot cells. By having access to both the RGB and the IR image one can conclude that the module is defective. One string, the third and fourth column from the right, is bypassed. The temperature is slightly increased compared to	
6.2	the other cells (except of the hotspots). Electroluminescence (EL) image of the above-mentioned module (see Figure 6.1). There are multiple cracks visible. This module is likely to show one or more hot cells when operated. One string is bypassed and therefore shows no electroluminescence signal. This EL image has been provided by CIEMAT (Centro de Investigaciones Energéticas,	63
6.3	Medioambientales y Tecnológicas)	64
6.4	(hotspot). Sketch describing the linkage between the electrical and the thermal model combining it to the electrothermal model. The cell temperature is iteratively fed into both models. Both, the electrical and the thermal model require an initial estimate of the temperature and then refine the temperature in an iterative way. The model stops after three iterations each as the temperature and the power do not change noticeably	64
6.5	afterwards	71
	are illustrated	72

6.6	Comparison of the developed model with the measured temperature and the thermal models from literature discussed in Chapter 2 for the 26 th and the 27 th of April 2023.	74
6.7	In blue, spectral transmittance against wavelength of the used artificial soiling. In red, solar spectrum used for averaging the spectral transmittance. In dark gray, spectral response of a mono-Si solar cell. Weighted	
6.8	averaging results in an effective transmittance of 44.6%. Measured and simulated IV curves. Exemplary, one day and 4 timestamps are chosen. 12 th of March 2024. Upper left: 10:00, upper right 12:00, lower left 14:00, and lower right 16:00. The small circles indicate the maximum point points.	75 76
6.9	Measured and simulated electrical powers for the entire time considered for the soiled experiment. Each sub-figure shows the data for one day.	77
6.10		,,
6.11	10 th of May 2024, between 10:00 and 16:00	78
6.12	12 th of May 2024, between 10:00 and 16:00. The left sub-figure of each column shows the most important meteorological data determining the temperature. The right sub-figure of each column compares the measured and hotspot temperature simulated by the developed model. Additionally, the temperature of a clean cell, a non-hotspot cell, is shown in dark gray. Data shown for the 13 th and 14 th of May 2024, between 10:00 and 16:00.	79 80
A.1	Calibration factor for the electrical calculation of the reference soiling loss for the first campaign measured with clean devices (reference day). The powers of modules 2, 3, and 4 are divided by the GTI measured by a reference cell. The derived calibration factors are 0.228 m ² , 0.2254 m ² ,	00
A.2	and 0.3248 m ² for modules 2, 3, and 4, respectively	87
	that, for the measurement day data between 13:23 and 13:27 is neglected.	88

A.3	Soiling loss for modules 2, 3, and 4 during the first campaign. The module powers are divided by the GTI and then divided by the previously determined calibration factor. The averaged soiling losses of modules 2, 3, and 4 are 4.2%, 3.7%, and 4.1%, respectively. Data between 13:22 and 13:27 were excluded as the reference cell was shaded	
A.4	by the scientists	89
A.5	modules 2, 3, and 4, respectively. Calculation of the soiling loss for modules 2, 3, and 4 during the second campaign. The module powers are divided by the power of module 1 and then divided by the previously determined calibration factor. The calculated soiling losses are 1.25%, 2.09%, and 3.75% for modules 2, 3,	90
A.6	and 4, respectively	91
A.7	modules 2, 3, and 4, respectively	92 93
	factor is 1.006 for module 1 and 1.021 for module 4. <i>Module power clean</i> refers to the power of module 2 which has been cleaned	93
A.9	Soiling loss of both modules of interest. The calculated soiling loss is 13.9% for module 1 and 14.1% for module 4	95
B.1	Result plot of the second measurement flight of the first campaign. The lower right module was chosen to be the clean reference module while the upper right module was chosen to be the soiled reference module. The upper numbers label the modules. The number in the middle states the optically measured soiling loss while the lower number is the electrical reference loss.	97
B.2	Result plot of the third measurement flight of the first campaign. The lower right module was chosen to be the clean reference module while the upper right module was chosen to be the soiled reference module. The upper numbers label the modules. The number in the middle states the optically measured soiling loss while the lower number is the electrical reference loss.	98

B.3	Result plot of the fourth measurement flight of the first campaign. The	
	lower right module was chosen to be the clean reference module while	
	the upper right module was chosen to be the soiled reference module.	
	The lower left module was cleaned before the flight which explains the	
	different soiling loss compared to the other three flights of the same	
	campaign. The upper numbers label the modules. The number in	
	the middle states the optically measured soiling loss while the lower	
	number is the electrical reference loss	. 99
B.4	Result plot of the second measurement flight of the second campaign.	
	The lower right module was chosen to be the clean reference module	
	while the lower left module was chosen to be the soiled reference mod-	
	ule. The upper numbers label the modules. The number in the middle	
	states the optically measured soiling loss while the lower number is	
	the electrical reference loss.	. 100
B.5	Result plot of the third measurement flight of the second campaign.	
	The lower right module was chosen to be the clean reference module	
	while the lower left module was chosen to be the soiled reference	
	module. The left sub-string of the upper left module was cleaned	
	before the flight (two columns of cells cleaned). The upper numbers	
	label the modules. The number in the middle states the optically	
	measured soiling loss while the lower number is the electrical reference	
	loss	. 101
C.1	Comparison of the developed model with the measured temperature	
C.1	and the thermal models from literature discussed in Chapter 2 for the	
	28 th and the 29 th of April 2023	103
C_2	Comparison of the developed model with the measured temperature	. 105
C.2	and the thermal models from literature discussed in Chapter 2 for the	
	30 th of April and the 1 st of May 2023	104
	of ripin and the i or may 2020	. 101

List of Tables

3.1	testbench. In the following, mainly the Axitec modules are used. They are highlighted in Figure 3.1. Table listing the different quantities measured at the testbench and the meteorology station close to the testbench.	22 23
4.1 4.2	Explanation of the different scattering angles and pathways Comparison of the different scattering angles	33 33
5.1	Comparing the electrically and optically measured soiling loss. The calculation of the electrical reference soiling loss is shown in Appendix A.4.	61
6.1	Summary of the simulation parameters. Breakdown parameters taken from (Restrepo-Cuestas and Montano, 2024; Jessen et al., 2018). The parameters are corrected for e.g. aging.	65
6.2	Overview of the origin of the known parameters for the thermal model. [1]: (Zhou et al., 2015), [2]: (Pfreundt et al., 2019), [3]: (Hoang et al., 2014), [4]: (Priyadarshini and Sharma, 2016), [5]: (Notton et al., 2005), [6]: (Lee et al., 2008), [7]: (Wolf, Pohl, and Brendel, 2005), [8]: (Module data sheet 2024), [9]: (National Oceanic and Atmospheric Administra-	
6.3	tion, 1976)	67
6.4	2015), [8]: (Priyadarshini and Sharma, 2016), [9]: (Pfreundt et al., 2019) Summary of the error metrics for the different thermal models, both from literature and the developed model. This table refers to the clean	69
	state. The data refers to the entire test period consisting of six days.	73

List of Abbreviations

AI Artificial Intelligence AOI Angle of incidence CdTe Cadmium telluride

CIEMAT Centro de Investigaciones Energéticas, Medioambientales y Tecnológicas

CMOS Complementary Metal-Oxide-Semiconductor

CNN Convolutional Neural Network
CSP Concentrating Solar Power

DLR Deutsches Zentrum für Luft- und Raumfahrt / German Aerospace Center

EL Electroluminescence

IR Infrared

IV (curve) current-voltage (curve)
LED Light emitting diode
MAE Mean absolute error
MBE Mean bias error

MPP Maximum Power Point

NOCT Normal operating condition temperature
OSM Optical Soiling Measurement sensor
PERC Passivated emitter and rear cell
PSA Plataforma Solar de Almería

Pt Platinum PV Photovoltaics

QRNN Quantile Regression Neural Network

RGB Red Green Blue (image)
RMSE Root mean square error
SAM Segment Anything Model

Si Silicon

mono-Si mono-crystalline silicon poly-Si poly-crystalline silicon STC Standard test conditions UTC Coordinated Universal Time

UV Ultraviolet

YOLO You Only Look Once

xxiii

List of Symbols

k q	Boltzmann constant elementary charge	1.380 649 × 10^{-23} J K ⁻¹ 1.602 176 634 × 10^{-19} C
σ	Stefan-Boltzmann constant	$5.67051(19)\times10^{-8}\mathrm{W/m^2K^4}$
A	area of a pixel sensor	m^2
A_{cell}	area of a PV cell	m^2
A_{mn}	area of pixel sensor (m, n)	m^2
a_{ohmic}	ohmic current fraction for avalanche breakdown	[-]
a_0	empiric parameter of the Sandia model	$\mathrm{K}\mathrm{m}^2\mathrm{W}^{-1}$
a_1	empiric parameter of the Sandia model	sm^{-1}
b_0	empiric parameter of the developed model for	J^{-1}
	measuring dust	- 1
b_1	empiric parameter of the developed model for	J^{-1}
1	measuring dust	r_1
b_2	empiric parameter of the developed model for	J^{-1}
	measuring dust	r 1
c_{eff}	calibration factor, ratio of modules' efficiencies	[-]
c_p	specific heat capacity of air	$J kg^{-1} K^{-1}$
C_{refl}	function describing the reflection properties of a PV module	[-]
c_{scat}	empirical scattering calibration function	J^{-1}
d	thickness of a layer	m
DNI	direct normal irradiance	$\mathrm{W}\mathrm{m}^{-2}$
DNI_{λ}	wavelength-dependent direct normal irradiance	$W m^{-2} nm^{-1}$
E_{λ}	wavelength-dependent irradiance reaching the camera	$\mathrm{W}\mathrm{m}^{-2}\mathrm{nm}^{-1}$
E_{λ}^{clean}	wavelength-dependent irradiance reaching the	${ m W}{ m m}^{-2}{ m nm}^{-1}$
π	camera from a clean module	
$E_{\lambda,refl}^{clean}$	wavelength-dependent irradiance reaching the	${ m W}{ m m}^{-2}{ m nm}^{-1}$
7.47.03.0	camera from a clean module that was reflected	
	at the module's surface	
$E_{\lambda,refl}^{soiled}$	wavelength-dependent irradiance reaching the	$\mathrm{W}\mathrm{m}^{-2}\mathrm{nm}^{-1}$
	camera from a soiled module that was reflected	
	at the module's surface	
E_{λ}^{soiled}	wavelength-dependent irradiance reaching the	$\mathrm{W}\mathrm{m}^{-2}\mathrm{nm}^{-1}$
21 . 1	camera from a soiled module	2 1
$E_{\lambda,scat,dir}^{soiled}$	wavelength-dependent direct irradiance reach-	$\mathrm{W}\mathrm{m}^{-2}\mathrm{nm}^{-1}$
	ing the camera from a soiled module that was	
	scattered at the module's surface	-2
G	GTI in the plane of the module	$W m^{-2}$
$G_{s, au}$	part of the GTI transmitted through the soiling layer	$\mathrm{W}\mathrm{m}^{-2}$

$G_{s, ho}$	part of the GTI reflected or scattered at the soil-	$\mathrm{W}\mathrm{m}^{-2}$
"	ing layer	
$G_{g,\rho}$	part of the GTI reflected or scattered at the glass	${ m Wm^{-2}}$
64	layer	
$G_{c,\rho}$	part of the GTI reflected at the semiconductor	$\mathrm{W}\mathrm{m}^{-2}$
	layer	
$G_{g, au}$	part of the GTI transmitted through the glass	${ m Wm^{-2}}$
- 8,1	layer	
$G_{f, ho}$	part of the GTI reflected or scattered at the	${ m Wm^{-2}}$
۵) ,p	ground	, , III
$G_{b, au}$	Part of the irradiance reaching the back-plate	${ m Wm^{-2}}$
$\mathcal{L}_{v,t}$	that is transmitted	, , III
$G_{b,\rho}$	Part of the irradiance reaching the back-plate	${ m Wm^{-2}}$
$\mathcal{C}_{v,\rho}$	that is reflected	V V 111
h	total convection coefficient	${ m W}{ m m}^{-2}{ m K}^{-1}$
_	free convection coefficient	$W m^{-2} K^{-1}$
h _{free}	forced convection coefficient	$W m^{-2} K^{-1}$
h _{forced} H	elevation	
II I		m A
-	electrical current	A
I_{dark}	dark current	A
I_{MPP}	MPP current	A
I_{photo}	photo current	A
I_{sat}	saturation current	A
I_{SC}	Short-circuit current	A
I_{shunt}	shunt current	A
I_{out}	output current of a PV cell	A
L	characteristic length of a module for convection	m
	modeling	
$L_{\lambda,dir}^{soiled}$	wavelength-dependent direct radiance falling	${\rm W}{\rm m}^{-2}{\rm nm}^{-1}{\rm rad}^{-1}$
	onto a soiled module	
$L_{\lambda,scat,dir}^{soiled}$	wavelength-dependent direct radiance scattered	${\rm W}{\rm m}^{-2}{\rm nm}^{-1}{\rm rad}^{-1}$
71,50011,011	at a soiled module reaching the camera sensor	
m	diode breakdown exponent	[-]
$\overline{\overline{M_{cam}}}$	color-mixing matrix of the camera	[-]
m_{cam}	simplified color-mixing matrix of the camera	[-]
n	diode ideality factor	[-]
$\overrightarrow{n_{module}}$	module normal vector	[-]
P	electrical power	W
P_{air}	atmospheric pressure	Pa
p_c	electrical power density of a cell	$\mathrm{W}\mathrm{m}^{-2}$
-	expected electrical power of a module if it was	W
P _{clean,exp}	clean	• •
P ., ,	measured electrical power of a soiled	W
P _{soiled,meas}	temperature corrected power of a soiled module	W
P _{soiled,Tcor}	empirical scattering function	[-]
P_{scat}	thermal conduction	$W m^{-2}$
ġ _{cond}	thermal conduction from a hot side of layer to	$W m^{-2}$
9hot,cold	the colder side	A A 111
à .		$\mathrm{W}\mathrm{m}^{-2}$
q _{cond,gs}	thermal conduction from glass to soiling layer	A A 111

XXV

		2
q́cond,cg	thermal conduction from the cell towards the	${ m W}{ m m}^{-2}$
	glass	
ġ _{cond,cb}	thermal conduction from the cell towards the	${ m Wm^{-2}}$
	backplate	
Ġconv,body	convective heat transfer at a body's surface	${ m W}{ m m}^{-2}$
ġconv,b	convective heat transfer at the back-sheet	${ m W}{ m m}^{-2}$
qconv,s	convective heat transfer at the soiling surface	${ m W}{ m m}^{-2}$
R	reflectance	[-]
$\overrightarrow{RGB_{mn}}$		
	RGB values of a given pixel (<i>m</i> , <i>n</i>)	[-]
R	red channel value of a given pixel	[-]
R^2	coefficient of determination	[-]
R _{clean}	average red channel value of a given area of an	[-]
	image of a clean module	
R _{clean,exp.norm}	average red channel value of a given area of	$m^{-2} s^{-1}$
	an image of a clean module normalized to the	
	exposure time	
R _{clean,GTI,norm}	average red channel value of a given area of	J^{-1}
, ,	an image of a clean module normalized to the	
	exposure time and the GTI	
R_{soiled}	average red channel value of a given area of an	[-]
Sotten	image of a soiled module	
R _{soiled,exp.norm}	average red channel value of a given area of	$m^{-2} s^{-1}$
soriew,exp.morm	an image of a soiled module normalized to the	
	exposure time	
$R_{soiled,GTI,norm}$	average red channel value of a given area of	I^{-1}
soiteu,G11,norm	an image of a soiled module normalized to the	,
	exposure time and the GTI	
R_{scat}	part of the red channel pixel value that corre-	$m^{-2} s^{-1}$
Nscat	sponds to scattered light	111 5
D	serial resistance	Ω
R_s		Ω
$\xrightarrow{R_{sh}} r_{cam}$	shunt resistance	
\longrightarrow	camera position	[-]
$\stackrel{r_{sun}}{\longrightarrow}$	sun position	[-]
$r_{sunreflex}$	sun reflex vector	[-]
SL	soiling loss	%
SL_{cam}	soiling loss measured with the camera-based	%
	method	
SL_{ref}	reference soiling loss, electrically measured	%
SR	soiling ratio	%
t_{acqui}	point in time of image acquisition	date
t _{acq,clean}	point in time of image acquisition of a clean	date
	module	
$t_{acq,soiled}$	point in time of image acquisition of a soiled	date
	module	
t_{exp}	exposure time	ms
t_{soiled}	point in time when a module is soiled	date
t_{ref}	reference point in time when a module is clean	date
T	transmittance	[-]
T_{cell}	transmittance of a given cell	[-]
T_a	ambient temperature	K

T	NOCT	1/
T_{NOCT}	NOCT temperature	K
$T_{NOCT,adj}$	adjusted NOCT temperature	K
T_c	cell temperature	K
T_m	module temperature, measured at the backplate	K
T_{cold}	temperature of a layer on the colder side	K
T_{warm}	temperature of a layer on the warm side	K
T_{body}	temperature of a body	K
T_b	backplate temperature	K
T_f	ground temperature	K
T_{g}	temperature of the glass layer	K
ΔT	temperature difference	K
u_0	empiric parameter of the Faiman model	[-]
u_1	empiric parameter of the Faiman model	[-]
V	voltage	V
V_{br}	diode breakdown voltage	V
V_{j}	diode junction voltage	V
V_{MPP}	MPP voltage	V
V_{OC}	Open-circuit voltage	V
v_w	wind speed	$\mathrm{m}\mathrm{s}^{-1}$
$v_{w,adj}$	adjusted wind speed	$\mathrm{m}\mathrm{s}^{-1}$
	wind direction	°north
$\xrightarrow[x_{obj}]{w_d}$	position of the object seen in the pixel (m, n)	[-]
α	angle under which a ray of light passes through	rad
u	a soiling layer	144
O'	angle between module normal vector and cam-	rad
α_{cam}	era vector	100
(V	angle between module normal vector and sun	rad
α_{sun}	vector	144
ατ	effective transmittance-absorbance product	[-]
β	module inclination	rad
		$\% K^{-1}$
γ Γ	temperature coefficient of module power Gamma correction function	
Γ_{RGB}		[-]
$\xrightarrow{\epsilon_{body}}$	emissivity of a body	[-] J ⁻¹
ϵ_{mn}	color-dependent spectral responsivity of pixel	J
	(m,n)	J ⁻¹
ϵ_{mn}	simplified color-dependent spectral responsiv-	J -
_	ity of pixel (m, n)	т—1
ϵ	simplified color-dependent spectral responsiv-	J^{-1}
	ity	0/
η	module efficiency	%
η_{ref}	nominal module efficiency	%
$\theta_{cam,sun}$	angle between camera vector and sun vector	rad
$ heta_{cam,reflexsun}$	angle between camera vector and sun reflex vector	rad
$ heta_{I,I}$	angle corresponding to the case (I,I) described	rad
- 1,1	in Table 4.1	
$ heta_{I,II}$	angle corresponding to the case (I,II) described	rad
- 1,11	in Table 4.1	
$ heta_{II,I}$	angle corresponding to the case (II,I) described	rad
~ 11,1	in Table 4.1	
	III IMDIC III	

xxvii

$ heta_{II,II}$	angle corresponding to the case (II,II) described	rad
	in Table 4.1	
λ	wavelength	nm
λ_{min}	minimal wavelength that is detected by the cam-	nm
	era	
λ_{max}	maximal wavelength that is detected by the cam-	nm
	era	
λ_{th}	thermal conductivity	${ m W}{ m m}^{-1}{ m K}^{-1}$
ν	kinematic viscosity of air	$m^2 s^{-1}$
$ ho_{spec}$	specular reflectance	[-]
au	soiling transmittance	[-]
$ au_0$	soiling transmittance for perpendicular inci-	[-]
	dence	
$\Phi_{th,sky}$	thermal sky radiation	${ m Wm^{-2}}$
$\Phi_{th,f}$	thermal radiation emitted by the module's back-	${ m W}{ m m}^{-2}$
,	plate	
$\Phi_{th,s}$	thermal radiation emitted by the soiling layer	${ m Wm^{-2}}$
ω	single scattering albedo	[-]

Chapter 1

Introduction

Climate change is a major challenge for mankind. A decisive factor driving climate change is the increasing concentration of carbon dioxide in the atmosphere (Matthews and Caldeira, 2008; Matthews et al., 2009; Gillett et al., 2011; Knutti and Rogelj, 2015; MacDougall et al., 2015; Cook et al., 2016). Hence, there is a need for decarbonization in all sectors. The electricity sector is one of the first to be decarbonized (IEA, 2024). Therefore, energy production has shifted from using fossil fuels like hard coal, lignite, natural gas, and oil towards using renewable energies like hydro power, wind power, and solar (IEA, 2024). Among all renewable energies solar is the most abundant with 3.9×10^9 PJ reaching the Earth every year (Quaschning, 2008). Although, there are also other technologies that convert solar energy into electricity, photovoltaics (PV) is one of the most important ones. It has established itself as the fastest-growing energy source. At the end of 2023, around 1624 GW were installed worldwide (IEA-PVPS, 2024). In 2023 alone 446 GW were installed (IEA-PVPS, 2024). Compared to other electricity generation technologies PV offers several advantages. PV can be installed in large PV parks and on rooftops. PV is suitable for remote solutions. PV is easy to install and the maintenance costs are low. Importantly, PV is often the cheapest way of generating electricity.

With PV installations growing rapidly, there are also new challenges arising, i.e. the monitoring of large PV plants. The efficiency of many parks is reduced by soiling. There are various types of soiling. Common examples are mineral dust deposition, bird droppings, biofilms of bacteria, algae, lichen, mosses, fungi, pollen, and emissions from exhaust engines and agriculture (Martin-Sanchez et al., 2018; Einhorn et al., 2018; Shirakawa et al., 2015). The regions that offer a large solar yield are often arid regions like North Africa or the Middle East that are prone to mineral dust (Ilse et al., 2018; Ilse et al., 2019). Therefore, mineral dust is an important type of soiling and deserves to be investigated further. It is estimated that soiling reduces global solar energy generation by 4% to 7% (Ilse et al., 2019). The impact of soiling depends on various factors. Most importantly, soiling is site-specific. Furthermore, soiling losses depend on the season. For example, rain periods lead to a natural cleaning of PV modules. Some studies have analyzed the impact of meteorological parameters like wind speed, humidity, and aerosol concentration on soiling losses (Figgis et al., 2016).

Soiling not only causes decreases in electricity generation, additionally, soiling can lead to an accelerated degradation of the PV installation (Chen et al., 2021; Garcìa et al., 2003). Soiling can also cause hotspots (Wendlandt et al., 2010; Yang et al., 2010; Oliveira et al., 2018). These are local areas within a PV device that significantly heat up compared to their surrounding due to power dissipation. Hotspots do not only accelerate the degradation, but are often also a safety risk. Hotspots are often detected by infrared (IR) flyovers. It might be challenging sometimes to determine the origin of a hotspot, as hotspots can be caused by defects or by soiling.

Although there are many approaches to mitigate soiling losses, e.g. described by (Ilse et al., 2019), the obvious idea of cleaning the modules remains. The cleaning process itself comes at the cost of labor, water, and initial investment. Optimal strategies include a good timing of the cleaning process, i.e. to reduce the total number of cleaning cycles. To optimize the cleaning routine, soiling measurements are beneficial.

There are already some ways of measuring soiling losses. In this context, the soiling loss is defined as the relative reduction in power experienced by a soiled module compared to the power that the same module would have if it was clean. The power of a soiled device is measured and compared to the power of a clean reference device (Gostein et al., 2013; Gostein, Caron, and Littmann, 2014; Gostein, Düster, and Thuman, 2015). There are two main disadvantages to this method. The clean reference module has to be cleaned every day and the method is not spatially scalable because in a PV park, the power is not measured on a module level.

Many scholars have performed measurements of the mass of the dust deposited on PV modules (Al-Hasan and Ghoneim, 2005; El-Shobokshy and Hussein, 1993; Elminir et al., 2006). The dust mass is correlated with the electrical loss that occurs. Collecting dust enables further analyses. For example, optical transmission, light scattering, and particle size can be studied in detail. However, for determining the electrical losses these have some limitations. The calibration has to be performed that links the dust mass to the soiling loss. Furthermore, this method is also not scalable. Only selected locations within a PV park can be measured.

Another type of indirect soiling measurement is optical soiling sensors. The sensor DUSST has been investigated by (Fernández-Solas et al., 2020). This is a device that uses a monochromatic LED and a PV cell as a light sensor. Soiling losses are quantified by comparing the light transmitted through a soiled glass with the light transmitted through the same glass in clean conditions (Fernández et al., 2019). MARS is another device that uses a camera to capture images of soiled glass. The glass contains small white and black reference areas. The measurement area changes its brightness depending on the soiling deposited on the glass. The brightnesses of the reference areas and the measurement area are compared. Imaging techniques are then used to estimate the transmittance losses (Gostein et al., 2018; Gostein et al., 2019; Aïssa et al., 2022). The DustIQ is an optical sensor that uses a photodiode to quantify the amount of light that is emitted from an LED and then scattered back into the device. The scattered light correlates to the amount of dust particles accumulated on the glass surface of the device (Korevaar et al., 2017; Karki, 2019). These sensors might be capable of giving an estimate of the soiling loss. Their main drawback is that their estimate might be far off and they measure only at one point in the solar field.

To obtain soiling measurements with spatial resolution attempts have been made to measure soiling with cameras. This offers the advantage that surveillance cameras or drones could monitor the soiling. The first approaches used classical computer vision to detect and quantify soiling. (Yap, Galet, and Yeo, 2015) and (Yfantis and Fayed, 2014) have used histogram methods to distinguish between clean and soiled modules on images captured by static cameras. However, these methods didn't calculate the electrical loss caused by the soiling. Furthermore, the practicality of these is questionable.

(Mehta et al., 2018) have created a data set that contains more than 48,000 images of a soiled PV panel. For each image, the electrical power loss has been measured. With this data set the authors have developed an AI model that is capable of predicting the power loss of a module just from seeing an image of this module. The approach

is very promising and is mainly limited by the training dataset. All images were captured from the same perspective from the same camera of the same module. The module was artificially soiled. The developed model could not just be applied to any image of a soiled PV module of a given PV park. (Yang et al., 2024) have developed a similar AI model that is also capable of predicting the soiling loss just from an image of the soiled module. Compared to (Mehta et al., 2018) the main advantage is that the training data contained images of a PV module that experienced real outdoor conditions in Doha. This increases the applicability. However, otherwise, the study suffers from the same limitations as the work by Mehta et. al.

This thesis aims to develop a new optical method that enables an accurate, spatially resolved soiling measurement method for PV parks. The method uses images captured by drones and calculates the soiling loss on a cell level. The method should be generally applicable. The focus is the soiling type dust but also various other soiling types like bird droppings, leaves, etc. should be considered. Within this work, they are summarized under the term inhomogeneous soiling. Inhomogeneous soiling can cause hotspots and lead to security issues. A new electrothermal model is introduced that is capable of estimating a module's temperature with cell resolution for the clean or a soiled state. In particular, hotspot temperatures can be estimated. Furthermore, electrical mismatch losses are considered. The combination of the methods allows the categorization of hotspots into two groups soiling-based and defect-based. This is valuable as IR imaging techniques can identify hotspots but cannot directly determine the hotspot's origin.

This thesis is structured as follows. Chapter 2 summarizes the state of the art in terms of PV soiling measurements. Chapter 3 describes the setup used for the experiments performed. Chapter 4 describes the sub-task of measuring the soiling type dust. Chapter 5 describes the measurement of inhomogeneous soiling types like bird droppings. Chapter 6 describes an electrothermal model that is capable of calculating electrical mismatch losses and of estimating the module's temperature. Chapter 7 gives a summary and provides an outlook for future work.

Chapter 2

State of the Art

This Chapter gives a summary about how soiling affects the operation of PV plants and how its magnitude can be determined. Effects of soiling are discussed for some studies performed at given sites. Soiling measurements with optical sensors, device pairs, and microscopy techniques are discussed. Afterwards, the image based soiling measurements techniques are discussed. These include RGB imaging, as well as IR, and EL imaging techniques. Furthermore, electrical modeling and thermal modeling of PV devices is discussed.

2.1 Soiling of PV Plants

The accumulation of dust, dirt, pollen and other contaminants on the surface of PV modules is commonly referred to as soiling (Ilse et al., 2019). Soiling is an important environmental factor to consider when evaluating the operation of a given PV installation and the potential of a certain location. Soiling reduces the generated power of an affected PV installation by stopping incident light from reaching the absorbing semiconductor layer of the PV module (Garg, 1974; El-Shobokshy and Hussein, 1993; Hassan et al., 2005). Annual soiling losses are typically in the range of 1% to 6% (Caron and Littmann, 2012; Kimber et al., 2006). On a global average they were estimated to be 3% to 4% in 2019 despite of cleaning at many sites (Ilse et al., 2019). At the same time soiling losses vary spatially for different regions and different sites and seasonally (Townsend and Hutchinson, 2000).

(Al Siyabi et al., 2021) have studied soiling losses at a site in Oman. The site is near the desert and is therefore severely affected by sand and dust. In their case study, the authors found that soiling losses reached 4.8% one week after the cleaning process. After three weeks, soiling losses reached 18.1%, and after five weeks 38.1%.

(Caron and Littmann, 2012) have studied soiling losses in southern California. The authors found that soiling losses could be as high as 11.5%. Furthermore, the authors found that the soiling rate, the increase in soiling loss over time, was on average 3.8% per month. Additionally, it was observed that 0.5 mm of rain is in most cases sufficient to naturally clean the affected modules.

(Conceição et al., 2018) have studied the soiling losses in various seasons in Evora, Portugal. In their case study, the authors found that in April soiling losses reached 4.1%, in July 1.9%, and 1.6% in September. The reason for the decrease in soiling was found to be the rain.

(Zorrilla-Casanova et al., 2011) performed a case study in Málaga. The authors obtained an average soiling loss of 4.4%. In the dry season, however, the soiling losses exceeded 20%. Additionally, the authors studied the dependence of the soiling loss on the angle of incidence. It has been confirmed that soiling losses are the lowest for perpendicular incidence. Up to an angle of incidence of 80°, the soiling loss continuously increases.

(Pavan, Mellit, and De Pieri, 2011) have analyzed two sites in Italy. For a site located on compact soil, the authors found an average soiling loss of 1.1%. For the second site which is located on sandy soil, the authors found an average soiling loss of 6.9%.

(Cordero et al., 2018) have investigated different sites in Chile. In the most severe case, in the northern part of the Atacama Desert, the authors found annual losses of 39%. The least affected site showed a soiling loss of 3%. In the capital Santiago, the measured soiling loss was on average 7%. Furthermore, the soiling rate has been studied in dependence on the humidity, the wind speed, the tilt angle of the setup, and the aerosol optical depth. An increased humidity leads to an increased particle deposition and therefore to an increased soiling rate. Increased wind speed on the other hand leads on average to a lower soiling rate. An increased aerosol optical depth leads to an increased soiling rate.

In addition to a lower generated electrical power soiling can also lead to an accelerated degradation of the impacted modules (Chen et al., 2021; Garcìa et al., 2003; Wendlandt et al., 2010; Yang et al., 2010; Oliveira et al., 2018). This can be either directly by contact of the soiling layer and the module's surface or indirectly when the soiling leads to a locally increased temperature. The latter case is discussion in more detail in Section 2.5.

For the above-mentioned reasons the monitoring of soiling is an important aspect to consider for operators of PV parks. There are different strategies of dealing with soiling. There is always a trade-off between improving the performance of a given installation and the costs associated with cleaning the modules. One has to take the initial investment for the cleaning infrastructure, the labor, the water cost, and other operating costs in account. Additionally, one should consider that the monitoring of soiling itself comes at a price. The simplest might be to ignore soiling and monitoring and never clean the PV modules. Another idea is to clean the modules once a year. These strategies are over-simplified, especially for sites that are sensitive to soiling. For improved strategies it is essential to have an estimate of the losses caused by soiling. One possible strategy would be to clean the modules whenever a threshold of e.g. 5% losses is reached. Cleaning strategies have e.g. been discussed in (Mondal et al., 2018; Jamil et al., 2017; Sayyah, Horenstein, and Mazumder, 2014; Ferretti, 2018; Mesbahi, 2018).

2.2 Soiling Measurements

The soiling loss SL is the reduction in electrical power that a PV device experiences due to the presence of soiling. For calculating the soiling loss, first, the difference between the expected power $P_{clean,exp}$ for the imaginary case that the device would be clean, and the actual power $P_{soiled,meas}$ in the soiled state is calculated. This difference is then divided by the expected power to obtain the soiling loss. This is shown in Equation 2.1. The soiling ratio SR, defined in Equation 2.1, is another metric that is often used.

$$SL = \frac{P_{clean,exp} - P_{soiled,meas}}{P_{clean,exp}} = 1 - \frac{P_{soiled,meas}}{P_{clean,exp}} = 1 - SR$$
 (2.1)

2.2.1 Soiling Measurements With Device Pairs

Calculating the soiling loss with device pairs offers several advantages. Typically, these methods are more accurate as the modules are used directly instead of estimating the soiling by a different device type. Furthermore, the impact of the spectral irradiance, the spectral response, the angle of incidence, and other factors are considered.

One question that arises when looking at Equation 2.1 is how to determine $P_{clean,exp}$ as the same module cannot be cleaned and soiled at the same time. Accordingly, there are several similar methods to determine the soiling loss. Commonly, the performance of the soiled PV device is measured and compared with the performance of a clean device of the same type. The two devices should be located close to each other so that they experience the same environmental conditions. In particular, the modules will experience the same ambient temperature T_a , the same wind speed v_w , wind direction w_d , and the same global tilted irradiance GTI. Normalization of the performance should always be performed. This is shown in Equation 2.2. The two devices may perform differently when clean. This may be production-related or due to aging.

$$SL = 1 - \left(\frac{P_{soiled}(t_{soiled})}{P_{clean}(t_{soiled})} \cdot \frac{P_{clean}(t_{ref})}{P_{soiled}(t_{ref})}\right)$$
(2.2)

Here, the indices *soiled* and *clean* refer to the two modules, the soiled module, and the clean reference module. t_{soiled} is the point in time when the module of which the soiling loss should be determined is actually soiled. t_{ref} is the point in time when the reference measurement is performed and both modules are clean. Equation 2.2 can be separated into two steps (see Equations 2.3 and 2.4). Here, c_{eff} is the ratio of efficiencies of both devices (modules) when they are clean. Note that, $P_{soiled}(t_{ref})$ describes the module that is soiled at a different point in time. At t_{ref} , also the *soiled* module is cleaned.

$$c_{eff} = \frac{P_{clean}(t_{ref})}{P_{soiled}(t_{ref})}$$
 (2.3)

$$SL = 1 - \left(\frac{P_{soiled}(t_{soiled})}{P_{clean}(t_{soiled})} \cdot c_{eff}\right)$$
(2.4)

One should note that it is not problematic if t_{soiled} and t_{ref} feature different environmental conditions. It is only important that the conditions for both modules are the same at both points in time. Also, it should be realized that the soiled and the clean reference module have to be surrounded by the same ambient temperature but both modules do not need to show the same surface temperature. It is possible that the soiling leads to a decrease of the module's efficiency and therefore to an increased operating temperature. This temperature increase would be caused by the soiling. Therefore, it would be part of the soiling loss. Therefore, in this thesis no temperature correction is performed. Other authors (Gostein et al., 2013; Gostein, Düster, and Thuman, 2015) have however performed temperature corrections. If the PV devices are reference cells, a tilt correction is sometimes applied, as reference cells that are slightly tilted relative to each other do not experience the same environmental conditions (Esquelli, 2020).

Some authors have compared the short-circuit currents of the devices instead of the power of the devices (Gostein et al., 2013; Gostein, Düster, and Thuman, 2015). If the soiling loss is defined in this way, it is a better metric to describe how much light still enters the cell. However, to estimate the power losses, it is better to compare

the power of the devices with each other as in this case electrical mismatch is also considered (see Section 2.4).

In the case that no second, cleaned device is available, the soiling loss can also be estimated by comparing the power output of the soiled module with the GTI. The GTI should be measured by an adequate PV reference cell with similar properties as the other PV device. If the ratio between the power and the GTI is known for the case that the device is clean, the soiling loss can in turn be inferred. The clean module's power in Equation 2.2 is replaced by the GTI. This is shown in Equation 2.5. If the soiling loss is calculated in this way, normalization to the ambient conditions, in particular to the temperature, is necessary. If the comparison is made between two PV devices, both devices experience the same conditions at a given time. This applies both to the time of the soiling measurement and to the time of the normalization. However, the measurement of the GTI is generally corrected for effects of the ambient conditions, i.e. the corresponding measuring devices perform given corrections internally. Therefore, a temperature difference between the device temperature during normalization and the measurement must be considered. Consequently, a temperature correction is applied when the soiling loss is determined by comparing the module power to the GTI. The module's temperature is assumed to be homogeneous over its entire surface. The backplate temperature T_{module} is measured with a temperature sensor, either a thermo-couple or a resistance-based thermometer like a Pt-1000 (described in Chapter 3). The coefficient γ that describes the relative decrease in power with increasing temperature is stated by the manufacturer in the data sheet. Finally, to get a better estimate of the soiling loss Equation 2.5 is applied with $P_{soiled,Tcor}$ defined in Equation **2.6.** T_{ref} is an arbitrarily chosen reference temperature.

$$SL = 1 - \left(\frac{P_{soiled,Tcor}(t_{soiled})}{GTI(t_{soiled})} \cdot \frac{GTI(t_{ref})}{P_{soiled,Tcor}(t_{ref})}\right)$$
(2.5)

$$P_{soiled,Tcor} = \frac{P_{soiled}}{1 + \gamma \cdot (T_{module} - T_{ref})}$$
(2.6)

One important aspect to keep in mind is that none of the concepts so far consider the wavelength dependence of soiling. The soiling loss was always considered to be an effective average over the wavelength spectrum. In general, this might be a reasonable assumption that e.g. bird dropping have a pretty similar transmittance for red and blue light. On the other hand, it is very likely that some kinds of dust not significantly but noticeably change their transmittance from red to blue light. Also, different PV technologies have different spectral sensitivities. This means that in theory the same soiling layer would lead to different soiling losses dependent on the module technology that is used. (Qasem et al., 2014) found that technologies with a larger bandgap, in particular amorphous silicon-based technologies, suffer from higher electrical losses, when dust is present. However, the above-mentioned measuring techniques remain valid. Limitation would arise for example when the power of a module is compared to the GTI of a PV reference cell and both devices use a different semiconductor.

The angle of incidence (AOI) on a PV module inevitably changes over a day. This can also play a role in the soiling loss. For example, if a soiling layer has a certain thickness or if a leaf only partially sticks onto the module's surface the soiling can also shade an area that would not be considered to be impacted by the soiling from a perpendicular view onto the module. A particularly important soiling type is dust. If a dust layer covers a PV module, its transmittance depends on the angle of incidence. Effectively, the dust layer appears thicker if viewed under an angle. (Heimsath and

Nitz, 2019) have investigated the angular dependence of dust deposited on solar reflectors. This study provides a way to model the angular dependence. It is designed to estimate losses for concentrating solar power (CSP) plants. This is not directly applicable to PV. Soiling losses due to dust are generally higher for CSP than for PV. For CSP only direct irradiance can be used and diffuse irradiance has to be neglected. For PV technologies both contribute to power generation. For both technologies dust reduces the power output by absorbing and scattering the incident light with scattering generally being the dominant factor. If the light is scattered at a dust particle it directly cannot contribute to power generation anymore in the case of CSP. In the case of PV however, a significant amount of scattered light still contributes to power generation. For example, if a PV module is illuminated perpendicularly and scattering takes place at dust particles on the module's surface, photons scattered in forward direction still fall into the module and can be absorbed there.

(Wolfertstetter et al., 2021) have studied the impact of the AOI and the Linke turbidity on the soiling losses. In this study, the soiling of a reference cell was analyzed. The soiling losses of a singular reference cell can be an estimate for the soiling losses of neighboring modules. As expected, it was found that soiling losses increase with increasing AOI. Also, it was found that soiling losses are less impacted by the AOI if the Linke turbidity is higher. This is intuitively understood when considering that a higher Linke turbidity means that the direct irradiance contributes less to the global irradiance.

2.2.2 Optical Soiling Sensors

One way to determine soiling losses are optical soiling measurement (OSM) sensors. These are capable of continuously measuring the soiling losses, are easy to install and to operate, and typically require a calibration step. These devices work as follows. A glass layer experiences the same environmental conditions as the surrounding modules. Therefore, dust is deposited. A light source illuminates the glass layer. This can be either the environment (the sun) or an additional device. An imaging device, such as a camera or a photodiode records information about the soiled glass surface. This information is then evaluated. For example, the covered area can be calculated or the light that is scattered by the dust particles is quantified. These metrics enable the estimation of the soiling loss.

The *MARS* soiling sensor by Atonometrics is a device that uses a camera to capture images of soiled glass (Atonometrics, 2024). The glass contains small white and black reference areas. The measurement area changes its brightness depending on the soiling deposited on the glass. The brightnesses of the reference areas and the measurement area are compared. Imaging techniques are then used to estimate the transmittance losses (Gostein et al., 2018; Gostein et al., 2019; Aïssa et al., 2022).

The *DustIQ* by Kipp & Zonen is also an optical sensor that uses a photodiode to quantify the amount of light that is emitted from an LED and then scattered back into the device (Kipp & Zonen, 2024). The scattered light correlates to the amount of dust particles accumulated on the glass surface of the device (Korevaar et al., 2017; Karki, 2019). These sensors might be capable of giving an estimate of the soiling loss. The main limitation is that the above-mentioned devices can be far off and they measure only at one point in the solar field.

(Wolfertstetter et al., 2021) have highlighted some shortcomings of OSM sensors. These devices are installed larger PV plants. These devices measure the soiling that they experience themselves. The soiling of the modules is not directly measured. Instead, it is assumed that the soiling is similar for the OSM and the modules. They

measure the soiling only at one point and cannot sufficiently consider spatially inhomogeneous soiling.

Furthermore, the impact of the spectral irradiance, the spectral response, and other factors are not considered.

2.2.3 Optical Soiling Sensors With Internal Light Source

The *DUSST* sensor (Detector Unit for Soiling Spectral Transmittance) is an optical sensor that has been developed by (Fernández et al., 2019) and studied by (Fernández-Solas et al., 2020). This is a device that uses a monochromatic LED and a PV cell as a light sensor. Soiling losses are quantified by comparing the light transmitted through a soiled glass with the light transmitted through the same glass in clean conditions (Fernández et al., 2019).

(Campos et al., 2023) have developed the soiling measurement system *Radguard*. The main idea of this system is to avoid the main operational drawback of device pairs, which is the frequent cleaning of the reference device. A lamp that is protected from soiling by e.g. a collimator illuminates a device, a reference cell or a pyranometer, at night. The output signal of the device is then compared to the signal that was obtained from the same setup in the night after the last cleaning procedure. The authors found that their method achieves an accuracy similar to the one of device pairs.

2.2.4 Microscopy Soiling Measurements

(Figgis et al., 2016) first introduced a method to measure soiling deposition and re-suspension rates. The authors used a portable microscope that is capable of measuring the area coverage and the light transmission losses of the soiling. The authors managed to successfully estimate the soiling mass per area. A comparable setup was introduced by (Valerino et al., 2020). The images taken by the microscope are evaluated in regard to the surface coverage. After the analysis of a calibration sample and the assumption of a linear dependence between transmittance loss and area coverage the evaluation of other samples was possible. It should be highlighted that many methods calculate the transmittance in a intermediate step and then derive the soiling loss. The linear calibration factor can vary significantly for different methods and different soiling types (Smestad et al., 2020).

2.3 Image-based PV Monitoring Techniques

The methods of measuring the soiling losses described in the previous section have some limitations when applied to larger scale PV plants. The power of each module is not measured individually. Such power measurements are typically only available on string level. Here a string refers to a connection of various modules mainly in series but potentially also in parallel. Additionally, it is not feasible to permanently operate one clean module. Reference cell systems and OSM measure the soiling loss indirectly and only cover small areas. Therefore, there is wide interest in measuring soiling losses with camera systems. Deriving the soiling losses from images would have the advantage to cover large areas in short times. Cleaning strategies could be optimized further. Soiling might be distributed inhomogeneously within a PV plant. A cleaning routine might start where the soiling has the biggest impact. Some areas within a plant might be cleaned more frequently than others. While infrared (IR) and electroluminescence (EL) imaging techniques are already commonly used for the monitoring of PV plants, visible / RGB imaging techniques are less established yet. While IR and EL imaging are mainly used to detect defective cells and modules, RGB images are mainly suggested to be used for the detection of soiling. All three cases will be discussed below.

2.3.1 RGB Imaging Techniques for Soiling Monitoring

(Qasem, Mnatsakanyan, and Banda, 2016) have developed two computer vision based algorithms to evaluate drone images of PV modules and to quantify soiling losses. One key aspect of the methods is the uniformity of the PV modules on the images. Clean module look very similar at all positions while soiled modules might look very different at different positions. The accuracy of their method is quite low with 5% absolute deviation in the best cases. Another computer vision method has been developed by (Li et al., 2017).

(Mehta et al., 2018) have developed a convolutional network that is capable of detecting soiling on images of PV modules. Additionally, their method is localizing the soiling and estimating the soiling loss. Correspondingly, the method is capable of suggesting a cleaning priority and cleaning strategy. The soiling losses are divided into eight ranges from 0% to 100%, each with a range size of 12.5%. For developing the method, the authors have created and published a dataset consisting of more than 45.000 images. The images are captured by a static camera and show the same perspective of one module from one perspective. The authors have also published their dataset. For every image, the irradiance and the timestamp are stated. The actual soiling loss determined by comparison to a clean reference module is stated. The method was tested on images from the internet of various sources. The classification of the soiling loss into the different categories worked in 97% of the cases. The soiling type classification works in 96% of the cases. The study is a milestone in the camerabased soiling measurements as it is the first of its kind that uses images as an input and can state the soiling loss as an output. The method has the potential to cover larger-scale PV parks. Some limitations are present. As the model considers only one module of one given module type from one perspective the application to other modules from various perspectives is questionable. The soiling patterns used in the study are mainly placed artificially onto the module. Only a few images show real conditions. Deviations are expected when real outdoor conditions are investigated. For the electrical soiling loss a discrete value could be stated instead of a range. The above-mentioned limitations could be removed by enhancing the underlying training

dataset though. Another limitation would be the interconnection of various modules in series or parallel. As the presented method considers each module individually, electrical mismatch cannot be considered. As only the output power and not the IV curve is estimated by the method electrical mismatch could also not be corrected for afterwards.

(Cavieres et al., 2022) have developed a method to diagnose whether a given module is healthy or defective. Furthermore, the soiling type is determined and the soiling loss is estimated in an octile range similar to the above-mentioned method by Mehta. The images used were captured using a static camera and a fixed perspective. The scene shows eight different modules with different amounts of soiling. This dataset was published. Additionally, the dataset of Mehta was used. The method achieved an accuracy of 73% in terms of predicting the range of the soiling loss. Furthermore, the authors report that in 72% of the cases in which the octile range was not predicted correctly, the actual soiling loss was in the neighboring range compared to the prediction.

(Zhang et al., 2021) have developed another model for soiling detection and quantification. Their method is partially based on the above-mentioned study by Mehta. Zhang et al. are stating a concrete value for the soiling loss instead of a range. This is done by using a quantile regression neural network (QRNN). The main difference between the methods by Mehta and Zhang is the mathematical formulation (Zhang et al., 2021). Mehta et al. describe the problem as a classification problem, where solar power losses are categorized as independent classes. A power loss of 19.9% falls into the class 10%-20% while 20.1% falls into the 20%-30% class. The classes are considered to be independent. According to the method of Zhang et al. the classes are overlapping and continuous (Zhang et al., 2021).

Yang et al. have developed a featured-based regression model to estimate the soiling loss. The authors created their dataset consisting of 479 raw images captured by a static camera from a fixed perspective. Some of the features considered by the method are the black-to-white ratio, different image intensity metrics, and different contrast metrics. The connection between the image features and the soiling losses has been studied by the authors in previous studies (Yang, Ji, and Guo, 2020a; Yang, Ji, and Guo, 2020b; Yang, Ji, and Guo, 2021) A linear regression model is trained using a subset of the above-mentioned dataset. The authors claim an uncertainty of less than 10% relative deviation if the soiling loss is higher than 8% for the tests on a test dataset (a part of the 479 images). Mainly, the limitations are similar to the above-mentioned studies. There is only a module type and only one perspective. Additionally, the study considers only the soiling type of dust. It is questionable if a linear regression remains sufficient once the circumstances are generalized.

(Di Tommaso et al., 2022) have used the open-source software YOLO to detect PV panels on RGB and IR images. Furthermore, they were able to detect various kinds of soiling on both RGB and IR images such as dust, bird droppings, delamination, and also hotspots. YOLO is a pre-trained neural network that specializes in detecting objects on images. The default YOLO model has 1000 different categories that it can detect. Via transfer learning the method can be adapted to any kind of object desired by the user. Required for the transfer learning process are images that show the object of interest and ground truth bounding boxes. Generally, the amount of ground truth data required is expected to be lower when applying transfer learning instead of developing a new method from scratch. It should be noted that (Di Tommaso et al., 2022) use the term soiling to describe what is called dust in this thesis. The author of the thesis uses soiling as a general term, including leaves, bird droppings and other soiling types. (Di Tommaso et al., 2022) use anomaly as the general term. 98% of

the PV modules were detected on both RGB and IR images, 88.3% of hotspots were detected on IR images, and 70% of anomalies were detected on RGB images. One advantage of their method is that they didn't rely on artificial soiling. Instead, all data was collected in 2 PV plants in Italy which are both on MW scale. Drone cameras were used to capture the images. As the proposed method uses drones, it is very scalable. Detection can probably be improved by increasing the training dataset of the method. One drawback however is that the method cannot estimate the resulting electrical power loss.

2.3.2 Electroluminescence Imaging Techniques for PV Monitoring

Now some studies are discussed that investigate electroluminescence imaging techniques. In an EL measurement, current is fed into the PV device. Charge carriers will radiatively recombine. Light is emitted according to the bandgap of the device. In the case of crystalline silicon near-infrared light with a wavelength of approximately 1150 nm will be emitted. Defective cells will emit less light or none at all.

EL measurements are mainly performed to check whether a given PV device has defects or not. A device can show none, one, or multiple defects. Also, there are different defect types. (Breitenstein et al., 2011) report that there are mainly micro-cracks, finger interruption, and cell breaks. However, there is no quantitative value that is typically estimated in contrast to the power loss caused by soiling which is a continuous metric. Theoretically, one could also estimate the power loss caused by a defect. This will however be a comparably harder task. In most cases, a defective module should be detected and replaced as soon as possible. Many defects cause a significant decrease in electrical power output and are not reversible. Pre-trained CNNs like AlexNet (Krizhevsky, 2012), VGG (Simonyan and Zisserman, 2014), ResNet (He et al., 2016), and particularly YOLO (Redmon et al., 2016; Redmon and Farhadi, 2017; Redmon and Farhadi, 2018) have been adapted in various studies to detect defective PV devices using EL images (Karimi et al., 2020; Deitsch et al., 2019; Chen, Karin, and Jain, 2022; Tang et al., 2020; Akram et al., 2019). Recently, (Cao et al., 2024) have developed a YOLO instance that is capable of detecting hotspots on electroluminescence images. For developing, validating, and testing the method, the authors have created a dataset containing images of 4530 images of defective PV devices. The authors report a mean average precision of 92.8% defect detection accuracy.

The pre-trained networks can not only be used for detecting defects on EL images. These networks can also be adapted to be used for detecting and distinguishing various soiling types on RGB images. This will be discussed later in Chapter 5. Furthermore, EL images will be used in Chapter 6 to validate the distinction between soiling-based and defect-based hotspots.

2.3.3 Infrared Imaging Techniques for PV Monitoring

Infrared thermography measurement methods work very similarly to EL measurement techniques. Strictly speaking, EL measurements are IR measurements. Sometimes EL measurements are referred to as dark IR imaging. In this work, however, IR measurements refer to measurements that are performed while the PV device is under normal operation when they are illuminated. There is no current fed into the device. Defective devices will in many cases heat up, e.g. due to shunts. The increased temperature is detected as it leads to increased thermal radiation and a shifted spectrum of thermal radiation. The emitted spectrum is broader than in the

case of EL measurements. The spectrum depends on the temperature instead of the PV device's bandgap. IR monitoring methods are e.g. discussed in (Akram et al., 2020; Gallardo-Saavedra et al., 2020; Kandeal et al., 2021). Also, here CNNs find wide application.

Chapter 6 will discuss the electrothermal modeling of soiled PV modules. It will be discussed which soiling patterns can cause hotspots. IR imaging will be used for validation purposes.

2.4 Electrical Modeling of PV Modules

The electrical modeling of PV modules is of great interest as it enables a prediction of the electrical power in dependence on meteorological parameters like the GTI and the ambient temperature. Also, the calculation of electrical mismatch is important for the cases, in which a module is partially soiled or shaded. Electrical mismatch describes the situation in which the weakest cell (e.g. the one with the heaviest soiling) limits the performance of the entire module. The total loss might be significantly bigger than the average loss over all cells. (Bishop, 1988) has presented a study that allows this electrical modeling of arrays of PV devices. His model is capable of analyzing serial and parallel interconnections of cells and modules. It has been implemented in the python package pylib (Holmgren et al., 2015; Holmgren, Hansen, and Mikofski, 2018). The Bishop model is based on the single-diode model.

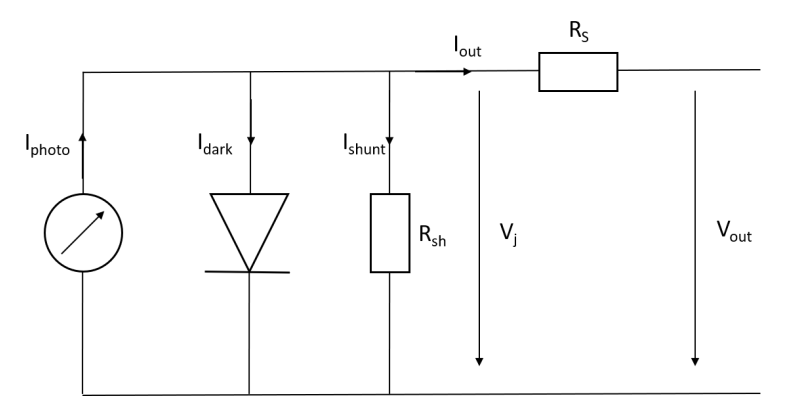


FIGURE 2.1: Equivalent circuit diagram of the single-diode model.

Figure 2.1 shows the equivalent circuit diagram of the single-diode model. According to the single-diode model, a PV cell consists of a current source, a diode, a shunt resistance R_{sh} , and a series resistance R_{s} . I_{photo} is the photo-current generated by the current source depending on the illumination. I_{dark} is the dark current passing through the diode. I_{shunt} is the current through the shunt resistance. V_{j} is the voltage across the diode junction. I_{out} is the output current of the entire PV cell and V_{out} is the output voltage of the entire PV cell.

$$I_{out} = I_{photo} - I_{sat} \cdot \left[\exp\left(\frac{q \cdot (V + I_{out} \cdot R_s)}{nkT}\right) - 1 \right] - I_{shunt}$$
 (2.7)

$$I_{shunt} = \frac{V_j}{R_{sh}} \cdot \left[1 + a_{ohmic} \cdot \left(1 - \frac{V_j}{V_{br}} \right)^m \right]$$
 (2.8)

Equation 2.7 implicitly defines the IV curve (Bishop, 1988). I_{sat} is the saturation current of the diode, q is the elementary charge, n is the diode ideality factor, and k is the Boltzmann constant. The current over the shunt resistance can be calculated by Equation 2.8 according to Bishop (Bishop, 1988). V_{br} is the breakdown voltage, a_{ohmic} is the fraction of ohmic current involved in avalanche breakdown, and m is the breakdown exponent. The Bishop model is capable of calculating the IV curve for an individual cell and is capable of calculating the IV curve of any connection of various cells either in parallel or in series or both. In particular, electrical mismatch is considered for the case that one cell is shaded, soiled, or defective.

2.5 Thermal Modeling of PV Modules

The module temperature is an important parameter for monitoring a PV installation. The temperature directly impacts the power output and additionally plays a role in the aging process. Furthermore, local defects and spatially inhomogeneous soiling can both cause hotspots (Vumbugwa et al., 2020). Hotspots, also small in size, drastically reduce the power output and increase aging.

In this section, an overview is given of existing methods for modeling the PV module temperature. The module temperature depends on the environmental meteorological conditions. The module temperature is an important quantity as it influences the performance of a given PV installation. An increase in temperature typically reduces the efficiency of the modules. For crystalline silicon technologies, the relative reduction in power is about -0.4%/K (*Module data sheet* 2024). Furthermore, an increased temperature accelerates the aging-based degradation of a PV module.

2.5.1 Modeling of Clean, Intact Modules

One of the simplest thermal models is the Ross model (Ross, 1981). The Ross model is defined in Equation 2.9 and determines the cell temperature T_c . The model requires the following input parameters: the ambient temperature T_a , the global tilted irradiance GTI, and the module's NOCT (normal operating cell temperature) temperature T_{NOCT} . The NOCT temperature is module specific and is typically stated by the manufacturer in the data sheet. It considers the following conditions: GTI = $800 \, \text{W/m}^2$, wind speed = $1 \, \text{m/s}$, ambient temperature = $20 \, ^{\circ}\text{C}$, and air mass 1.5.

$$T_c = T_a + \text{GTI} \cdot \frac{T_{NOCT} - 20^{\circ}\text{C}}{800\text{W/m}^2}$$
 (2.9)

The Sandia Photovoltaic Array Performance Model (King, Kratochvil, and Boyson, 2004) in addition considers wind effects. In the first step, the model determines the PV module's backside temperature, and the surface temperature on the module's rear side, T_m . In the second step, it calculates the cell temperature T_c . The Sandia model requires the GTI, two empirically determined coefficients a_0 and a_1 based on the module structure and the type of mounting, the wind speed v_w , and the ambient temperature T_a . Equation 2.10 shows how to determine the backplate temperature T_m and the cell temperature T_c respectively. Note that ΔT describes the temperature difference between T_m and T_c for a GTI of $1000 \, \text{W/m}^2$. a_0 has the unit $\text{K} \cdot \text{m}^2/\text{W}$ and a_1 has the unit s/m.

$$T_m = \text{GTI} \cdot a_0 \cdot \exp(a_1 \cdot v_w) + T_a$$

$$T_c = T_m + \frac{\text{GTI}}{1000\text{W/m}^2} \cdot \Delta T$$
(2.10)

The Faiman model is a thermal model which uses empirical heat loss factors (Faiman, 2008). Equation 2.11 describes how the cell temperature T_c is determined based on the ambient temperature T_a , the GTI, the two heat loss factors u_0 and u_1 , and the wind speed v_w .

$$T_c = T_a + \frac{\text{GTI}}{u_0 + u_1 \cdot v_w} \tag{2.11}$$

The U.S. National Renewable Energy Laboratory developed the NOCT Cell Temperature Model as part of the System Advisor Model (SAM) (Gilman, 2015). It is one of the most sophisticated thermal models. Equation 2.12 illustrates how the thermal

model predicts the cell temperature T_c . Input variables are the ambient temperature T_a , the GTI, and the module efficiency η_{ref} at reference conditions. In addition, the effective transmittance-absorbance product $\alpha\tau$ is required, which combines the transmittance and absorptance effects of the photovoltaic cell with the incoming solar radiation G. Both T_{NOCT} and v_w are adjusted by the type of mounting and the height above the ground leading to $T_{NOCT,adj}$ and $v_{w,adj}$. To obtain these parameters, an offset is added to T_{NOCT} and v_w is multiplied by an attenuation factor (Gilman, 2015).

$$T_c = T_a + \frac{\text{GTI}}{800\text{W/m}^2} \cdot (T_{NOCT,adj} - 20^{\circ}\text{C}) \cdot (1 - \frac{\eta_{ref}}{\alpha \tau}) \cdot \frac{9.5}{5.7 + 3.5 \cdot v_{w,adj} \cdot \text{s/m}}$$
(2.12)

These thermal models consider the ambient temperature and solar radiation to determine cell temperatures. Three of them also include wind speed, which is expected to have a major impact on the results (Lamaamar et al., 2021; Skoplaki and Palyvos, 2009). Yet, the thermal models lack in replicating the whole PV module under partial shading or partial soiling conditions. Even though single cells can be simulated and their temperatures determined on the cell level, the effects of shaded cells on their neighboring cells and the entire surrounding string are not considered. However, this would be necessary for the intended purposes.

2.5.2 Modeling of Hotspots

Hotspots are locations within a PV module that show a temperature increase compared to the remaining PV module's surface. However, hotspots are typically not defined by the temperature increase exceeding a certain threshold. Instead, a hot-spot is typically defined as a cell being operated with a current higher than its short-circuit current. This causes the affected cell to be operated in the reverse bias region and thus leads to power dissipation and local heating (IEC, 2005; Winkel et al., 2024b).

Qian et al. have developed a model that is capable of simulating the hotspot temperature of a partially shaded cell (Qian et al., 2018). They have investigated different degrees of shading, changing the covered area of a given cell. A key finding was that half-cell modules are less prone to create hotspots. If a hotspot occurs, the temperature increase will be significantly lower compared with an analogous full-cell module. The developed model was not validated against a measurement. The model was not designed to be applied in outdoor conditions. Instead, the estimation of the above-mentioned difference between half-cell and full-cell modules was the objective. Solheim et al. have simulated a PV hotspot accurately using a finite elements method (Solheim et al., 2013). They considered 800,000 nodes per module. This makes the approach too intense in terms of calculation to be applied to a larger scale. A study by Rossi et al. presented a thermal model that is not only capable of estimating the final hotspot temperature but is also capable of modeling the process of the affected cell heating up over time (Rossi et al., 2014). It is a dynamic model instead of a steadystate model. Furthermore, the paper proposed a method to detect hotspots. The hotspot detection relies on current sensors connected to the output of each module. It is desirable to use images for hotspot detection as this would remove the need for the above-mentioned current sensors. The current sensors would offer the advantage of permanently providing data. A drone camera system would not have this advantage. Surveillance cameras can continuously record data. The thermal model has not been validated under outdoor operating conditions. Geisemeyer et al. developed a thermal model that is capable of calculating the hotspot temperature of a partially shaded cell (Geisemeyer et al., 2014). Their model not only gives a value of the temperature

but also gives the temperature distribution within the affected cell. On the other hand, their model is very complex and unsuitable to be applied to a larger number of modules.

To the best of the author's knowledge, there is no thermal model with low calculation effort for hotspot temperature simulation of soiled or shaded cells that is validated over a larger time interval under real operating conditions.

One of the goals of this work is to develop a simple enough electrothermal model that is usable for real operating conditions and the specific application case with cell-resolved soiling input data that provides the temperature output with cell resolution. In particular, the electrothermal model is connected to the cell-resolved soiling measurements performed in this work.

2.6. Statistics

2.6 Statistics

The following statistical metrics are used in the evaluation parts of this thesis. These values occur during the validation of a model. x_i is the measured value of a quantity and \hat{x}_i is the model's prediction of this value. \bar{x}_i is the average of all measured values. N is the total number of all data points. The root mean square error RMSE, see Equation 2.13, is a metric that describes deviation between the actual measured values and the prediction. Similarly, the mean absolute error MAE also describes the deviation between the prediction and the measurement (see Equation 2.14). Here, however, all data points are weighted the same. In contrast, the RMSE weighs outliers more. The mean bias error MBE is a metric that describes how the weather the model on average overestimates or underestimates the actual value (see Equation 2.15). The coefficient of determination R^2 , defined in Equation 2.16, describes the ratio of how much of the variation of the actual data points can be explained by the model. Generally, a R^2 close to one indicates a good model. A R^2 close to zero suggests that the model cannot explain the variation in the measured data.

RMSE =
$$\sqrt{\frac{\sum_{i=1}^{N} (x_i - \hat{x}_i)^2}{N}}$$
 (2.13)

$$MAE = \frac{\sum_{i=1}^{N} |x_i - \hat{x}_i|}{N}$$
 (2.14)

MBE =
$$\frac{\sum_{i=1}^{N} (\hat{x}_i - x_i)}{N}$$
 (2.15)

$$R^{2} = 1 - \frac{\sum_{i=1}^{N} (x_{i} - \hat{x}_{i})^{2}}{\sum_{i=1}^{N} (x_{i} - \bar{x}_{i})^{2}}$$
(2.16)

Chapter 3

Setup and Methods

In this Chapter the setup is explained that is used for the experiments in the following Chapters 4, 5, and 6. Additionally, some important methods are introduced.

3.1 PV Testbench

The experiments for the scientific research presented in this work have been performed at a PV testbench located on CIEMAT'S Plataforma Solar de Almería (PSA).



FIGURE 3.1: PV Testbench used for most experiments with this work. There are twelve modules in total, six different types, two of each type. There are six photogrammetry targets mounted on the setup. Multiple additional targets are placed around the setup. The numbers refer to an internal numbering. This numbering will be used in the following Chapters to clearly identify each module.

Figure 3.1 shows the testbench. It consists of twelve modules. The modules are listed in Table 3.2. There are six different module types and two modules of each type. The numbers are assigned here to clearly identify the modules. These numbers will be used in the following Chapters. As soiling experiments are one of the main purposes of the setup it is designed symmetrically. One possible use case is the following. One module of each type is located in the west and one in the east. The west side is considered the soiled side and the east side is considered the clean side. As discussed in section 2.2 one of the more accurate ways of measuring soiling of a given module is the comparison to a clean module of the same type. The designs of the experiments performed in this work is discussed later individually. The modules are oriented in south direction with an inclination of 30° . The power of all twelve modules is permanently recorded with a time resolution of one measurement every 10 seconds. For two of the twelve modules the IV curves are also recorded. This is additional information as the regular power measurement gives only the power at the maximum power point (MPP) while the IV curve contains also the open-circuit voltage (V_{OC}), the

TABLE 3.1: Table listing the characteristic data of the modules installed at the testbench. In the following, mainly the Axitec modules are used. They are highlighted in Figure 3.1.

Manufacturer	Nominal Power	Specifications
JA Solar	410 W	bi-facial, half-cell, mono-Si, PERC
JA Solar	390 W	full-cell, mono-Si
Risen	375 W	bi-facial, half-cell, mono-Si
Jinko	395 W	bi-facial, half-cell, mono-Si
Axitec	335 W	72 full-cells, poly-Si
Axitec	280 W	60 full-cells, poly-Si

short-circuit current (I_{SC}) and the voltage and the current at the MPP (V_{MPP} and I_{MPP}). There are also twelve Pt-1000 temperature sensors (uncertainty class B, DIN EN 60751) available. For a measured temperature of 100°C this refers to an uncertainty of 0.8 K. Typically, one temperature sensor would be mounted at each module. Furthermore, the testbench has two reference cells in plane with the modules that measure the GTI. All parameters which are measured at the testbench and used in this work are listed in Table 3.2. The sampling rate of each sensor is one measurement every 10 s. The IV-curve is the only exception with one measurement per minute.

100 m in the north of the setup there is a meteorology station that measures all important meteorological parameters. Measured is for instance the direct normal irradiance (DNI) by a pyrheliometer. The near-infrared irradiance emitted by the sky is measured with a pyrgeometer. Both the wind direction and the wind speed is measured. The ambient temperature and the atmospheric pressure is measured. The parameters are also listed in table 3.2.

3.1. PV Testbench 23

TABLE 3.2: Table listing the different quantities measured at the test-bench and the meteorology station close to the testbench.

Quantity	Symbol	Unit	Measurement Instrument
Electrical power	P	W	SOL.Connect Center III meter
			by Papendorf Software Engi-
			neering GmbH, 10 channels
IV curve	-	-	SOL.Connect meter mpp by
			Papendorf Software Engineer-
	7		ing GmbH, 2 channels
Short-circuit current	I_{SC}	A	SOL.Connect meter mpp
Open-circuit voltage	V_{OC}	V	SOL.Connect meter mpp
MPP current	I_{MPP}	A	SOL.Connect meter mpp
MPP voltage	V_{MPP}	V	SOL.Connect meter mpp
Direct normal irradiance	DNI	W/m^2	Kipp & Zonen first class
			pyrheliometer
Global tilted irradiance	GTI	W/m^2	SOZ-03 reference cell by NES
			Sensors GmbH
Module temperature	T_m	K or °C	Pt-1000 thermometer
Ambient temperature	T_a	K or °C	CS215-L thermometer
Wind speed	v_w	m/s	NRG 200m wind wane by
-			NRG Systems
Wind direction	w_d	$^{\circ}$ north	NRG 200m wind wane by
			NRG Systems
Atmospheric pressure	P_{air}	Pa	Barometer
Thermal sky radiation	Φ_{sky}	W/m^2	CGR4 Pyrgeometer by Kipp
	v		& Zonen, serial number
			IRCGR4-120446

3.2 Camera Systems

A DJI Mavic 2 Pro drone is used for the flights and to capture the images (DJI, 2024). The images have 5472 by 3648 pixels. The pixel sensors are based on the CMOS technology. The camera has an opening viewing angle of 77 degrees.

3.2.1 Gamma Correction

For the measurement method developed in Chapter 4, there must be a linear relation between the radiance falling into a camera's pixel sensor and the corresponding RGB value of this pixel. For RGB images in the formats jpg or png, this is typically not the case. Instead, for a typical camera, the relation between the radiance reaching the sensor and the RGB value is non-linear. For small radiances, even a small increase in brightness (radiance) can cause a larger increase in the RGB values. While for higher radiances it takes a large increase in brightness (radiance) to cause even a small increase in the RGB values.

To obtain images that show the desired linear behavior raw images in the dng format can be captured. For reasons of practicality, the raw images can afterwards be converted into linearized RGB images.

3.2.2 Flat Field Correction

The lens attached to the front of the camera results in darkening the edges of the image, known as vignetting. Vignetting refers to a position-dependent loss of light in the performance of an optical system, which is mainly due to the blockage of part of the incident beam by the effective size of the aperture stop. This reduction of light results in a gradual fading of an image at points near its periphery (Szeliski, 2022).

In order to calculate the vignetting effect images of an integrating sphere are captured. This is a device that is white in its interior. The inside is illuminated for these experiments. The expected image therefore shows the same brightness at all positions. In reality, however, the image loses brightness at the edges and particularly in the corners. The center of the image is the brightest. A correction matrix is calculated that states for every pixel the relative decrease in brightness compared to the brightest pixel in the center of the image. In the following, this matrix is used to compensate for the brightness reduction of at the edges.

3.2.3 Photogrammetry

One important intermediate step in the analyses in this work is the calculation of orthoimages. This refers to the following: The PV modules investigated here are all rectangular. In the images, they are distorted due to the perspective. The idea is to account for the perspective and segment a rectangular image of the PV module out of the entire scene. This photogrammetry method has been described in detail in (Prahl, 2019). For the calculation of orthoimages the camera position, the module position, and the lens properties are considered. When the lens properties are known optical distortion can be considered.

The testbench is measured with a tachymeter to create an accurate reference coordinate system with accurate locations of each module. The measurements include the corners of the modules as well as the position of six reference photogrammetry targets. The targets can for example be seen in Figure 3.1. The targets consist of a white circle and an identification code around the white circle. The circles are used to

25

later calculate the position of the camera relative to the target. The photogrammetry software will fit an ellipse to the circle. This accounts for perspective distortion and the viewing angle can be estimated. The code around the circle distinguishes the targets.

During a measurement, additionally, photogrammetry targets are placed on the ground around the setup (see Figure 3.1). These targets support an accurate calculation of the camera position relative to the testbench.

Chapter 4

Drone-Based Optical Measurement of Dust-Like Soiling

This Chapter aims to develop a new camera-based method for quantifying the electrical losses caused by the deposition of mineral dust on the PV modules. In comparison to the methods described in Chapter 2 the here presented method aims to concretely state the soiling loss instead of giving a range. Furthermore, the method should use images captured by drones. This enables the method to be scaled to the level of an entire PV plant.

Note that parts of this Chapter have already been published by the author in (Winkel et al., 2024a).

4.1 Optical Measurement Principle

PV modules are typically quite dark because they should absorb as much light as possible in order to convert it into electricity. The deposition of particles on their surface leads to light scattering which makes the modules appear brighter. The method is based on measuring this brightness increase and converting it to the soiling loss. The reflectance of a PV module as well as the scattering by the particles both show a strong angular dependence and have to be considered.

The first step of the method requires the isolation of the scattering signal from the signal that would be found for a clean module (clean background calibration). Images of a clean module are taken from various perspectives for this purpose. The second step of the method is the conversion of the brightness increase into the soiling loss (scattering calibration). This is carried out using images of a soiled module with known soiling loss from various perspectives. The soiling loss of this module is obtained by comparing its power output to that of the cleaned module as described in Chapter 2, and e.g. in (Gostein, Düster, and Thuman, 2015; Gostein et al., 2016).

Practically, the measurement is performed in two steps. First, a spiral flight is performed over the two above-mentioned reference modules. Afterwards, other modules can be evaluated. The soiling loss will be calculated for every image of every cell individually. For each cell, a filtered average is calculated over all images.

4.2 Optical Measurements Theory

Figure 4.1 illustrates the geometry of the measurement. For diffuse radiation, only one beam is sketched exemplary, while diffuse radiation is coming from the entire hemisphere. The reflected and scattered light is indicated with an ellipse because light scattering takes place in various directions. It has to be noted that the sun vector, the module normal vector, and the camera vector (drone vector) do not have to be in plane in the three-dimensional case. This is a simplification for the illustration. All vectors are pointing away from the module.

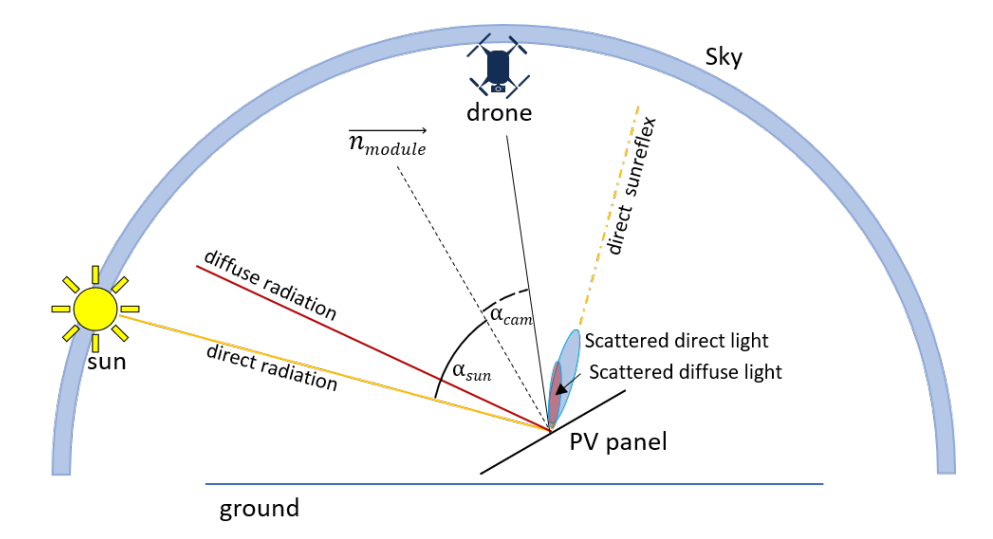


FIGURE 4.1: Sketch to describe the geometry of the measurement method. Shown are the sun position, a direct sun ray towards the PV module, the drone position, and the module position including its normal vector $\overrightarrow{n_{module}}$. Also, one exemplary ray contributing to the diffuse radiation received that is received by the module is shown. Additionally, the direct sun reflex is shown together with the reflex of the diffuse radiation of one exemplary point in the sky.

4.2.1 Relation of the RGB Values to the Incoming Radiation

The camera mounted on the drone is used as a sensor. The captured images are interpreted as irradiance maps. Each pixel corresponds to a certain irradiance caused by radiation coming from a certain direction. The relation between the irradiance and the pixel's RGB values is described by the camera equation (Equation 4.1) (Kuhn et al., 2017; Wilbert, 2009).

$$\overrightarrow{RGB_{mn}} = \Gamma_{RGB} \left(\overline{\overline{M_{cam}}} \cdot \int_{A_{mn}} \int_{\lambda_{min}}^{\lambda_{max}} t_{exp} \cdot \overrightarrow{\epsilon_{mn}} \cdot E_{\lambda} \left(\overrightarrow{r_{cam}}, \overrightarrow{x_{obj}}, t_{acqui} \right) d\lambda dA \right)$$
(4.1)

 $\overrightarrow{r_{cam}}$ is the vector from the object seen in pixel (m, n) to the entrance pupil of the camera. $\overrightarrow{x_{obj}}$ is the position of the object seen in pixel (m, n) in a global coordinate system. $\overrightarrow{RGB_{mn}}$ is a vector containing the three-color channel values of a certain pixel (m, n). Γ_{RGB} is the camera-specific gamma correction that considers the potentially non-linear response in terms of irradiance. $\overline{\overline{M_{cam}}}$ is the camera-specific color-mixing

matrix, A_{mn} is the pixel area of the pixel, $\overrightarrow{\epsilon_{mn}}$ is its color-dependent spectral responsivity, and λ_{min} and λ_{max} are the minimum and maximum wavelength of the spectrum that are detected by the camera. The exposure time of an image is denoted t_{exp} . E_{λ} is the wavelength-dependent irradiance that is caused by radiation reaching the camera at the time of the image acquisition t_{acqui} from the specific perspective and object.

$$R\left(\overrightarrow{r_{cam}}, \overrightarrow{x_{obj}}, t_{acqui}, t_{exp}\right) = m_{cam} \cdot A \cdot t_{exp} \int_{\lambda_{min}}^{\lambda_{max}} \epsilon \cdot E_{\lambda}\left(\overrightarrow{r_{cam}}, \overrightarrow{x_{obj}}, t_{acqui}\right) d\lambda \tag{4.2}$$

This relation between the irradiance caused by the radiation received from a certain object element and the red channel in the corresponding image element will be used to connect the brightness increase to the incoming solar irradiance and the soiling loss in the following.

4.2.2 Contributions to the Camera Signal According to the Interaction at the Module's Surface

First, an image of a soiled module is considered. The irradiance E_{λ}^{soiled} which falls from the soiled module into the camera can be split into different terms. The subscript λ indicates the wavelength dependence of the irradiance. The superscript "soiled" indicates that the irradiance is coming from a soiled module. The first contribution is $E_{\lambda,scat,dir}^{soiled}$ which denotes the direct irradiance scattered at the soiling layer of the module that hits the camera. On the other hand, there is $E_{\lambda,refl}^{soiled}$ which describes the reflected irradiance at the module's surface that is hitting the pixel. It consists of both direct and diffuse irradiance and it considers both specular and diffuse reflection. There is also scattering of the diffuse irradiance towards the camera, but this term is neglected because the scattered direct irradiance is much greater than the diffuse irradiance for sunny conditions. It is ensured that this assumption is correct by requiring that the modules are not shaded by clouds during the measurements and by limiting the evaluation to small incidence angles of the direct irradiance (less than 40°).

$$E_{\lambda}^{soiled} = E_{\lambda,scat,dir}^{soiled} + E_{\lambda,refl}^{soiled}$$
(4.3)

In the case of a clean module, indicated by the superscript "clean", the Equation simplifies as follows

$$E_{\lambda}^{clean} = E_{\lambda,refl}^{clean} \tag{4.4}$$

In the following it is shown how $E_{\lambda,refl}^{clean}$ and $E_{\lambda,refl}^{soiled}$ are related to each other.

4.2.3 Comparing the Camera Equation for the Clean and Soiled Case

The measurement equation is derived by comparing the camera equation for the clean and soiled cases of Equation 4.2.

$$R_{clean/soiled} = m_{cam} \cdot A \cdot t_{exp} \int_{\lambda_{min}}^{\lambda_{max}} \epsilon \cdot E_{\lambda}^{clean/soiled} \left(\overrightarrow{r_{cam}}, \overrightarrow{x_{obj}}, t_{acq,clean/soiled} \right) d\lambda \quad (4.5)$$

The point in time when the image of the soiled module is captured is denoted $t_{acq,soiled}$ and $t_{acq,clean}$ is the acquisition time of the image of the clean module. These equations can be simplified further by dividing by the constants and the known exposure time so that these parameters and the red pixel value are combined in one parameter, respectively $R_{soiled,exp,norm}$ or $R_{clean,exp,norm}$. This results in the following:

$$R_{clean/soiled,exp.norm} = \int_{\lambda_{min}}^{\lambda_{max}} \epsilon \cdot E_{\lambda}^{clean/soiled} \left(\overrightarrow{r_{cam}}, \overrightarrow{x_{obj}}, t_{acq,clean/soiled} \right) d\lambda \tag{4.6}$$

With

$$R_{clean/soiled,exp.norm} = \frac{R_{clean/soiled}}{m_{cam} \cdot A \cdot t_{exp}}$$
(4.7)

 E_{λ}^{clean} can be written as shown in Equation 4.3 and simplified using a hereby defined function $c_{refl}(\overrightarrow{r_{cam}},\overrightarrow{r_{sun}})$:

$$R_{clean,exp.norm}\left(\overrightarrow{r_{cam}},\overrightarrow{r_{cam}}\right) = \int_{\lambda_{min}}^{\lambda_{max}} \epsilon \cdot E_{\lambda}^{clean}\left(\overrightarrow{r_{cam}},\overrightarrow{x_{obj}},t_{acq,clean}\right) d\lambda$$

$$= c_{refl}\left(\overrightarrow{r_{cam}},\overrightarrow{r_{sun}}\right) \cdot GTI(t_{acq,clean})$$
(4.8)

On the one hand, R_{clean} is proportional to the illumination of the module, described by the global tilted irradiance $GTI(t_{aqc,clean})$ in the plane of the module at the point in time $t_{acq,clean}$ of capturing the image of the clean module. On the other hand, it is assumed that all dependencies of the geometry can be summarized in a function $c_{refl}(\overrightarrow{r_{cam}},\overrightarrow{r_{sun}})$. It is assumed that all cells show the same optical behavior in the clean state so that at the end, R_{clean} does not depend on $\overrightarrow{x_{obj}}$ anymore. This assumption is acceptable for many PV modules, but there are also PV modules for which it is not applicable. If different cells, e.g., within a poly-crystalline PV module, look noticeably different, the method will hence most likely lead to higher deviations. Furthermore, it is assumed that the optical properties of the cells are described well by a rotational symmetry for c_{refl} around the module normal vector $\overrightarrow{n_{module}}$. Correspondingly, c_{refl} can also be described by a set of three angles: the angle between the camera vector and the normal vector α_{cam} , the angle between the sun vector $\overrightarrow{r_{sun}}$ and the normal vector α_{sun} , and the angle between the camera vector and the sun vector $\theta_{cam,sun}$. There are also other combinations of angles that can describe the situation. For example, the angle $\theta_{cam,reflexsun}$ between the camera and the sun reflex vector $\overrightarrow{r_{sunreflex}}$ might be suited better than the angle $\theta_{cam,sun}$ between the camera vector and the sun vector. For the case of a soiled module, one can use Equation 4.3 and $c_{refl}(\overrightarrow{r_{cam}}, \overrightarrow{r_{sun}})$ as explained in the following to obtain Equation 4.9.

$$\begin{split} R_{soiled,exp.norm}\left(\overrightarrow{r_{cam}},\overrightarrow{x_{obj}},t_{acq,soiled}\right) \\ &= \int_{\lambda_{min}}^{\lambda_{max}} \epsilon \cdot E_{\lambda,scat,dir}^{soiled}\left(\overrightarrow{r_{cam}},\overrightarrow{x_{obj}},t_{acq,soiled}\right) d\lambda \\ &+ \int_{\lambda_{min}}^{\lambda_{max}} \epsilon \cdot E_{\lambda,refl}^{soiled}\left(\overrightarrow{r_{cam}},\overrightarrow{x_{obj}},t_{acq,soiled}\right) d\lambda \\ &= R_{scat}\left(\overrightarrow{r_{cam}},\overrightarrow{x_{obj}},t_{acq,soiled}\right) + c_{refl}\left(\overrightarrow{r_{cam}},\overrightarrow{r_{sun}}\right) \cdot \tau(\alpha_{sun}) \cdot \tau(\alpha_{cam}) \cdot \text{GTI}(t_{acq,soiled}) \end{split}$$

$$(4.9)$$

 R_{soiled} consists of two parts. R_{scat} is defined as the contribution related to the first integral and corresponds to the scattering at soiling particles. The second summand in the equation is similar to Equation 4.5 for the clean module and can be interpreted as the brightness without scattering by soiling particles — or in other words, basically, roughly the brightness one would see if the module was clean. The factors $\tau(\alpha_{sun})$ and $\tau(\alpha_{cam})$ consider that the reflection signal is attenuated compared to the clean case. τ is the wavelength averaged transmittance of the soiling layer. It depends on the angle under which the radiation falls on the soiling layer, so that two typically different transmittances appear in the equation. The soiling layer is passed by the reflected light first under the angle α_{sun} and afterwards under the angle α_{cam} . Under the above assumptions for the properties of the cells, $c_{refl}(\overrightarrow{r_{cam}},\overrightarrow{r_{sun}})$ is the same for the clean module and the soiled module, as long as the geometry defined by $\overrightarrow{r_{cam}}$ and $\overrightarrow{r_{sun}}$ is the same. Equations 4.5 and 4.6 are then connected to each other — by rewriting Equation 4.6 using $R_{clean,exp.norm}$ from Equation 4.5. For this, we consider images of a clean module element and a soiled module element taken from the same relative position of the camera to the module element $\overrightarrow{r_{cam}}$ and $\overrightarrow{r_{sun}}$. Then, Equation 4.5 is solved for $c_{refl}(\overrightarrow{r_{cam}},\overrightarrow{r_{sun}})$ and substitute the result in Equation 4.6. In doing so, we assume that the transmittances did not change between the two image acquisitions. The resulting equation links the clean and the soiling images and is the basis for deriving the soiling loss.

$$R_{soiled,exp.norm}\left(\overrightarrow{r_{cam}},\overrightarrow{x_{obj}},t_{acq,soiled}\right)$$

$$=R_{scat}\left(\overrightarrow{r_{cam}},\overrightarrow{x_{obj}},t_{acq,soiled}\right)+R_{clean,exp.norm}\left(\overrightarrow{r_{cam}},\overrightarrow{x_{obj}},t_{acq,soiled}\right)$$

$$\cdot \tau(\alpha_{sun})\cdot \tau(\alpha_{cam})\cdot \frac{\text{GTI}(t_{acq,soiled})}{\text{GTI}(t_{acq,clean})}$$
(4.10)

The equation also considers that the clean and soiled images might have been taken at different times with different illumination situations. This is included in the equation by the ratio of the global tilted irradiances at the time of the respective image acquisition ($GTI(t_{acq,soiled})$, $GTI(t_{acq,clean})$). Equation 4.10 can be reformulated to Equation 4.11 which more clearly describes the transmittance of the soiling layer.

$$\tau(\alpha_{sun}) \cdot \tau(\alpha_{cam}) = \frac{R_{soiled,exp.norm} - R_{scat}}{R_{clean,exp.norm}} \cdot \frac{\text{GTI}(t_{acq,clean})}{\text{GTI}(t_{acq,soiled})}$$
(4.11)

In this equation, τ has to be calculated. The transmission $\tau(\alpha)$ of the soiling layer depends on the angle of incidence α . For normal incidence, the value of τ reaches its maximum τ_0 . For an oblique incidence, the soiling layer effectively appears thicker and the soiling losses will increase. In this work, it is assumed that the transmittance

is described by the effective thickness of the soiling layer as in Equation 4.9. All viewing angles and incident angles are limited to small values so this assumption is expected to hold.

$$1 - \tau(\alpha) = \frac{1 - \tau_0}{\cos \alpha}$$

$$\tau(\alpha) = 1 - \frac{1 - \tau_0}{\cos \alpha}$$
(4.12)

There are more complex models in literature to describe the angular dependence of the soiling on reflecting mirrors, e.g., (Heimsath and Nitz, 2019), but the described approach is used for simplicity. With this assumption, the left side of Equation 4.11 only contains the cosines of the two known angles and the parameter that is to be determined, the transmittance τ_0 . The parameters on the right side of Equation **4.11** are partly known. $R_{soiled,exp,norm}$ is proportional to the red channel of the soiled module's image and $R_{clean,exp.norm}$ to that of the clean reference module. $R_{soiled,exp.norm}$ and $R_{clean,exp.norm}$ have to be compared for the same geometry described by the sun position $\overrightarrow{r_{sun}}$ and $\overrightarrow{r_{cam}}$ the camera's position relative to the PV cell. Of particular interest is the orientation of $\overrightarrow{r_{sun}}$ and $\overrightarrow{r_{cam}}$ to each other. For instance, the most important aspect is how close the camera viewing point is to the direct sun reflex as this might cause over-exposure and direct reflexes. The GTIs are measured and known. R_{scat} is unknown for the moment and will be discussed below. It depends on the properties of the soiling layer including its transmittance τ and the illumination and viewing geometry. It should be mentioned that $R_{soiled,exp.norm}$, R_{scat} , and $R_{clean,exp.norm}$ depend on $\overrightarrow{r_{cam}}$, $\overrightarrow{r_{sun}}$, and $GTI(t_{acqui})$. $R_{soiled,exp.norm}$ and R_{scat} , additionally, depend on the local soiling $\tau_0(\overrightarrow{x_{obj}})$. In the following, it is assumed that $\tau_0(\overrightarrow{x_{obj}})$ is an average over the area of each cell. Equation 4.11 can be simplified further by normalizing to the GTIs.

$$\tau(\alpha_{sun}) \cdot \tau(\alpha_{cam}) = \frac{R_{soiled,GTI,norm} - R_{scat}/GTI(t_{acq,soiled})}{R_{clean,GTI,norm}}$$
(4.13)

With

$$R_{clean/soiled,GTI,norm} = \frac{R_{clean/soiled,exp.norm}}{GTI(t_{aqc,clean/soiled})}$$
(4.14)

4.2.4 Analyze Different Scattering Pathways

To further understand Equation 4.13 and R_{scat} , the underlying scattering pathways are analyzed. There are multiple scattering pathways possible even if only first-order scattering is considered. The scattering pathways are sketched in Figure 4.2. It can be shown by geometrical considerations that the scattering angles are the same for the cases (I, I) and (II, II) as well as for (I, II) and (II, I), respectively. The angles are explained in Tables 4.1 and 4.2.

Considering the four pathways, we now formulate Equation 4.15 describing $L_{\lambda,scat,dir}^{soiled}$, which is the wavelength-dependent radiance of the direct radiation that is scattered once by the soiling particles and reaches the sensor.

TABLE 4.1: Explanation of the different scattering angles and pathways.

Nomenclature	Case Description
(I,I)	The incident irradiance is scattered in the direction of the camera without interacting with the glass cover.
(I,II)	The incident irradiance is scattered in the direction of the module. Then, it is refracted at the air-glass surface. Afterward, the light is reflected at the cell's surface. Then, it is refracted at the glass–air surface. When leaving in the direction of the camera, the irradiance is transmitted through the soiling layer.
(II,I)	The incident irradiance is transmitted through the soiling layer. Then, it is refracted at the air-glass surface. At the cell's surface, the irradiance is reflected. Then, it is refracted at the glass–air surface. When leaving the module, the irradiance is scattered in the direction of the camera.
(II, II)	The incident irradiance is transmitted through the soiling layer. Then, it is refracted at the air-glass surface. When reaching the cell's surface, the irradiance is reflected. Then, it is refracted at the glass–air surface. When reaching the soiling layer for the second time, the light is scattered in the direction of the cell. Then, it is again refracted at the air-glass surface. Afterwards, the light is reflected by the cell surface for a second time. Then, it is refracted at the glass–air surface Finally, it is transmitted through the soiling layer in the direction of the camera.

TABLE 4.2: Comparison of the different scattering angles.

Nomenclature	Case Description
$\theta_{I,I}(\overrightarrow{r_{cam}},\overrightarrow{r_{sun}}) = \theta_{II,II}(\overrightarrow{r_{cam}},\overrightarrow{r_{sun}})$	Angle between camera vector and sun vector; the camera vector is pointing in the direction of the module and the sun vector is pointing away from the module.
$\overline{\theta_{I,II}}(\overrightarrow{r_{cam}},\overrightarrow{r_{sun}}) = \theta_{I,II}(\overrightarrow{r_{cam}},\overrightarrow{r_{sun}})$	Angle between the sun reflex vector and the camera vector; both vectors are pointing away from the module.

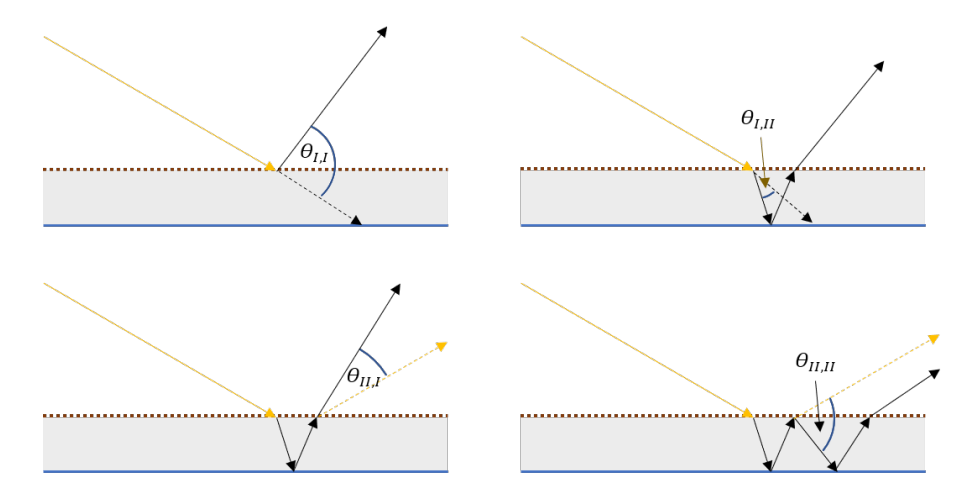


FIGURE 4.2: Sketch to describe the scattering pathways relevant to the measurement method. The cover glass is shown as a gray surface with the soiling layer on top (dotted brown line) and the PV cell below (straight blue line). Shown is the direct radiation coming from the sun as a straight yellow arrow. The black arrow with a straight line shows in which direction the light leaves if it is scattered (camera direction). The dashed yellow or black arrows show the direction relative to which the scattering angle is defined. In the lower two sub-figures, the yellow dashed arrow corresponds to the direct sun reflex.

$$L_{\lambda,scat,dir}^{soiled}\left(\overrightarrow{r_{cam}},\overrightarrow{r_{sun}}\right)$$

$$=L_{\lambda,dir}^{soiled}\left(\overrightarrow{r_{sun}}\right)\cdot\omega$$

$$\cdot\left[\left(1-\tau(\alpha_{sun})\right)\cdot P_{scat}(\theta_{I,I},\lambda)+\left(1-\tau(\alpha_{cam})\right)\cdot\tau(\alpha_{sun})\right]$$

$$\rho_{spec}\cdot P_{scat}(\theta_{I,II},\lambda)+\left(1-\tau(\alpha_{sun})\right)\cdot\tau(\alpha_{cam})\cdot\rho_{spec}$$

$$\cdot P_{scat}(\theta_{II,I},\lambda)+\left(1-\tau(\alpha_{cam})\right)\cdot\tau(\alpha_{sun})\cdot\tau(\alpha_{cam})(\rho_{spec})^{2}$$

$$\cdot P_{scat}(\theta_{II,II},\lambda)\right]$$

$$(4.15)$$

 $L_{\lambda,dir}^{soiled}$ is the wavelength-dependent direct radiance falling on the soiled module. ω is the single scattering albedo, i.e., the ratio of the particles' scattering coefficient to their extinction coefficient. ω describes that only a fraction of the radiation that is not transmitted is scattered. The fraction of the radiation that is not transmitted is described by the terms $(1-\tau)$ which appear for all four summands. P_{scat} is the scattering phase function, describing the probability of a given scattering angle. ρ_{spec} is the reflectance of the cell surface. ω , τ , and ρ_{spec} are considered to be spectrally weighted averages over the wavelength.

When the drone is flying above the modules, the angle $\theta_{I,I}$ is typically corresponding to backward or sideward scattering while $\theta_{I,II}$ is corresponding to forward scattering. Scattering is strongly direction-dependent and after averaging over wavelengths and particle sizes, forward scattering is dominant over other scatter directions. This condition is ensured by selecting images with a specific geometrical configuration. For this reason, all terms containing $P_{scat}(\theta_{I,I},\lambda)$ or $P_{scat}(\theta_{II,II},\lambda)$ are neglected and the equality of $\theta_{I,II}$ and $\theta_{II,I}$ is considered to lead to Equation 4.16.

$$L_{\lambda,scat,dir}^{soiled}\left(\overrightarrow{r_{cam}},\overrightarrow{r_{sun}}\right)$$

$$=L_{\lambda,dir}^{soiled}\left(\overrightarrow{r_{sun}}\right)\cdot\omega\cdot\rho_{spec}\cdot P_{scat}(\theta_{I,II},\lambda)$$

$$\left[\left(1-\tau(\alpha_{cam})\right)\cdot\tau(\alpha_{sun})+\left(1-\tau(\alpha_{sun})\right)\cdot\tau(\alpha_{cam})\right]$$
(4.16)

Equation 4.16 is also valid for irradiances instead of radiances when introducing an additional proportionality factor c. Equation 4.17 is obtained.

$$L_{\lambda,scat,dir}^{soiled}\left(\overrightarrow{r_{cam}},\overrightarrow{r_{sun}}\right)$$

$$= c \cdot \text{DNI}_{\lambda} \cdot \omega \cdot \rho_{spec} \cdot P_{scat}(\theta_{I,II},\lambda)$$

$$\left[(1 - \tau(\alpha_{cam})) \cdot \tau(\alpha_{sun}) + (1 - \tau(\alpha_{sun})) \cdot \tau(\alpha_{cam}) \right]$$
(4.17)

The wavelength-dependent irradiance of the scattered direct radiation that hits the pixel sensor is denoted $E^{soiled}_{\lambda,scat,dir}$ and the wavelength-dependent direct normal irradiance that hits the module is denoted DNI $_{\lambda}$. Coming back to the calculation of R_{scat} , one can write the following:

$$R_{scat} = \int_{\lambda_{min}}^{\lambda_{max}} \epsilon \cdot E_{\lambda,scat,dir}^{soiled} \left(\overrightarrow{r_{cam}}, \overrightarrow{r_{sun}}\right) d\lambda$$

$$= \int_{\lambda_{min}}^{\lambda_{max}} \epsilon \cdot c \cdot \omega \cdot \rho_{spec} \cdot DNI_{\lambda}(\alpha_{sun}) \cdot P_{scat}(\theta_{I,II}, \lambda)$$

$$\left[(1 - \tau(\alpha_{cam})) \cdot \tau(\alpha_{sun}) + (1 - \tau(\alpha_{sun})) \cdot \tau(\alpha_{cam}) \right] d\lambda$$
(4.18)

c, ω , and ρ_{spec} can be combined to a new constant c'.

$$R_{scat} = \int_{\lambda_{min}}^{\lambda_{max}} c' \cdot \epsilon \cdot DNI_{\lambda}(\alpha_{sun}) \cdot P_{scat}(\theta_{I,II}, \lambda)$$

$$\left[(1 - \tau(\alpha_{cam})) \cdot \tau(\alpha_{sun}) + (1 - \tau(\alpha_{sun})) \cdot \tau(\alpha_{cam}) \right] d\lambda$$

$$= c' \cdot \left[(1 - \tau(\alpha_{cam})) \cdot \tau(\alpha_{sun}) + (1 - \tau(\alpha_{sun})) \cdot \tau(\alpha_{cam}) \right]$$

$$\cdot \int_{\lambda_{min}}^{\lambda_{max}} \epsilon \cdot DNI_{\lambda}(\alpha_{sun}) \cdot P_{scat}(\theta_{I,II}, \lambda)$$

$$(4.19)$$

In the following step, it is assumed that the remaining integral is proportional to the DNI multiplied by an integral just over ϵ and P_{scat} . The proportionality factor c' therefore changes to c''.

$$R_{scat} = c'' \cdot \left[(1 - \tau(\alpha_{cam})) \cdot \tau(\alpha_{sun}) + (1 - \tau(\alpha_{sun})) \cdot \tau(\alpha_{cam}) \right] \cdot DNI$$

$$\cdot \int_{\lambda}^{\lambda_{max}} \epsilon \cdot P_{scat}(\theta_{I,II}, \lambda)$$
(4.20)

In a final step, c'' and the integral are combined to define the function $c_{scat}(\overrightarrow{r_{sun}}, \overrightarrow{r_{cam}})$.

$$R_{scat} = \left[(1 - \tau(\alpha_{cam})) \cdot \tau(\alpha_{sun}) + (1 - \tau(\alpha_{sun})) \cdot \tau(\alpha_{cam}) \right] \cdot DNI$$

$$\cdot c_{scat} \left(\overrightarrow{r_{sun}}, \overrightarrow{r_{cam}} \right)$$
(4.21)

The empirical scattering function $c_{scat}\left(\overrightarrow{r_{sun}},\overrightarrow{r_{cam}}\right)$ describes the probability of different scattering directions. Equations 4.13 and 4.21 can be combined to isolate the empirical scattering function $c_{scat}\left(\overrightarrow{r_{sun}},\overrightarrow{r_{cam}}\right)$.

$$c_{scat}\left(\overrightarrow{r_{sun}}, \overrightarrow{r_{cam}}\right) = \frac{R_{soiled,GTI,norm} - R_{clean,GTI,norm} \cdot \tau(\alpha_{cam}) \cdot \tau(\alpha_{sun})}{\left[\left(1 - \tau(\alpha_{cam})\right) \cdot \tau(\alpha_{sun}) + \left(1 - \tau(\alpha_{sun})\right) \cdot \tau(\alpha_{cam})\right] \cdot \frac{\text{DNI}(t_{acq,soiled})}{\text{GTI}(t_{acq,soiled})}}$$

$$(4.22)$$

Equation 4.22 can also be solved for τ_0 , the value of the soiling transmission for $\alpha = 0^{\circ}$ when using Equation 4.12. All results for the soiling loss later on refer to normal incidence ($\alpha = 0^{\circ}$).

$$\tau_{0} = 1 - \frac{-b_{1} + \sqrt{b_{1}^{2} - 4 \cdot b_{0} \cdot b_{2}}}{2 \cdot b_{0}}$$

$$b_{0} = \frac{R_{clean,GTI,norm} - 2 \cdot c_{scat}(\overrightarrow{r_{sun}}, \overrightarrow{r_{cam}}) \cdot \frac{DNI(t_{acq,soiled})}{GTI(t_{acq,soiled})}}{\cos(\alpha_{cam}) \cdot \cos(\alpha_{sun})}$$

$$b_{1} = \frac{\cos(\alpha_{cam}) + \cos(\alpha_{sun})}{\cos(\alpha_{cam}) \cdot \cos(\alpha_{sun})} \cdot c_{scat}(\overrightarrow{r_{sun}}, \overrightarrow{r_{cam}}) \cdot \frac{DNI(t_{acq,soiled})}{GTI(t_{acq,soiled})} - R_{clean,GTI,norm}$$

$$b_{2} = R_{clean,GTI,norm} - R_{soiled,GTI,norm}$$

$$(4.23)$$

With this set of equations, it is possible to determine the soiling ratio for a given image as described in the next section. First, images of the clean reference module will be used to calculate the expected background signal corresponding to a clean PV module for any geometry (see section 4.3.1). $R_{clean,GTI,norm}$ can then be determined for any camera position. Afterwards, the images of the soiled reference module are analyzed, and using the measured τ_0 for this reference module, c_{scat} can be determined in dependence of the geometry (see section 4.3.2). Finally, the soiling loss can be measured for a third module (see section 4.3.3).

4.3 Calibration Measurements

Before the method is applied to analyze the soiling losses of a PV module with unknown soiling loss, two calibration measurements are performed with a clean and a soiled module with known soiling loss.

4.3.1 Determination of Expected Background Signal Corresponding to a Clean PV Module

The goal is to determine the expected background signal corresponding to a clean PV module $R_{clean,GTI,norm}$ in dependence on the geometry defined by $\overrightarrow{r_{cam}}$ and $\overrightarrow{r_{sun}}$. Consequently, before the measurement flight, one module is cleaned. Images of this module are captured from various perspectives, which can be achieved, e.g., using a spiral flight route. Every cell of the clean module is examined individually. For each image and each cell, the geometry and the brightness are determined. $\overrightarrow{r_{cam}}$ $\overrightarrow{r_{sun}}$ are reduced to the angle between the camera vector and the sun reflex vector $\theta_{cam,sunrefl}$ (the scattering angle) and the angle between the camera vector and the module normal vector α_{cam} to describe the geometry. The idea is to model the expected brightness for a clean module as a function of these two angles. Afterwards, the clean brightness can be calculated and subtracted as a background signal for the images of other PV modules that are to be evaluated. The method requires many images from different perspectives. For example, assuming 100 reference images and one clean reference module with 60 cells results in 6000 data points consisting of the brightness and the two angles mentioned above.

After filtering the data points as described in the previous section, a polynomial fit of second order is performed to describe $R_{clean,GTI,norm}$ as a function of $\theta_{cam,sunrefl}$ and α_{cam} . Using this fit, the expected brightness of an imaginary clean module under any geometry can be calculated. The influence of this fit on the calibration is discussed later in section 4.6 and visualized in 4.6. Note that the same $\theta_{cam,sunrefl}$ can be obtained from various combinations of $\overrightarrow{r_{cam}}$ and $\overrightarrow{r_{sun}}$. This means in particular that even when the sun position has changed over time, one can still compare images of the clean modules with an early timestamp with images of the soiled module with a later timestamp.

4.3.2 Determination of the Scattering Behavior

The next intermediate goal is to determine c_{scat} in dependence on the geometry defined by $\overrightarrow{r_{cam}}$ and $\overrightarrow{r_{sun}}$. Therefore, the scattering calibration is performed after the clean calibration. It is required for the evaluation of other modules. One soiled module with known soiling loss is considered. It should be homogeneously soiled, and the soiling losses have to be determined using electrical measurements as described above. As in the case of the background signal, many images are captured from various perspectives. In the case that the clean and soiled reference modules are located directly next to each other, one flight is sufficient to perform both calibrations. The geometry is used to evaluate the previously determined background calibration function to obtain the clean background signal for each cell and each image. By comparing the actual RGB value of the soiled cells and the clean background values, the brightness increase is determined. Considering the geometry, the electrical soiling loss, the irradiances at the image acquisition times, and the brightness increases enables the calculation of the scattering function c_{scat} according to Equation 4.22 from the previous section. First, discrete values are calculated for each cell and image. Afterwards, the scattering

function is described in dependence on $\theta_{cam,sunrefl}$ and $\theta_{cam,sun}$, the angle between the camera vector and the sun vector using a polynomial fit of the second order. The scattering calibration and its approximations are discussed in more detail in Chapter 4.6.

4.3.3 Calculation of Soiling Loss

After the calibration flight and its evaluation $R_{clean,GTI,norm}(\theta_{cam,sunrefl},\alpha_{cam})$ and $c_{scat}(\theta_{cam,sunrefl},\theta_{cam,sun})$ are known. Now, a flight over the modules for which the soiling loss should be measured can be performed. Equation 4.23 is then used together with the background signal $R_{clean,GTI,norm}$ and c_{scat} to determine the soiling loss of each cell of the PV modules as seen in each image. One soiling loss value is obtained for every cell and each image. Values for a cell that are deviating by more than two standard deviations from the median for this cell are excluded to reduce the impact of noise and outliers. Afterwards, the arithmetic average is again calculated. Finally, one obtains the soiling loss for each cell as an average of the soiling losses from each image for this cell that remain after the filtering. The soiling loss on a module level is then determined as the average of the cell soiling losses. This approach neglects electrical mismatch. However, it has been confirmed by the electrical model developed in Chapter 6 that the soiling losses discussed here are sufficiently small and sufficiently homogeneous so that electrical mismatch can indeed be neglected.

4.4 Measurement Procedure and Data Processing

4.4.1 Measurement Procedure

First, the reference measurement is performed. A spiral flight over the clean and the soiled reference module is carried out. Both modules are located directly next to each other so that one flight is sufficient to cover both modules. A spiral flight has the advantage that multiple different perspectives are included.

Afterwards, the measurement flight is performed. For the first and the second measurement campaign, this is also a spiral flight. For the third campaign, the flight pattern was a straight flight in the east-west direction. Each campaign is discussed individually below.

According to the spiral route, the drone continues to go further to the outside step by step. Simultaneously, the drone starts at its maximum height and decreases the height the further it goes to the outside of the spiral. The electrical power of the four modules, the GTI, and the DNI are recorded permanently. Additionally, for modules 2 and 3, the IV curve is traced. These data are recorded every 10 s (see Chapter 3). These values are recorded on the measurement day itself and also on a sunny reference day on which all devices are clean. The comparison to this day allows the determination of the reference soiling losses. The drone captures both raw images and RGB images. Only the raw images are used for the evaluation. Images are captured every 3 to 5 s. The images contain metadata such as exposure time, aperture, and ISO. For the flight routes used, one pixel in an image corresponds to approximately 6 mm in the module plane in reality.

4.4.2 Data Processing

The camera described in Chapter 3 is used. Also, the vignetting correction, the gamma correction, and the used photogrammetry methods are described there.

The orthoimages of each module are cut into individual cells. This is performed by applying a mask that aligns with the modules' edges. The position of each module is given in a reference coordinate system which allows the distinction of all modules. For each orthoimage, the sun position is calculated from the timestamp. The camera position relative to the cell is calculated. This information is sufficient to describe the geometry. The brightness of each cell of each orthoimage is extracted and normalized to the GTI at a certain timestamp.

Afterwards, the calibrations and the evaluation are performed in the following order. First, the clean reference module is analyzed (see section 4.3.1) followed by the soiled reference module (see section 4.3.2). Afterwards, it is possible to analyze all other modules. For every image of a given cell, a soiling loss is calculated. The final soiling value of a cell is the filtered average over all images to exclude outliers (see section 4.3.3).

To calculate the electrical reference loss SL_{ref} , two methods from Section 2.2.1 are used. The calculation is discussed in detail in Appendix A.1, A.2, and A.3.

Note that the electrically measured reference soiling loss is an input for the presented optical method. Therefore, the accuracy of the optical method is limited by the accuracy of the electrical reference measurement. This is also true for other method from the literature, e.g. for the study presented by (Mehta et al., 2018) and by (Yang, Ji, and Guo, 2021) and will be true for any optical method that requires a calibration with electrical reference measurements.

4.5 Results and Discussion

All flights performed on the three days are evaluated. Below, each flight is discussed individually.

4.5.1 First Campaign

Figure 4.3 shows the setup during the first measurement campaign. Module 1 (lower right of the four central modules) is used as the clean reference module. Module 2 (upper right of the four central modules) is used as the soiled reference module.



FIGURE 4.3: This figure show the setup during the first campaign.

Figure 4.4 shows the results of the cell-resolved soiling loss calculation. The optically measured and the electrical reference value of the soiling loss is stated right next to each module in Figure 4.4. The optical method overestimates the soiling loss of the clean reference module by 0.3% (absolute) and overestimates the soiling loss of the soiled reference module by 0.6%. This is explained by the fact that different images are used for the calibration and the evaluation. For modules 3 and 4 the optical method once overestimates the soiling loss by 0.4% and once underestimates the soiling loss by 1.0%. The optical model manages to distinguish the soiled modules from the clean module and also manages to identify more heavily soiled cells with a given module. For example the lower row of cells in the upper two module (module 2 and module 4) are identified. The deviations obtained on module level are 1% absolute or lower. This is roughly the uncertainty with which the electrical reference measurement can determine the soiling loss.

Figure 4.5 shows the optically measured soiling loss against the electrically measured reference soiling loss for every image. In contrast to Figure 4.4, the optically measured soiling loss SL_{cam} in Figure 4.5 is module resolved and not cell resolved and is not yet averaged over all images. As can be seen, the calculated module soiling loss is similar for every image and there are no major outliers.

According to the results, the soiling distribution of each module seems to be roughly homogeneous. However, there are a few cells that have a different soiling loss than their neighboring cells. In particular, the lower right cell of module 2 and the upper right cell of module 3 have a higher soiling loss. This observation in the results corresponds to the expectation from the photo shown in Figure 4.3. One can clearly see that the upper right cell of the upper left module is brighter and more soiled than its neighbors. The same applies for the lower right cell of the upper right module.

41

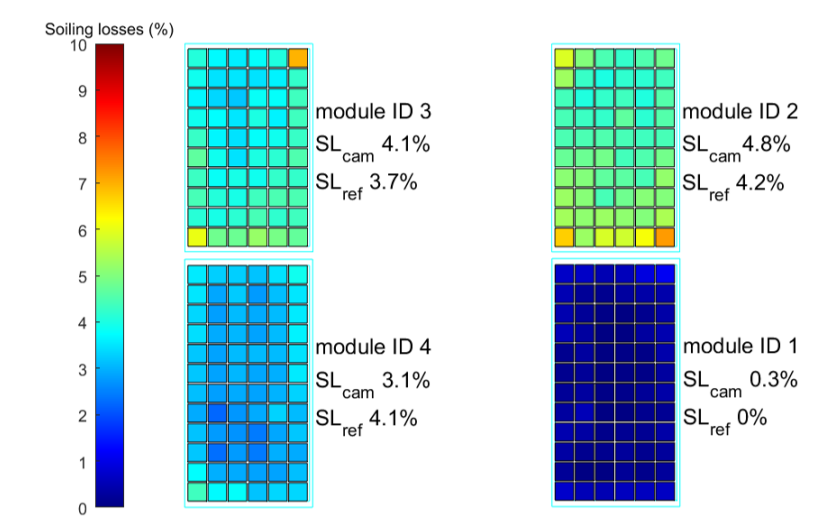


FIGURE 4.4: Results of the first flight performed on the 8 April 2022. The color marks the calculated soiling loss. The lower right module (1) was used as the clean calibration module while the upper right (2) was used as soiled reference module. The upper numbers label the modules. The number in the middle states the optically measured soiling loss using the drone images while the lower number is the electrical reference loss.

The calculated soiling loss of the clean module is 0.3% and the soiling loss of the soiled reference module is 4.8%. These values differ slightly from the electrical reference values that were used to calibrate the method (0% and 4.2%, respectively). These differences are explained by the fact that the results shown here were created by evaluating different images from different perspectives compared to the calibration. The calculated soiling loss for the upper left module is 4.1% which is close to the electrically measured reference value of 3.7%. The measured value of the lower left module is 3.1% and differs more from the electrical reference value of 4.1%. This might be explained by the fact that the upper modules were soiled with a different soiling type compared to the lower left module.

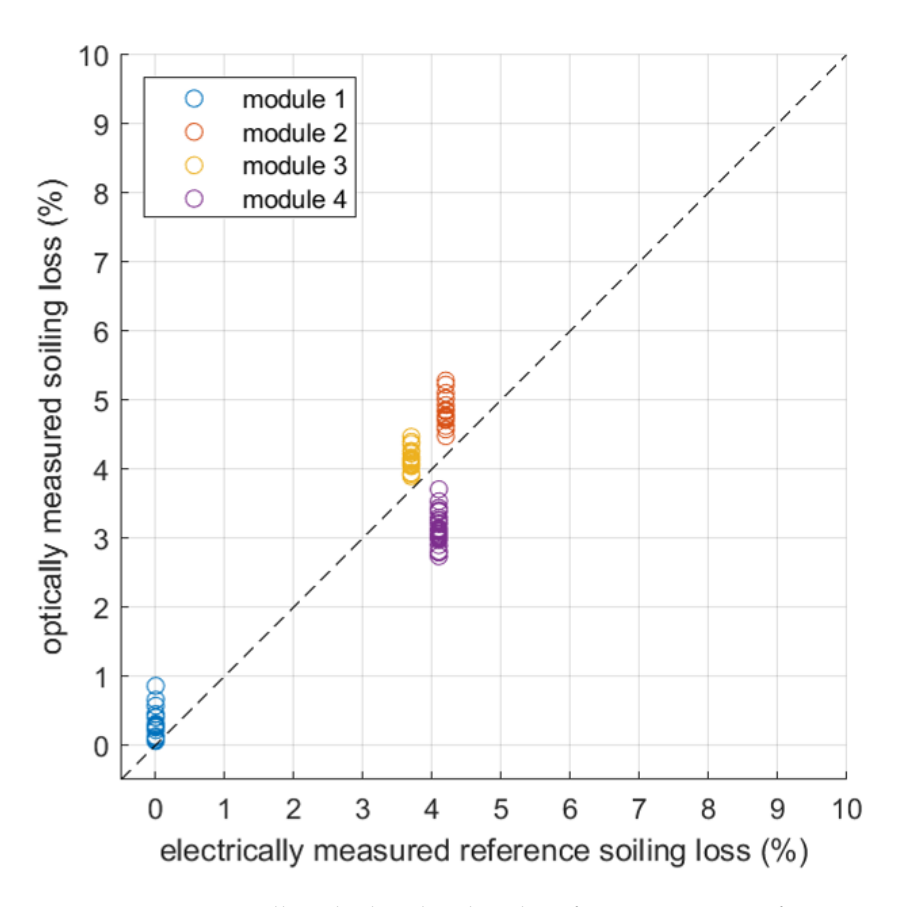


FIGURE 4.5: Optically calculated soiling loss for every image of every module against the electrically measured reference soiling loss. The standard deviations for the soiling loss on module level for modules 1 to 4 are 0.14%, 0.22%, 0.20%, and 0.18%, respectively. The results belong to the first flight performed on 8 April 2022.

4.5.2 Second Campaign

During the second campaign the lower right as well as the upper right module were both clean. Figure 4.6 shows the setup during the second campaign. Figure 4.7 summarizes the results of the first measurement flight of the second campaign. The soiling of the first validation module is determined with a deviation of 0.5% absolute. The soiling of the second validation module is determined with a deviation of 0.9% absolute.



FIGURE 4.6: This figure show the setup during the second campaign.

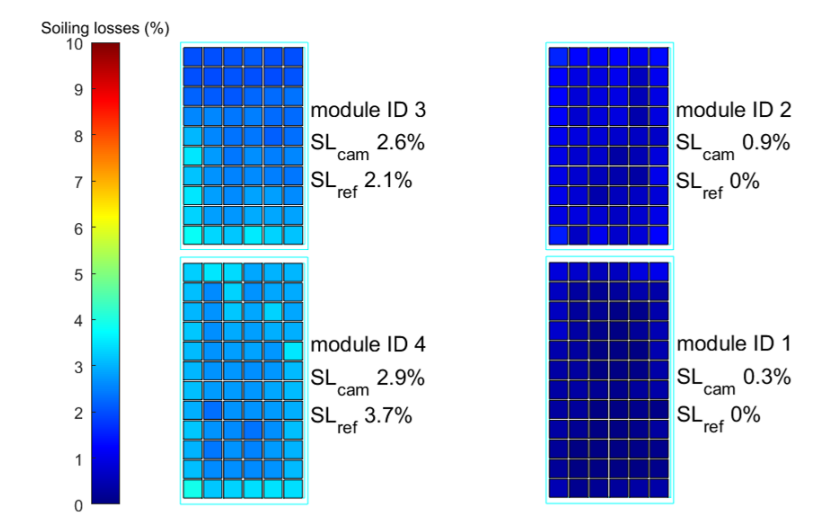


FIGURE 4.7: Result plot of the first measurement flight of the second campaign. The lower right module was chosen to be the clean reference module while the lower left module was chosen to be the soiled reference module. The upper numbers label the modules. The number in the middle states the optically measured soiling loss while the lower number is the electrical reference loss.

4.5.3 Third Campaign

For the third campaign, the modules were artificially soiled with gypsum. The gypsum was mixed with water and the mixture was then deposited on the module with a towel. The operating temperature of the module led to a quick drying of the mixture. The artificial soiling was as homogeneously distributed as possible and was considered to be sufficiently homogeneous by simple visual inspection. After obtaining the results of this measurement, the above-mentioned electrical model confirmed that the soiling was homogeneous enough to neglect additional mismatch losses. Figure 4.8 shows the artificially soiled setup during the measurement.



FIGURE 4.8: This figure show shows the setup during the third campaign.

Figure 4.9 summarizes the results of the measurement flight of the third campaign. The soiling loss of the first validation module is determined with a deviation of 2.3% absolute. The soiling of the second validation module is determined with a deviation of 1.7% absolute.

The larger deviations in this case might be explained by the fact that in this experiment, artificial soiling was used as explained in the discussion of Figure 4.10.

45

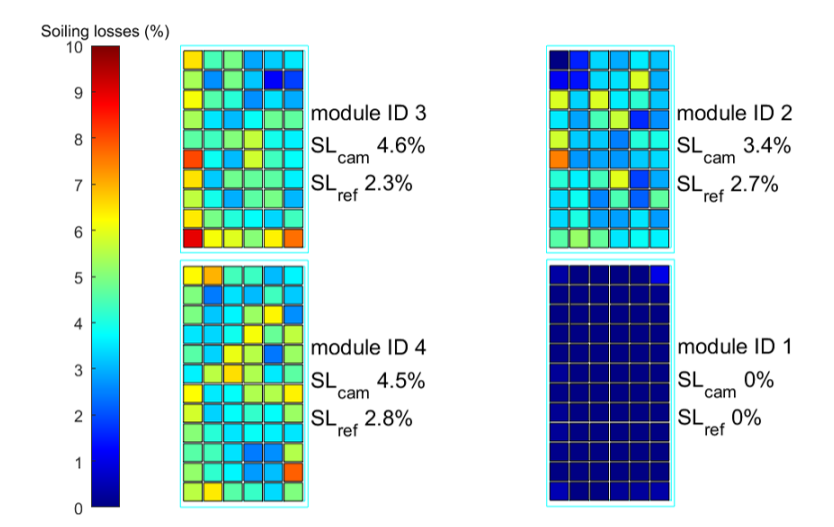


FIGURE 4.9: Result plot of the first measurement flight of the third campaign. The lower right module was chosen to be the clean reference module while the upper right module was chosen to be the soiled reference module. In this campaign, the modules were soiled artificially with gypsum. The artificial soiling was not as homogeneously distributed as was the case for the previous campaigns with natural soiling. The upper numbers label the modules. The number in the middle states the optically measured soiling loss while the lower number is the electrical reference loss.

4.5.4 Summary

Figure 4.10 summarizes the results of all measurements performed. It shows the optically measure soiling losses against the electrically measured reference soiling losses. The values are presented on a module level. The RMSE of the measured soiling loss over all measurements is 0.93% absolute and the MBE is 0.33% absolute.

The red dot refers to the above-discussed measurement for which the test and soiled reference modules had a different soiling type. This different soiling type explains the higher deviations. The blue triangle and the dark red rhombus refer to the third measurement campaign where the modules were soiled artificially with gypsum. The artificial soiling is not as homogeneous as the natural soiling. Hence, the approximation for the calibration that all cells of the soiled reference module have the same soiling level is less adequate and higher deviations can be explained.

One can see that in some cases the method overestimates and in other cases it underestimates the soiling losses. According to (Dunn et al., 2013; Peterson, Chard, and Robinson, 2022), the uncertainty of the electrical measurements of the soiling loss is about 1% absolute. This is the same magnitude as the calculated RMSE. There are not yet enough data to state whether the bias error of the method is systematic or not. The method is qualitatively able to distinguish between stronger and less soiled modules and also stronger and less soiled cells. Additionally, it can give a reasonable estimation of the absolute soiling value.

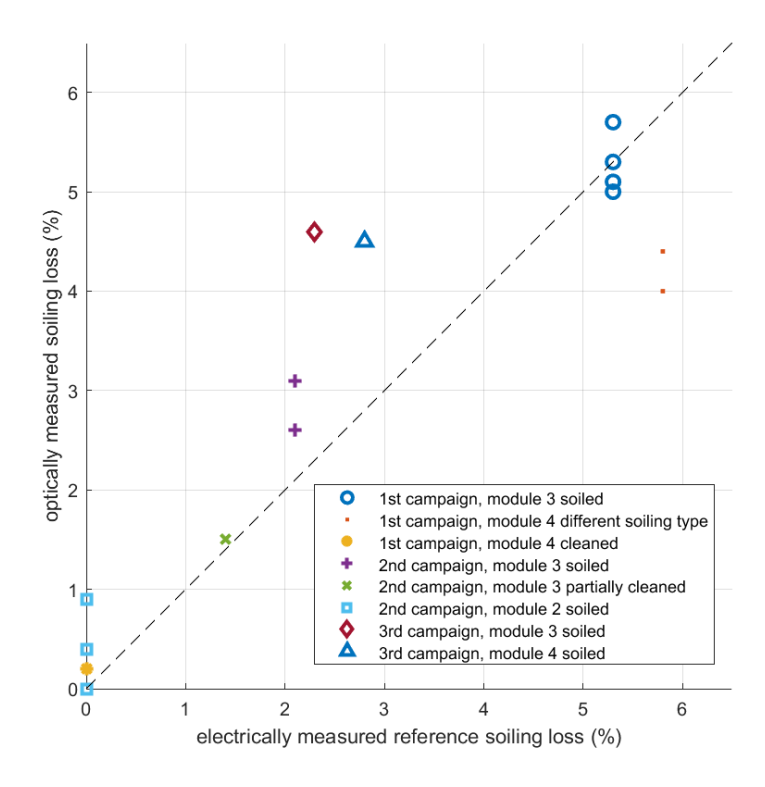


FIGURE 4.10: Optically measured soiling losses based on the images plotted against the electrically measured reference soiling losses for several modules and the three measurement campaigns performed. For some campaigns and modules, several identical markers are seen referring to different flights within the same campaign.

47

There is no obvious benchmark model that could be compared with the proposed model because of its novelties. The most similar model is probably the AI model by Yang (Yang et al., 2024) that calculates the soiling losses from just seeing an image. The authors state that the relative prediction error is below 10% if the actual soiling loss exceeds 8% absolute. According to Figure 4 of their paper, this is the case in a minority of the cases. Unfortunately, the average soiling loss, the RMSE, the MBE, and the MAE are not stated. Figure 4 of the Yang paper is similar to Figure 4.10 here. Yang has analyzed a wider range of soiling losses. In the range up to 8% absolute soiling loss, the deviation between the measurement and the prediction seem to be comparable to the proposed method. When making this comparison, one has to be extremely careful and has to keep in mind that both models were tested on different datasets. Yang et al. used the same camera and the same perspectives for all images. Additionally, the same modules were used for training and evaluation. All in all, both methods should be tested under various conditions to allow a fair comparison.

4.6 Visualization of the Calibration Functions

In this section, the calibration of the clean background signal and the calibration of the scattering signal are described. As an example, the first flight of the first campaign is chosen.

4.6.1 Clean Background Calibration

After performing the calibration flight, one obtains the brightness of the cells of the clean module. The brightnesses are averaged over the cells' areas and are then normalized to the exposure time and the GTI present at the time of capturing the image. These normalized brightnesses are then available for different cells, camera positions, and different sun positions. Figure 4.11 visualizes the second-order polynomial fit that is performed to describe the normalized brightness in dependence on $\theta_{cam,sunrefl}$ and α_{cam} .

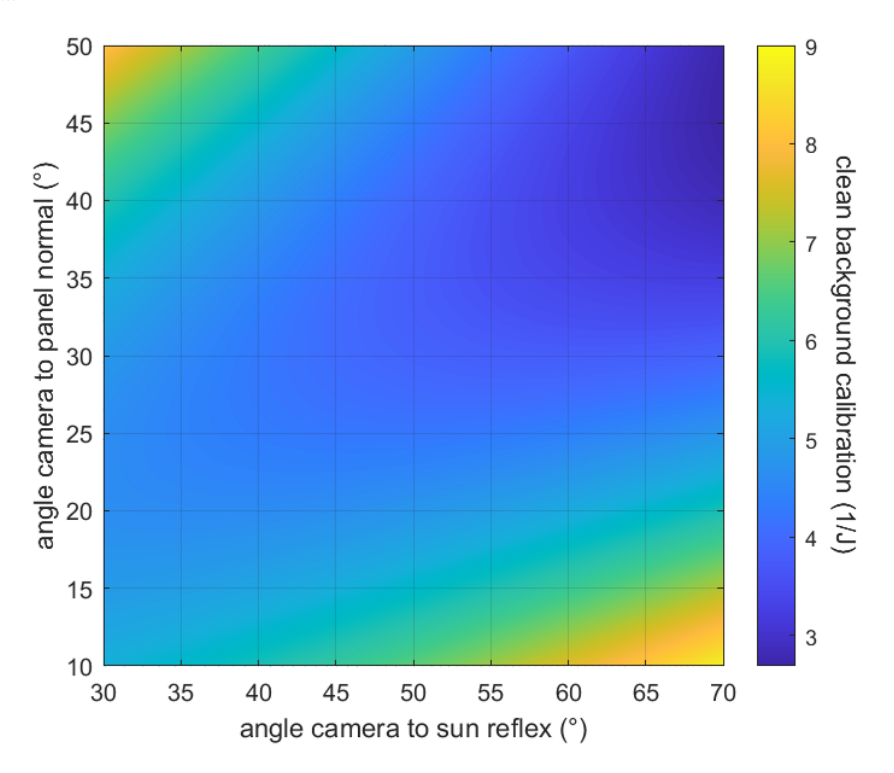


FIGURE 4.11: Clean background calibration for the first measurement flight of the first campaign. The x-axis shows the angle between camera and sun reflex vector $\theta_{cam,sunrefl}$ while the y-axis shows the angle between camera vector and panel normal vector α_{cam} . The calibration function is a polynomial of second order of the above-mentioned angles. The calibration function gives basically the expected brightness normalized to GTI and exposure time, which explains the unit.

Figure 4.12 shows the relative deviations between the normalized brightnesses that are used to create the clean background calibration and the brightnesses that would be expected according to the polynomial function (the fit values are subtracted from the measured values and divided by the fit values). For every image, one obtains 72 data points since the clean module has 72 cells. These 72 cells have very similar angles as they are spatially very close to each other. The deviations between different cells from the same image are roughly on the same level as deviations for the same cell but from the next image. The fact that some cells within a given image show

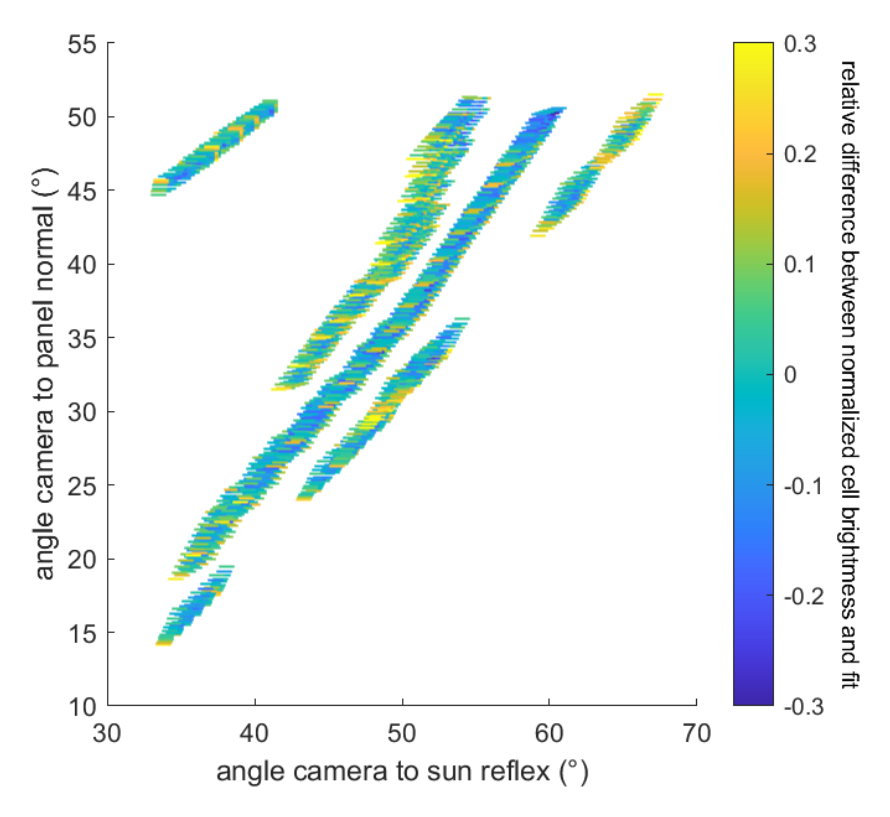


FIGURE 4.12: Relative difference between the normalized brightnesses that are used to create the clean background calibration and the expected values according to the fit.

different brightnesses than others can be attributed to the fact that some cells are slightly brighter or darker than others in reality. Also, the masking of cell in-between spaces cannot be performed perfectly so that this space might influence some cells more than others. There is no sharp edge between the cell and the in-between space in the images. Rather, there is a continuous drop in brightness when one moves from the in-between space towards the cell.

The relative deviation of 30% observed for some points in Figure 4.12 might seem alarming at first. By analyzing Equation 4.23, one can see that it is less dramatic than it seems at first glance. The coefficient b_2 depends on the clean calibration value $R_{clean,GTI,norm}$ and on $R_{soiled,GTI,norm}$. However, as an example for a soiling loss of 5%, $R_{clean,GTI,norm}$ is typically three times bigger than $R_{clean,GTI,norm}$ so that the relative deviation for b_2 will be less than 30%. In the equations for b_0 and b_1 , the factor $\frac{\text{DNI}(t_{acq,soiled})}{\text{GTI}(t_{acq,soiled})}$ is relatively close to 1. Both equations are dominated by c_{scat} which is typically 10 times bigger than $R_{clean,GTI,norm}$ as one can extract from Figures 4.11 and 4.13, so that the relative deviation for b_0 and b_1 will be significantly below 30%. Finally, one obtains also that the deviation for τ_0 will be less than 30%.

4.6.2 Scattering Calibration

After performing the calibration flight, one obtains images of the cells of the soiled reference module from various perspectives. As these perspectives, the soiling loss of this module, and the clean background calibration are already known, one can use Equation 4.22 to calculate the discrete values of the scattering calibration function c_{scat} for each cell and image. It is assumed as an approximation that the module is homogeneously soiled and that the reference soiling loss on the module level can be

used for every cell. Hence, one obtains a data point for each cell and image. Then, a polynomial fit of the second order is created to describe the scattering behavior as a function of $\theta_{cam,sunrefl}$ and $\theta_{cam,sun}$. Figure 4.13 visualizes this polynomial.

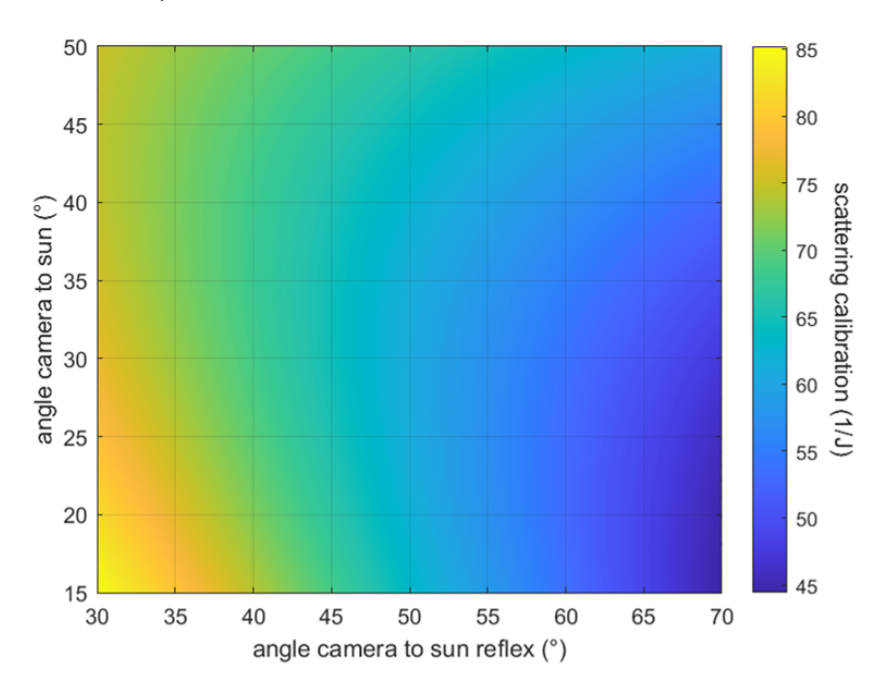


FIGURE 4.13: Scattering calibration of the first flight of the first campaign. The x-axis shows the angle between camera vector and sun reflex vector $\theta_{cam,sunrefl}$ while the y-axis shows the angle between camera vector and sun vector $\theta_{cam,sun}$. The color bar shows the scattering calibration parameter c_{scat} .

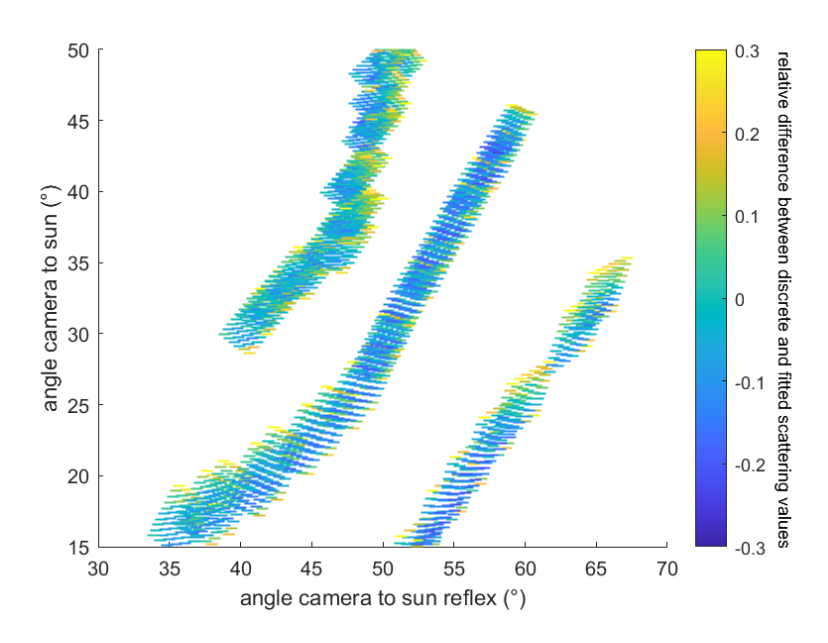


FIGURE 4.14: Relative difference between the discrete scattering values and the scattering values expected according to the scattering calibration function.

Figure 4.14 shows the relative differences between the discrete scattering values

51

that were used to create the fit and the values that would be expected according to the fit itself. One can see that the fit in general describes the data quite well. On the other hand, it is observed that on the edge of each of the line shapes' point groups in the figure, there are some points with a higher positive deviation. This indicates that for some of the outer cells in the module, the deviations are higher than for the others. This is explained by the module not being exactly homogeneously soiled as assumed when using the same τ_0 for all cells for the calculation of c_{scat} . Figures 4.3 and 4.4 confirm that the lower row of cells in module 2 is slightly more soiled than the other cells in the module. One must be aware of this limitation of the method which helps to understand the found deviations. However, the relatively low deviations shown in Figure 4.10 indicate that the homogeneity of the soiling of the soiled reference modules was low enough for the reported measurement campaigns to obtain useful results. Also, the electrical data are only available on the module level and using this soiling loss for each cell is only an estimate of the reference soiling loss on the cell level. In case that the soiling of the soiled reference module is too inhomogeneous, an iterative determination of c_{scat} could be used.

4.7 Conclusions

This Chapter has presented a new method to optically measure the soiling loss of PV modules soiled with dust with high spatial resolution. The method is capable of properly estimating the soiling loss, with an RMSE of 0.93% absolute in the validations. Individual cells with a higher soiling can be identified. Also, on the module level, a qualitative distinction between more and less soiled modules is possible.

The method's calibration requires two reference measurements of a clean and a soiled module. The calibration is performed before every individual measurement. The brightnesses of the clean module are extracted from various perspectives and this is also performed for the soiled reference module for which the soiling losses are also determined electrically. The soiled module is typically brighter as there is more light scattering at the module's surface. Conclusions about the scattering behavior of the dust on top of the module are drawn from the images. After understanding this behavior, it is possible to evaluate other modules.

As the method is based on analyzing drone images, it could be applied to a larger scale and could potentially cover entire PV plants. Currently, the method calculates the soiling loss on a cell level, which allows the consideration of mismatch effects within the modules. When modules are connected in a series in bigger parks, there are additional mismatch losses from module to module. These losses can also be considered when knowing the soiling loss with a spatially high resolution. A combination of this method with thermography measurements enables the distinction between soiling-based and defect-based hotspots.

Near-future plans consist of testing the method on a larger scale. Chapter 5 presents another method that was developed to also detect other kinds of soiling beyond dust. These are inhomogeneous soiling types like bird droppings and leaves, and potentially also snow. The two methods are foreseen to be combined in the near future. Simplifying the method's calibration is also a goal. Additionally, it is planned to further investigate the properties of the calibration function. For example, it might be possible to create a calibration that can be performed once and does not have to be repeated for every measurement campaign. This could enhance the practicability of the method as there would no longer be the need to measure the individual power of one homogeneously soiled module.

Chapter 5

Optical Measurement of Spatially Inhomogeneous Soiling

The previously described and developed measurement method for the soiling type dust follows an analytical approach. The scattered light that falls into the camera is quantified and the soiling-based electrical loss is derived. This approach is possible because dust usually consists of small particles which lead to Mie scattering. This measurement method is not generally applicable for measuring other types of soiling. This Chapter deals with the development of a measurement method for inhomogeneous soiling. This refers to all types of soiling that can be interpreted as larger objects on the module surface. For example, there may be leaves or bird droppings on the module. A plausible approach to solving this general task is to first detect the soiling and segment it afterward.

In Chapter 2 some studies have already been presented that investigated the soiling loss estimation from images (Mehta et al., 2018), (Cavieres et al., 2022), (Zhang et al., 2021), and (Yang et al., 2024). The authors of these studies also used classical computer vision methods as an intermediate step in their analyses. These studies additionally presented ways of distinguishing different soiling types.

Two possible enhancements of the literature methods should be addressed here. When the soiling distribution is known, it is possible to determine the electrical mismatch analytically. This is done by considering the module as a serial connection of the individual cells with individual parameters (see Chapter 6). The studies mentioned above thus solve a problem with AI, which can also be solved analytically. This analytical approach will be introduced here to potentially achieve greater accuracy and reduce computational efforts. A second limitation of (Mehta et al., 2018), (Cavieres et al., 2022), (Zhang et al., 2021), and (Yang et al., 2024) is that the training data set is limited. It lacks generality, e.g. in terms of different module types, viewing perspectives, and soiling types. By applying transfer learning to already existing detection and segmentation methods it is intended to achieve better general applicability with a relatively small transfer training data set.

5.1 Methodology

Figure 5.1 illustrates the workflow of the method. The images of the soiled PV modules are transferred into orthoimages as described in Chapters 3 and 4. In the second step, the soiling is detected on the orthoimages. In the next step the soiling is detected with a method based on the open-source software YOLO (You Only Look Once) (Redmon et al., 2016; Redmon and Farhadi, 2017; Redmon and Farhadi, 2018; Li et al., 2022; Wang, Bochkovskiy, and Liao, 2023; Bochkovskiy, Wang, and Liao, 2020). In the following step, the detected soiling is then segmented by a method based on the open source software SAM (Segment Anything Model) (Kirillov et al., 2023). Both methods use transfer learning and are described in more detail in the next section 5.1.1. YOLO and SAM have already been extensively trained on large data sets. By applying transfer learning, these models should also be applied for the detection of soiling on PV modules.

Afterwards, the soiling is classified into different categories. The next step is to assign a transmittance to every soiling type and soiling spot. This allows the calculation of a cell-resolved averaged soiling transmittance. Finally, the electrical mismatch can be considered and the total soiling loss is calculated.

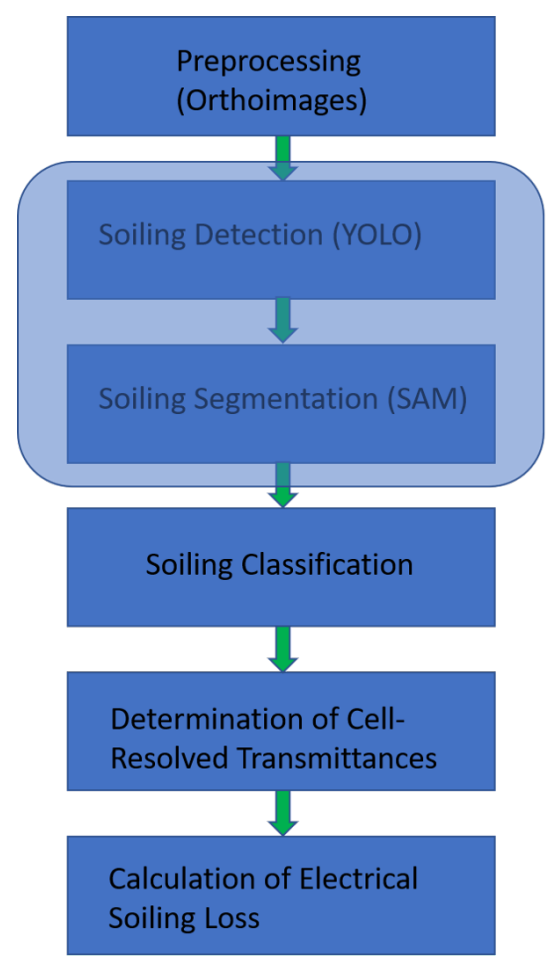


FIGURE 5.1: Flow chart illustrating the work flow of the proposed method. The two steps in the box are performed by the method developed by (Beuter, 2023).

5.1.1 Soiling Detection and Soiling Segmentation with YOLO and SAM

The method using SAM and YOLO to detect and segment soiling on PV modules was developed with a Master thesis (Beuter, 2023) supervised by Peter Winkel within this work. The method's inputs are orthoimages. First, a YOLO instance is used to detect the soiling on the orthoimage of a PV module. This YOLO instance has been specialized (application of transfer learning) for PV modules. In particular, this instance has been trained to recognize cell in-between spaces and conductor tracks as part of the module and not as soiling. The YOLO instance first calculates a bounding box in which the soiling is located for each soiling spot detected on the module. This bounding box is then transferred to a SAM instance. The SAM instance is then responsible for segmentation. It distinguishes pixel-wise between a clean module and soiling.

Beuter has trained the model for both soiling detection and segmentation. The here presented work applies Beuter's model to new datasets. The following processing steps are developed here solely by the author of this work.

As discussed in (Beuter, 2023), the method works well for most cases. However, the method also has limitations. On the one hand, the method is limited by the training data set. Only a few different module types and soiling types were used. Here, the same modules that Beuter used for his training will be evaluated. Therefore, this limitation is not expected to be too problematic. Further limitations are caused by the resolution of the input orthoimages. In both the orthoimages used in (Beuter, 2023) and the orthoimages used here, one pixel corresponds to 6 mm. The transition between clean and soiled module surfaces can therefore only be determined with this resolution. Furthermore, the transition between homogeneous and inhomogeneous soiling is fluid. Homogeneous soiling here refers to the dust soiling type analyzed in the previous Chapter. Beuter's soiling detection should only detect inhomogeneous soiling. Dust should therefore not be detected here. The transition from homogeneous to inhomogeneous soiling is sometimes continuous and is problematic, for example, when dust is deposited on the edge or in the corner of a module. The output of Beuter's method is, on the one hand, a mask that binary classifies all pixels into clean and soiled. On the other hand, all detected soiling is labeled and numbered.

5.1.2 Classification of Different Soiling Types

A new way of distinguishing different kinds of soiling is developed. Two different kinds of soiling are used in the first tests of the developed method. Leaves and poster stickers are attached to the modules of interest. The poster stickers are simulating bird dropping and will hence be referred to as artificial bird droppings in the following. As can be seen in Figures 5.2 and 5.3 the leaves and the artificial bird dropping vary significantly in color. Therefore, it is sufficient to analyze the color of a given soiling spot to categorize it. A dynamic threshold method is introduced. In simple terms: if a detected soiling spot is bright enough it is classified as a bird dropping and if it is darker it is classified as a leave. This way of categorizing the different kinds of soiling is only used for the specific case of two categories as discussed here. In order to achieve general applicability an advanced method should be used, that also considers properties like the size, the shape, and the color distribution of the soiling spots. The average color itself might not be sufficient to distinguish multiple types of soiling.

Figures 5.2 and 5.3 show the results of detecting, segmenting, and categorizing different soiling spot. For both cases the left sub-figure shows the input orthoimage

while the right sub-figure shows the masked orthoimage. Detected leaves are shown in blue while detected bird dropping are shown in red. As one can see every soiling spot is detected. Additionally, when comparing the input orthoimage with the masked orthoimage one can see that the categorization worked for every soiling spot for the two cases shown here.



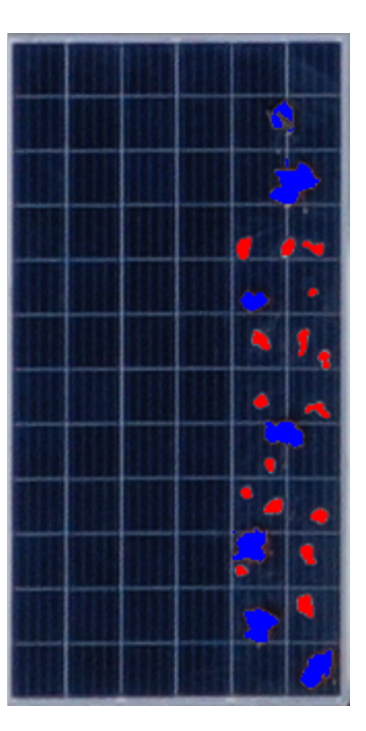


FIGURE 5.2: Left: Exemplary chosen orthoimage of module 4; Right: Masked orthoimage of the orthoimage on the left. Detected leaves are colored blue and detected stickers are colored red.

This approach was only possible because there are only two categories. If there were multiple categories, also other characteristics of the soiling spot could be used for classification purposes. In particular the size and the shape of soiling can help to distinguish different soiling types. Depending on the complexity of the images of interest one can either stick to classical computer vision methods for the categorization or one can use deep learning approaches to distinguish the different soiling types.

5.1.3 Determination of Cell-Resolved Transmittances

After classifying each detected soiling spot, a transmittance has to be assigned to each category. In general, the transmittance could be estimated from literature. However, for the experiments performed here, the transmittance of each soiling type is optically measured. For this purpose two reference cells are used. Both reference cells are cleaned. Afterwards, one reference cell remains clean while the other one is entirely covered with one of the soiling types. The ratio of GTIs of both reference cells determines the transmittance of the given soiling type.

First, the reference cells are normalized to each other. While both cells are clean the ratio of their GTIs determines their calibration factor. Figure 5.4 shows the calibration factor over the calibration time interval. Averaging over the reference interval leads to a calibration factor of 0.9989. Figure 5.5 shows the calculated transmittance of the bird droppings over time. Averaging over the chosen time interval leads to an effective transmittance of 3%. Figure 5.6 shows the calculated transmittance of the leaves over

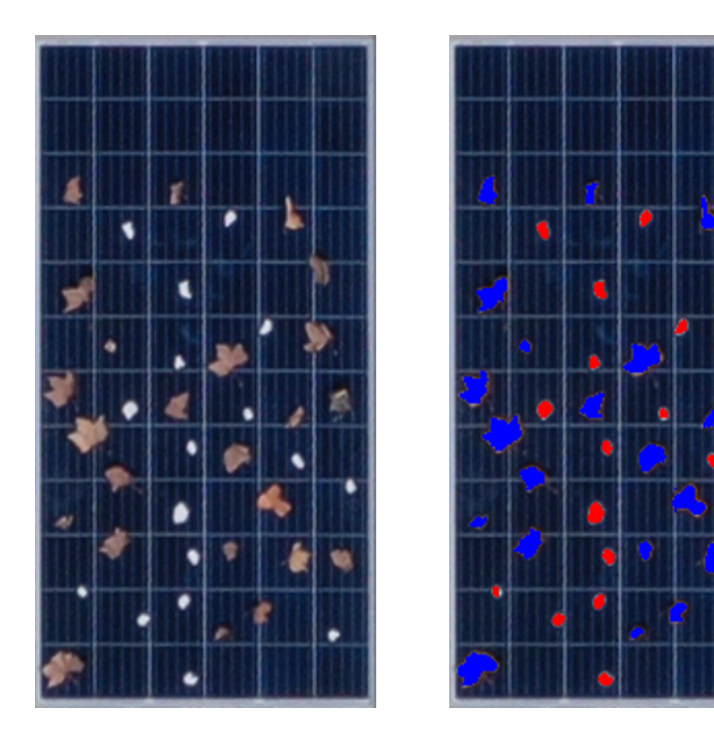


FIGURE 5.3: Left: Orthoimage of module 1; Right: Masked orthoimage of the orthoimage on the left. Detected leaves are colored blue and detected stickers are colored red.

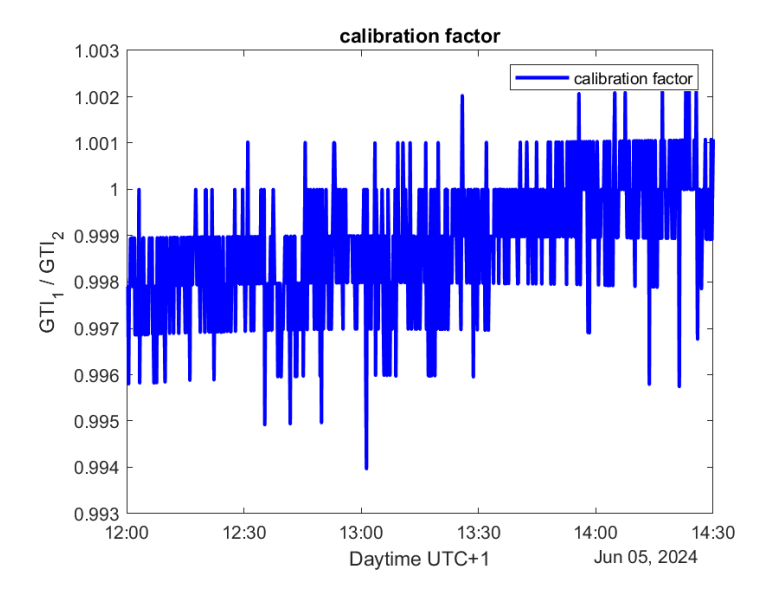


FIGURE 5.4: Calibration of the reference cells. Ratio of the GTIs of the reference cells over time. Averaging leads to a calibration factor of 0.9989. The increase of the calibration factor over time is caused by a small tilt of the reference cells towards each other.

time. Averaging over the chosen time interval leads to an effective transmittance of 15%. The slope is the graph is caused by a slight tilt of the reference cells against each other.

After determining the transmittances of each soiling type, it is now possible to determine the transmittances of each cell. Equation 5.1 shows how the transmittance T_{cell} of each cell is calculated.

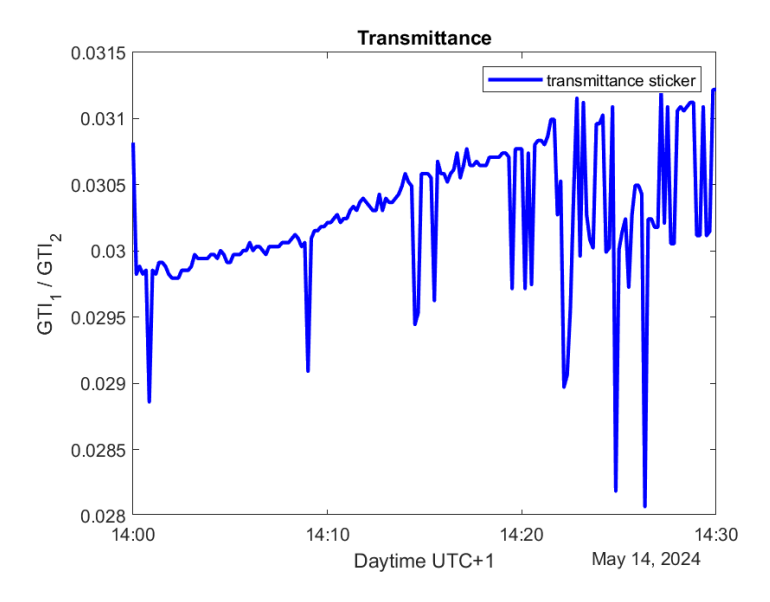


FIGURE 5.5: Transmittance of the bird droppings over time. Averaging leads to a transmittance of 3%. The calibration factor is already considered. The change over time is caused by a tilt of the reference cells towards each other.

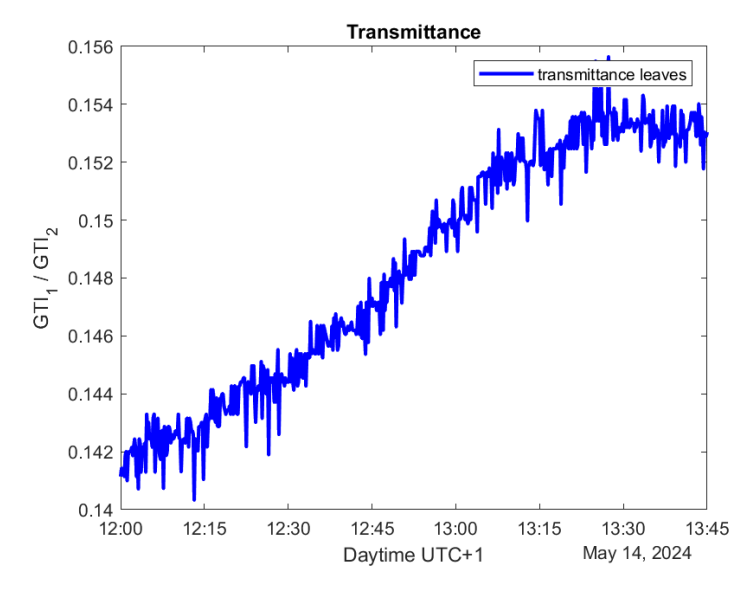


FIGURE 5.6: Transmittance of the leaves over time. Averaging leads to a transmittance of 15%. The calibration factor is already considered. The measured transmittance slightly changes over time as the reference cells are slightly tilted towards each other.

$$T_{cell} = \frac{1}{A_{cell}} \cdot \sum_{i} A_i \cdot T_{area,i} \tag{5.1}$$

The cell is divided into its individual areas A_i . These are the different soiling spots and the remaining clean area. T_{area} is the transmittance of each area. T_{area} is either one of the previously determined transmittances or 1 in case of a clean area. A_{cell} is the area of the entire cell.

 T_{cell} is calculated for every cell for a given image. These cell-resolved transmittances are averaged over all images of interest. There are always various images of a given module. In order to be considered an image has to fulfill one criterion. The viewing angle (the angle between the module normal vector and the camera vector) has to be smaller then 30°. This criterion ensures that perspective distortion is neglectable. Otherwise leaves that are not in laying in plan on the module might be considered to cover a larger area then they actually are.

5.1.4 Soiling Loss Calculation on Module Level

An electrical model (see Chapter 6) is used to calculate the soiling loss on the module level. The model considers electrical mismatch. therefore the soiling loss is generally speaking not equal to the arithmetic average of the cell-resolved transmittance losses $(1-T_{cell})$. Instead, electrical mismatch, if present, causes additional losses on module level.

The electrical model calculates the power of the module for the imaginary clean case and for the case of the calculated soiling pattern. The ratio of the calculated powers is then considered to be the soiling loss. For these calculations, the electrical model considers the module's data sheet parameters. In particular the electrical model considers the nominal power from the data sheet. At this point aging or other deviations from the manufacturer's specifications are not considered. Hence, the model does not accurately calculate the power output of the module. However, the mismatch losses are considered to be independent of the degree of aging. After a calibration measurement, the degree of aging and other deviations from the manufacturer's specifications are considered and the power output can be determined. Details of the electrical models are described in Chapter 6.

5.2 Exemplary Test of the Developed Method

The measurement was carried out on April 30th, 2024. As described above two different soiling types are used: leaves and artificial bird dropping. These soiling types are placed in two different modules. These are shown above in Figures 5.2 and 5.3. Both modules are soiled with both soiling types. For module 1 (Figure 5.3) the soiling is distributed over the entire area of the module. For module 4 (Figure 5.2) the soiling is only placed in the right sub-string to provoke electrical mismatch.

The evaluation is performed as described in section 5.1. Figure 5.7 shows the cell-resolved transmittance losses (soiling losses). One can see that the cells which are covered the most in Figure 5.2 and 5.3 show also the highest soiling losses.

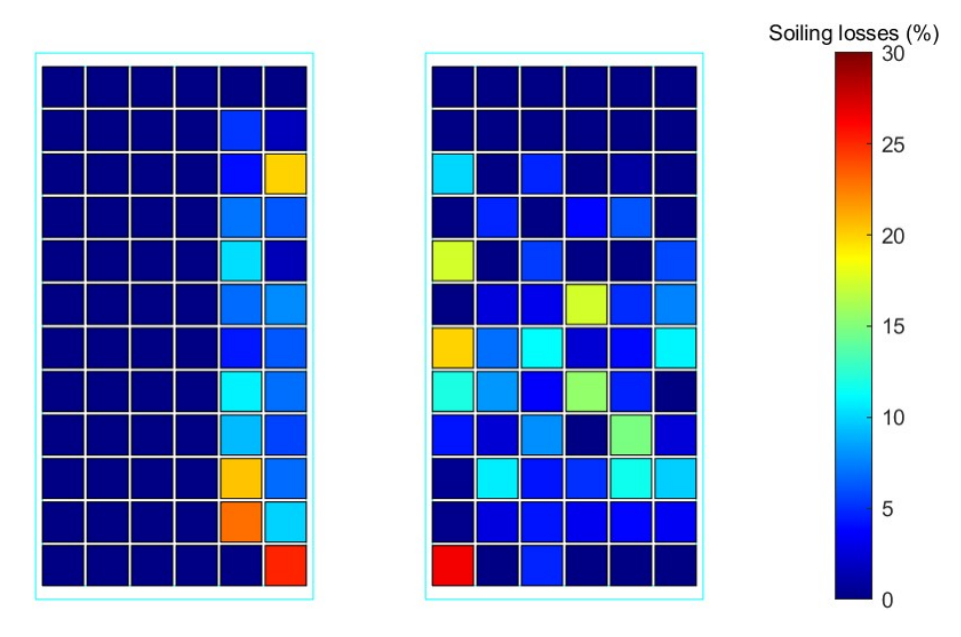


FIGURE 5.7: Cell resolved transmittances for module 1 (right) and module 4 (left). Averaged result from seven orthoimages, including the ones shown in Figures 5.2 and 5.3. In the following used to determine the electrical losses.

Figure 5.8 illustrates how much the cell-resolved transmittance varies from one image to another. As an example this Figure refers only to the right sub-string of module 4 (left in Figure 5.7). The Figure confirms that the evaluation is similar for every image. The highest standard deviation (considering the data of the seven images) of the transmittance for a cell is 2.1%. The average standard deviation is 0.4% absolute. Table 5.1 then compares the soiling loss on a module level calculated by the developed optical method with the electrical reference measurement. The electrical reference is calculated by comparing the power of modules 1 and 4 to the power of module 2 that has been cleaned beforehand. The method is described in Chapter 2 and is already used in Chapter 4. A detailed evaluation of the electrical reference measurement can be found in the Appendix A.4.

Table 5.1 shows the results of measuring the soiling loss optically. For module 1 the electrically measured soiling loss is 13.9% and the optically measured soiling loss is 14.4%. For module 4 the electrically measured soiling loss is 14.1% and the optically measured soiling loss is 14.8%. The absolute deviations are therefore 0.5% and 0.7%. These results show that the method principally works. The method should be tested under a variety of conditions.

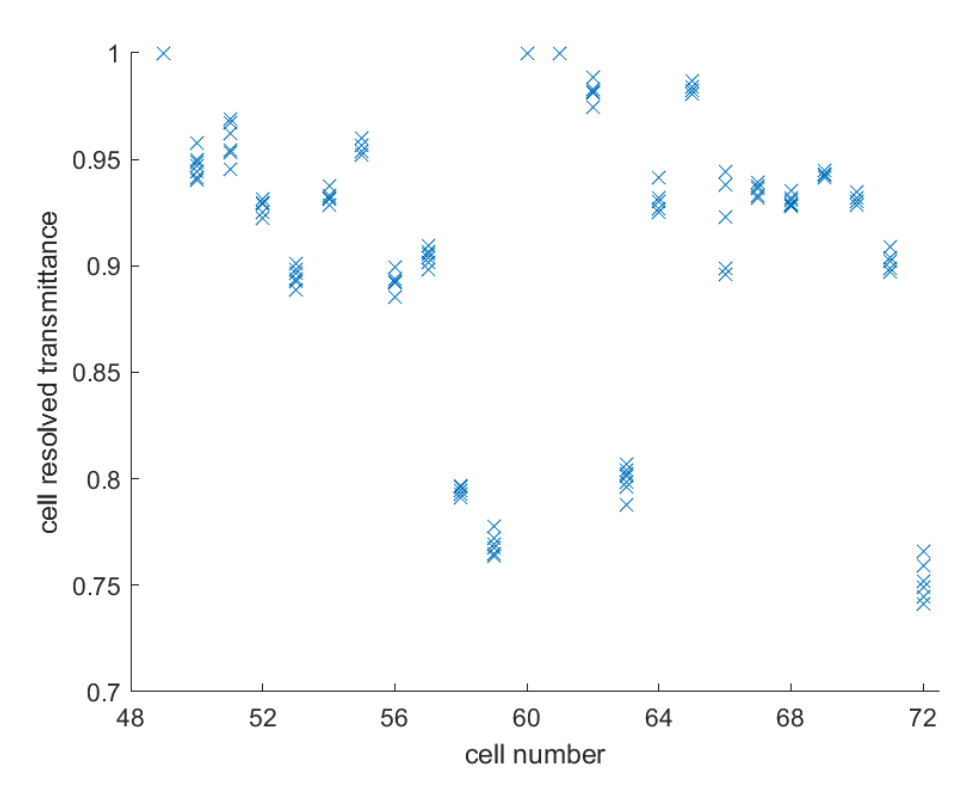


FIGURE 5.8: Scatter plot of the cell-resoled transmittances; referring to module 4 (left in Figure 5.7). Only the cells of the right sub-string are shown. Cell number starts at the upper left corner and is then counted downward. After finishing the first column, counting is continued in the second column.

TABLE 5.1: Comparing the electrically and optically measured soiling loss. The calculation of the electrical reference soiling loss is shown in Appendix A.4.

Module number	Electrical measured soiling loss	Optically measured soiling loss
1	13.9%	14.4%
4	14.1%	14.8%

5.3 Summary and Outlook

This Chapter has presented a new method for measuring inhomogeneous soiling. The method was tested for two different soiling types. Both soiling types, leaves and stickers have been detected and segmented. The stickers were chosen to simulate bird droppings. The method was tested in one campaign with two modules. For each module, seven images have been considered. For the first module, the observed absolute deviation is 0.5% and for the second module, the deviation is 0.7%. For both modules, the measured reference loss is around 14%. This shows that the method principally works.

Further tests of the method have to be performed in the future. The method should be tested for a greater variety of soiling types and modules. Not all soiling types might be detected with the same accuracy. Also, it should be noted that the transmittance might vary for different soiling spots of the same soiling type, e.g. not every leave looks the same and has the same transmittance. Furthermore, it is not yet clear how the method performs when literature values for the transmittance are considered.

A test of the method on a large scale in a PV plant with operating conditions would be beneficial to address the above-mentioned considerations and to get statistical evidence. One should also keep in mind that so far only artificial soiling has been considered.

Chapter 6

Electrothermal Modeling of Soiled PV Modules

IR measurements are already common practice to identify malfunctioning modules within a PV plant. The affected modules heat up and can in most cases be identified. However, the origin of such a hotspot (see definition in Section 2.5.2) is not immediately clear. A hotspot might either be caused by a cell being defective or being heavily soiled. This Chapter presents a new electrothermal model that helps to distinguish both cases. Additionally, is capable of predicting a module's temperature for the case that the module is clean and for the case that a hotspot is present. The electrical power can be estimated while considering electrical mismatch. Consequently, it can be stated which soiling pattern leads to a hotspot and which doesn't. The method is designed to be an extension of the methods developed in Chapters 4 and 5. The output (the soiling pattern) that is calculated by these methods can be used as an input for the method developed here. Parts of this Chapter have already been published by the author in (Winkel et al., 2024b).

Figure 6.1, left shows a module that visually is not soiled. No malfunction would be expected at first glance. The right side of the Figure shows the corresponding IR image of the same module. Four cells are identified which are heating up. Since there is no soiling present, the heating is caused by the cells being defective. Figure 6.2 shows an electroluminescence (EL) image of the same module. The image confirms that the module is indeed defective. Figure 6.3, left shows a module that is artificially soiled (shaded). The right side of the Figure shows the corresponding IR image. The affected cell is heating up. The artificial soiling hence therefore sufficient to cause a hotspot.

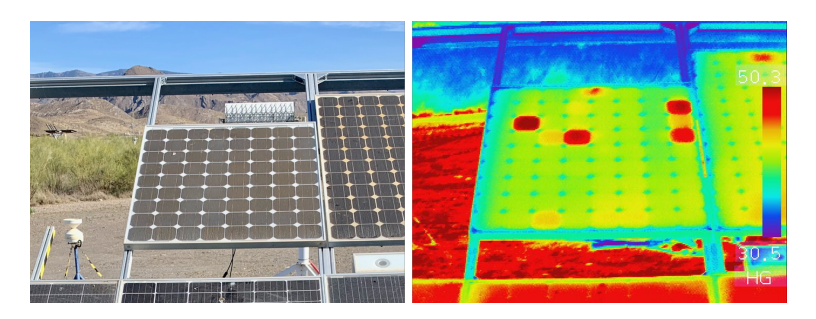


FIGURE 6.1: Left: RGB image of a defective module. On the RGB image it appears clean and a potential hotspot is not observed. Right: IR image of the defective module. The IR image clearly shows 4 hot cells. By having access to both the RGB and the IR image one can conclude that the module is defective. One string, the third and fourth column from the right, is bypassed. The temperature is slightly increased compared to the other cells (except of the hotspots).

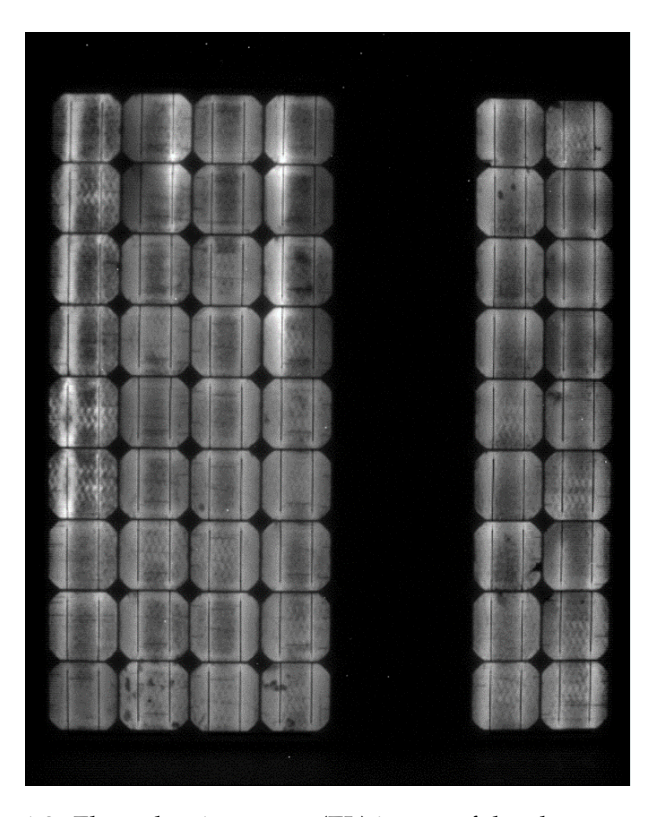


FIGURE 6.2: Electroluminescence (EL) image of the above-mentioned module (see Figure 6.1). There are multiple cracks visible. This module is likely to show one or more hot cells when operated. One string is bypassed and therefore shows no electroluminescence signal. This EL image has been provided by CIEMAT (Centro de Investigaciones Energéticas, Medioambientales y Tecnológicas).

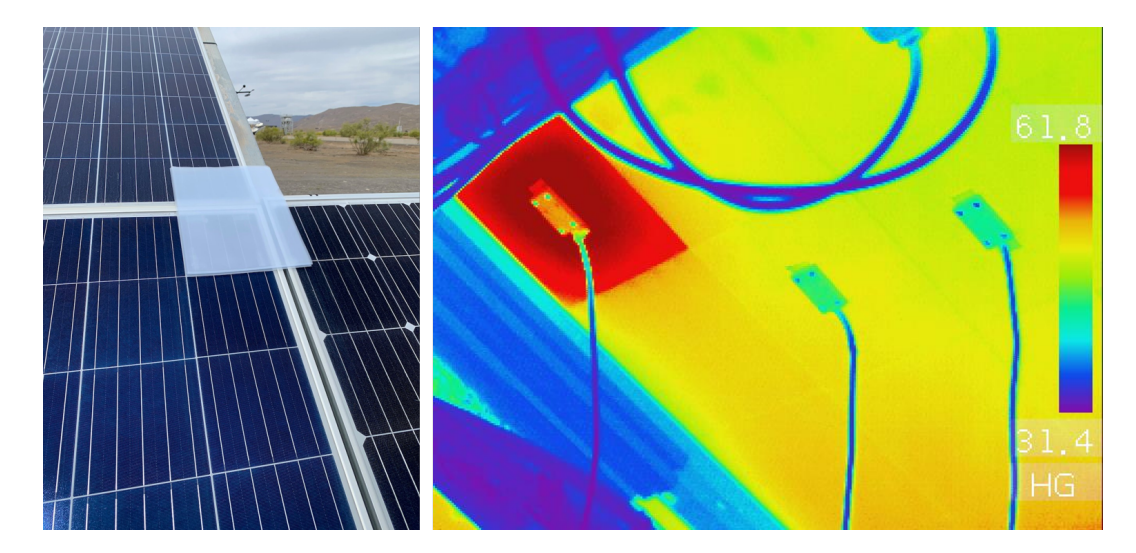


FIGURE 6.3: Left: RGB image of the artificially shaded/soiled cell. Right: IR image of the rear side of the PV module seen in the RGB image on the left. The artificially shaded cell shows a significant temperature increase (hotspot).

6.1 Electrical Model

Section 2.4 has already presented the Bishop model (Bishop, 1988) that is used to model the electrical properties of the PV modules.

The Bishop model parameters, which are mainly the single-diode parameters, are not immediately known. The methods by (Restrepo-Cuestas et al., 2022; Restrepo-Cuestas and Montano, 2024) are used to determine these parameters. As an input, these methods only require the PV module data sheet parameters. Due to aging and other e.g. production effects, the actual module parameters might differ from the data sheet parameters. To achieve greater accuracy, IV-curves of the module are recorded. The data sheet parameters are adjusted according to the confirmation measurement and are stated in Table 6.1.

TABLE 6.1: Summary of the simulation parameters. Breakdown parameters taken from (Restrepo-Cuestas and Montano, 2024; Jessen et al., 2018). The parameters are corrected for e.g. aging.

Parameter	Value
Breakdown factor	0.002
Breakdown voltage	$-14\mathrm{V}$
Trigger voltage of the bypass diode	$-0.5\mathrm{V}$
Breakdown exponential factor	3
Efficiency	17.622%
Short circuit current under STC	9.61 A
Open circuit voltage under STC	47.13 V
Power under STC	349 W
MPP current under STC	9.26 A
MPP voltage under STC	37.80 V
Temperature coefficient of the power	-0.37%/K

6.2 Thermal Model

The thermal model developed in this work is illustrated in Figure 6.5. It has a structure of four layers and six temperature nodes. The four layers are the soiling layer, the front glass cover, the silicon layer, and the back-plate. The temperature nodes are T_a , the temperature of the upper side of the soiling layer T_s , the temperature of the upper side of the glass layer T_g , the silicon temperature T_c (subscript c referring to cell), the temperature of the lower side of the back-plate T_b , and the ground temperature T_f (subscript f for floor). Note that the silicon layer is considered to be much thinner than the other layers. Roughly, the silicon layer should be around 300 µm (Tool et al., 2002). By making this assumption one can assume that there is only one cell temperature and the cell has no thermal resistance. Note also that the description of a PV cell as a stack of three layers (glass, silicon, and backplate) is generally a big simplification. The goal is to develop an easily usable thermal model. The goal is not to predict the temperature with a sub-digit precision. E.g. the anti-reflection coating of the cell is considered to be part of the glass layer and is not mentioned individually. Furthermore, the back reflector is neglected because of its thickness of around 20 µm (Lorenz et al., 2017). Thin passivation layers are also not considered here.

Note furthermore that out of the six above-mentioned temperatures, the ambient temperature and the ground temperature are inputs while the other four are outputs of the model. T_a is measured with a CS215-L thermometer. T_f has been estimated to be 10 K colder than the ambient temperature. This assumption is connected with uncertainties. However, it has been confirmed that the resulting variations in $\Phi_{th,f}$, if T_f had a 10 K uncertainty, are one order of magnitude smaller than the convective heat transfer on the rear side for the case of non-hotspot and two orders of magnitude smaller for the case of a hotspot. In the future, the simplest would be to measure the floor temperature. There are also various approaches to modeling the ground temperature (Zheng, Hunt Jr, and Running, 1993; Xu et al., 2020; Araghi et al., 2017). However, for the intended purposes, they are less suitable as they are quite complex by themselves and generally require many inputs. Furthermore, the floor temperature is not going to be spatially homogeneous as the ground experiences a shading pattern that changes over time. Additionally, the ground and the module's rear side are not parallel to each other. Therefore, the rear side in reality does not receive the entire thermal radiation emitted by the ground. Instead, it should receive a weighted average of the $\Phi_{th,f}$ and $\Phi_{th,sky}$.

Energy fluxes in between the four layers and the surrounding can be divided into five categories: GTI G, thermal radiation Φ_{th} , thermal conduction \dot{q}_{cond} , convection \dot{q}_{conv} , and generated surface power density p_c . The surface power density p_c is defined as the electrical power P_c generated by the PV cell, divided by the cell area A. The GTI is measured by a reference cell, in the wavelength range from 400 nm to 1150 nm. According to the manufacturer, the relative deviations against class pyranometers are up to 5%. The thermal radiation $\Phi_{th,sky}$ of the sky is measured by a pyrgeometer (see Table 6.2). The pyrgeometer roughly starts to measure at 4 µm until 100 µm. The thermal radiation of the sky could also be estimated with a weather model in case there is no pyrgeometer available. The other fluxes are not measured and they are only intermediate results for the model.

The thermal radiation emitted by the soiling layer is denoted as $\Phi_{th,s}$. $\Phi_{th,f}$ is the thermal radiation emitted by the floor and $\Phi_{th,b}$ is the thermal radiation emitted by the back sheet. $G_{s,\tau}$ is the part of G that is transmitted through the soiling layer. $G_{s,\rho}$ is the part of G that is reflected at the soiling layer or, in other words, scattered back to the air above the soiling layer. As for the soiling layer reflection and transmission can

TABLE 6.2: Overview of the origin of the known parameters for the thermal model. [1]: (Zhou et al., 2015), [2]: (Pfreundt et al., 2019), [3]: (Hoang et al., 2014), [4]: (Priyadarshini and Sharma, 2016), [5]: (Notton et al., 2005), [6]: (Lee et al., 2008), [7]: (Wolf, Pohl, and Brendel, 2005), [8]: (*Module data sheet* 2024), [9]: (National Oceanic and Atmospheric Administration, 1976).

Quantity	Symbol	Unit	Source
Ground temperature	T_f	°C	Estimated from ambient
	•		temperature
Surface power density	p_c	W/m^2	Electrical model
Absorptance	α	-	[1, 2, 3, 4]
Reflectance	ρ	-	[1, 2, 3, 4]
Transmittance	au	-	[1, 2, 3, 4]
Emissivity	ϵ_{body}	-	[1, 2, 3, 4]
Thermal conductivity	λ_{th} .	${ m W}{ m m}^{-1}{ m K}^{-1}$	[1, 2, 5, 6, 7]
Layer thickness	d	mm	PV data sheet [8]
Cell area	A_{cell}	m^2	PV data sheet [8]
Elevation	Н	m	Google Maps
Atmospheric density	$ ho_{air}$	${\rm kg}{\rm m}^{-3}$	[9]
Kinematic viscosity of air	ν	${ m m}^2{ m s}^{-1}$	[9]
Thermal conductivity of air	λ_{air}	${ m W}{ m m}^{-1}{ m K}^{-1}$	[9]
Specific heat capacity of air	c_p	$\rm Jkg^{-1}K^{-1}$	[9]
Characteristic length, mod-	Ĺ	m	PV data sheet [8]
ule height			

take place at each interface between the layers. $G_{g,\tau}$ is the part of G that is transmitted through the glass layer. $G_{g,\rho}$ is the part of G that is reflected at the interface between the soiling layer and the glass layer. Reflections of second order are neglected here. For example, $G_{g,\rho}$ can be reflected again at the interface between glass and soiling, but for simplicity, this term is neglected. $G_{f,\rho}$ is the part of the GTI that reaches the back sheet of the module. Attenuations occur because the module itself is shading the ground. A part of the light that reaches the ground is reflected, both directly and diffusely. Finally, only a fraction of the reflected light reaches the module's rear side. The ground albedo and the view factor have to be considered for $G_{f,\rho}$. The view factor describes the fraction of the light reflected by the unshaded that reaches the module's back sheet. $G_{b,\tau}$ is the part of $G_{f,\rho}$ that is transmitted through the back sheet and $G_{b,\rho}$ is the part that is reflected there.

 $\dot{q}_{cond,gs}$ is the conductive heat transfer through the soiling layer. $\dot{q}_{cond,cg}$ is the conductive heat transfer through the glass layer. $\dot{q}_{cond,cb}$ is the conductive heat transfer through the back sheet. All conductive heat transfers point away from the cell. This is defined this way because the cell is the layer that absorbs the most radiation and is therefore the hottest. $\dot{q}_{conv,s}$ is the convection that takes place on the soiled surface. $\dot{q}_{conv,b}$ is the convection that takes place on the module.

 p_c is the power density generated by the cell, which describes the electric power exiting the cell (positive sign) or the received electric power converted to heat (negative sign). All quantities are defined in such a way that they are positive for common operating conditions without a hotspot.

Assuming steady-state temperatures and considering each layer by itself, input

and output fluxes can be equated in the form of balance equations. The balance equations for each layer are shown in Equations 6.7, 6.8, and 6.9. The order of the equations is the same as the one of the layers shown in Figure 6.5.

$$\Phi_{th,body} = \epsilon_{body} \cdot \sigma \cdot T_{body}^4 \tag{6.1}$$

$$\dot{q}_{cond,hot,cold} = \lambda_{th} \cdot \frac{T_{hot} - T_{cold}}{d}$$
 (6.2)

$$\dot{q}_{conv,body} = h(v_w) \cdot (T_{body} - T_a) \tag{6.3}$$

Equations 6.1, 6.2, and 6.3 describe how the thermal radiation, the thermal conduction, and the convection depend on the temperature, respectively. For thermal radiation, the key parameters are the body's emissivity ϵ_{body} , the Stefan-Boltzmann constant σ , and the body's surface temperature T_{body} . The thermal conduction depends on the thermal conductivity λ_{th} , the temperatures of hot and cold sides T_{hot} and T_{cold} , and the corresponding thickness d. Convection depends on the temperature difference between the surface and the ambient temperature $(T_{body} - T_a)$ and the convective heat transfer coefficient h which depends on the wind speed v_w itself.

Both free and forced convection are considered. The heat transfer coefficients are combined as the square root of the quadratic sum (Siebers, 1983). In some cases, also larger exponents instead of two might be used. Notton et al. discuss a few different forced and free convection models for PV modules (Notton et al., 2005). The free convection model by (Kreith and Kreider, 1978) and the forced convection by (Cole and Sturrock, 1977) are used. See therefore Equation 6.4 and Equation 6.5. Equation 6.6 shows how free and forced convection are combined. Roughly speaking, for wind speeds above 3 m/s the forced convection dominates. Vice versa for wind speeds below 1 m/s the free convection can be interpreted as a lower limit.

$$h_{forced} = 11.4 \frac{W}{m^2} + 5.7 \frac{W \cdot s}{m^3} \cdot v_w \tag{6.4}$$

$$h_{free} = 1.42 \cdot \left(\frac{(T_m - (T_a) \cdot \sin(\beta))}{L}\right)^{0.25}$$
(6.5)

$$h = \sqrt{h_{forced}^2 + h_{free}^2} \tag{6.6}$$

L is the characteristic length of the module, which in this case is the module height. β is the inclination of the module. T_m and T_a are the module temperature and the ambient temperature like in the literature models discussed above.

The air parameters are derived from the US Standard Atmosphere (National Oceanic and Atmospheric Administration, 1976). Some parameters are estimated involving certain assumptions. E.g. it is assumed that there is no transmission through the cell, meaning UV and IR radiation passing through the semiconductor layer is neglected. The error due to this assumption should be of the same order of magnitude that the neglect of multiple reflections has. For the convection, some parameters are also determined using the python library fluids (Bell, 2023), which contains functions of the US Standard Atmosphere (National Oceanic and Atmospheric Administration, 1976). Other parameters are derived from the data sheet of the PV module (*Module data sheet* 2024). The physical properties of each layer will be discussed in the next section 6.2.1.

6.2. Thermal Model 69

6.2.1 Material Properties of Layers

A set of material properties is selected based on the literature and the module data sheet. This set includes optical properties such as reflectance, transmittance, and emissivity. The parameter set also includes the thermal conductivity. In addition, the layer thickness is stated. All parameters are illustrated in Table 6.3. If there are multiple values for one parameter, the one emphasized in bold was finally implemented in the thermal model. The * symbol indicates that the value is an assumption with justification in the caption of the table. The emissivity of silicon is not stated here because thermal radiation only takes place at surfaces, i.e. at the interfaces with air. In the model, the silicon layer is therefore not emitting thermal radiation. The thermal conductivity of silicon is not stated because the silicon layer is assumed to be thin against the glass and back-plate layers. The absorptance of each layer is not stated here as it can be calculated simply, as the sum of reflectance, transmittance, and absorptance has to be one. The transmittance through the semiconductor layer itself is neglected. Literature states that the fraction of the light that is transmitted through the silicon layer is in the low single-digit percent range. Additionally, most parts of this light are then reflected at the back reflector which has not been included in the model. Note also, that the thickness of a dust layer will be different in each situation. 10 µm is a reasonable dust particle diameter (Ilse et al., 2019; Ilse et al., 2018). Since there is no significant thermal resistance in such a thin layer, this thickness can be neglected. The dust surface temperatures and the module surface are basically the same.

TABLE 6.3: This table summarizes the most important properties of the four module layers. [1]: (Devi and Satheesh, 2021), [2]: (Devi and Satheesh, 2022), [3]: (Rubio, Caselles, and Badenas, 1997), [4]: (Hamdhan and Clarke, 2010), [5]: (Toolbox, 2003), [6]: (Toolbox, 2011), [7]: (Zhou et al., 2015), [8]: (Priyadarshini and Sharma, 2016), [9]: (Pfreundt et al., 2019)

	$\rho[-]$	$\tau[-]$	$\epsilon_{body}[-]$	$\lambda_{th}[Wm^{-1}K^{-1}]$	d[mm]
Dust layer	$(1 - \tau)$ ·	Optically	0.903 [3]	0.27 [4]	0.01 *
	0.95 [1, 2]	measured			
Foil stack	Optically	Optically	0.92 [5]	0.2 [6]	Measured
	measured	measured			
Glass	0.08 [7, 8]	0.92 [7, 8]	0.837 [9]	1.0 [9]	3.0 [9]
Silicon	0.08 [7]	0*	-	-	-
Back sheet	0.86 [7]	0.2 [7]	0.769 [9]	0.155 [9]	0.35 [9]

For the ground, n emissivity of 0.947 is assumed (Rubio, Caselles, and Badenas, 1997). The albedo of the ground is 0.189 (Sutha et al., 2017). It is assumed that 5% of the incident light will be reflected and reaches the rear side of the module. This can only be estimated as parts of the ground are shaded by the module itself. Also, not the entire part that is reflected at the ground goes in the direction of the module. The larger part goes towards the rest of the hemisphere.

The soiling layer's parameters have been estimated as follows. The most important property is the transmittance as it determines whether the cell generates or dissipates energy. For dust-like soiling, one can assume that reflection and scattering dominate over absorption (Ilse et al., 2019). For other soiling types, considerations have to be made individually. In the experiments, a stack of foils is used which should

also have a very low absorptance. For the experiments presented in section 6.3.2, the transmittance of the foils has been measured optically with a Perkin Elmer Lambda 1050 spectrophotometer (discussed below). In the future, the transmittance model developed by (Winkel et al., 2024a) can determine the transmittance of dust using RGB images of the affected modules. In terms of the emissivity, there is literature for both, the plastic foils used here and for mineral dust which is a future application. Ground reflectance, i.e. the albedo, is also a prerequisite for the precise determination of the energy balance (Enriquez et al., 2012). The ground emissivity varies depending on the ground type. For instance, the bare soil calcaric regosol shows an emissivity of 0.947, whereas green-colored short grass has a higher emissivity of 0.976, and dry grassland reaches a value as high as 0.99 (Rubio, Caselles, and Badenas, 1997). Finding an accurate value that suits the test bench is less important because only a fraction of the radiation reflected on the ground will be reflected toward the module's rear side. A large portion of the reflected radiation leaves in the direction of the sky. It is only possible to roughly estimate this fraction. The equations above assume that the ground experiences the entire GTI. While in reality parts of the ground are shaded by the module itself. The uncertainty of this factor how much ground reflected irradiance hits the module's rear side is much larger than the uncertainty of the reflectance property itself or different ground types. Also, this factor is going to change over time.

6.2.2 Combination of Electrical and Thermal Model

The electrical model initially guesses the module temperature to be equal to the NOCT temperature (according to the data sheet) and calculates the cell power P_c . This power estimate is then divided by the cell area, giving the surface power density p_c for the cell. The thermal model receives the surface power density as one of the parameters to predict the cell temperature T_c . These better estimates of the cell temperatures are then fed back into the electrical model, as it might differ from the originally estimated temperature. In the tested datasets used in this work, both power and temperature predictions converge after three iterations. The power changes afterwards by less than 0.01 W per iteration and the temperature by less than 0.01 K. Figure 6.4 illustrates the interconnection of the electrical and the thermal model.

The electrical model is based on the single-diode model. The single-diode parameters are estimated according to the data sheet. (Bishop, 1988) provides a tool that enables the extraction of the single-diode parameters from the data sheet parameters. Additionally, a potential efficiency reduction due to aging and module-specific production-related deviations from the design efficiency are considered. The data sheet's power and efficiency are adjusted such that the model results match the measurements for the power, voltage, and current for a calibration interval. The temperature effect on the model parameters was considered as given in the data sheet to obtain the expected power under STC. The module is considered to be a serial connection of three sub-strings of 24 cells each. There is a bypass diode in parallel to each sub-string. The model allows assigning every cell its individual properties. In particular, every cell has its soiling transmittance. IV curves are calculated on cell, string, and module levels. Correspondingly, electrical mismatch losses are considered. The same current must flow through all cells unless the bypass diodes are active. The most affected cell limits the total current. If the total current is greater than the I_{SC} of the most affected cell, this cell dissipates energy. Also, the temperature of each cell is considered as input data. This cell-resolved temperature is used as an iterative input of the electrical and thermal model. The electrical model's implementation is based

6.2. Thermal Model 71

on the Python package *pvlib* (Holmgren, Hansen, and Mikofski, 2018; Holmgren et al., 2015). It uses a model developed by Bishop et al. (Bishop, 1988).

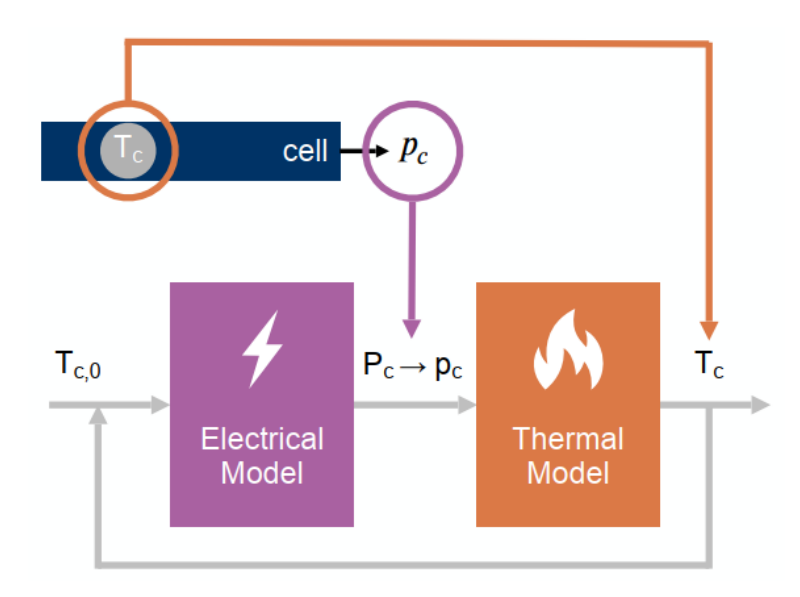


FIGURE 6.4: Sketch describing the linkage between the electrical and the thermal model combining it to the electrothermal model. The cell temperature is iteratively fed into both models. Both, the electrical and the thermal model require an initial estimate of the temperature and then refine the temperature in an iterative way. The model stops after three iterations each as the temperature and the power do not change noticeably afterwards.

$$G + \Phi_{th,sky} = G_{s,\tau} + G_{s,\rho} + \Phi_{th,s} + \dot{q}_{conv,s}$$
 (6.7)

$$G_{s,\tau} + \dot{q}_{cond,gs} + \dot{q}_{cond,cg} = G_{g,\tau} + G_{g,\rho}$$

$$\tag{6.8}$$

$$G_{b,\tau} + G_{g,\tau} = G_{c,\rho} + p_c + \dot{q}_{cond,cg} + \dot{q}_{cond,cb}$$

$$\tag{6.9}$$

$$G_{f,\rho} + \Phi_{th,f} + \dot{q}_{cond,cb} = G_{b,\tau} + G_{b,\rho} + \Phi_{th,b} + \dot{q}_{conv,b}$$
 (6.10)

6.2.3 Non-Linear Set of Equations

Equation 6.7, Equation 6.8, Equation 6.9, and Equation 6.10 build a set of four equations with four unknown quantities. There are four unknown temperatures T_s , T_g , T_c , and T_b . All other parameters are known (or estimated) as described in Table 6.2 and Table 6.3 above. Some of the temperatures occur in the fourth power. This makes the system non-linear and not analytically solvable. However, this system can be solved numerically. The *fsolve* function of the *scipy* package (The SciPy community, 2024) is used.

6.2.4 Thermal Inertia

As described above, the model solves a set of non-linear Equations for the steadystate. In reality, the cell temperature does not instantly respond to a change of input parameters, e.g. a change in incoming radiation. The thermal inertia of the module is not considered when applying the steady-state assumption. To roughly consider the thermal inertia a rolling average is applied. Averaging is performed over ten temperature values modeled with the above described model and the average is assigned to the last of the corresponding timestamps of the final time series. The time interval is chosen as a simple best-by-test approach. In the following, the rolling average is applied to the developed model as well as to the models from the literature.

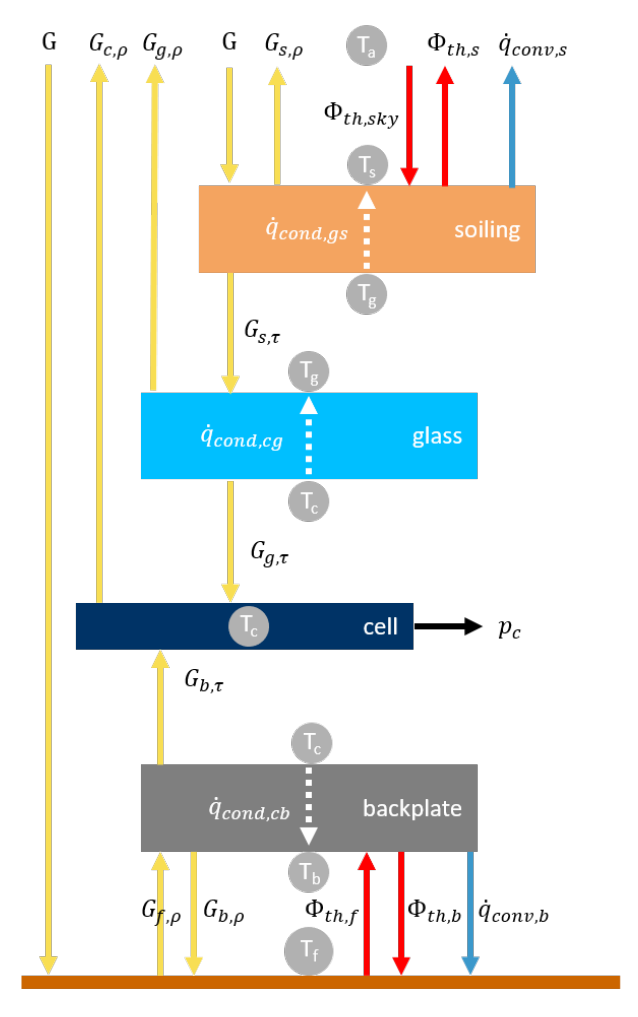


FIGURE 6.5: Sketch of the model structure. Shown are the four different layers of the model and the temperature nodes. Additionally, all energy fluxes are illustrated.

6.3. Results 73

6.3 Results

In this section the experiments performed to validate the developed model are discussed. These are on the one hand experiments with a clean module (see Section 6.3.1) and experiments with a partially soiled module (see Section 6.3.2).

6.3.1 Experiments with Clean Modules

The performance of the electrothermal model under clean conditions was analyzed within six consecutive days, from April 26th until May 1st, 2023. In particular, the performance for module temperature determination was compared to measurements and the state-of-the-art models described in Chapter 2. The temperature was measured with a Pt-1000 sensor (uncertainty class B) which was mounted on the module's rear side with an adhesive thermo-film (see Chapter 3). The module of interest is manufactured by JA Solar and has a nominal power of 390 W (*Module data sheet* 2024). Details can be found in the data sheet (*Module data sheet* 2024).

Figure 6.6 compares the modeled temperature to the measured one over the above-mentioned periods. In general, the model works well and is capable of giving a good estimation of the module temperature. For some intervals, a negative bias is found (e.g. Apr. 26, 15:00-16:00) while the model overestimates the temperature for other time intervals (e.g. May 1st, 14:30-16:00). Reasons for this and possible solutions are assumed to be mostly related to the convection model. For example, currently, only the wind speed is considered, but not the wind direction. Also, the convection should in theory depend on the position of a given cell within the given module. The effects of the convection modeling will be discussed further related to the experiment with soiled modules (section 6.3.2). Further potential enhancements could be a better consideration of thermal inertia which plays a particular role when the GTI or the wind speed suddenly changes.

The obtained error metrics over the six days, 10:00 to 16:00 each, are an RMSE of 2.6 K, an MAE of 2.2 K, and an MBE of -1.3 K.

Figure 6.6 (right) shows the results of the developed model and the four above-mentioned thermal models from the literature for two exemplary days. On the left, the Figure shows the two most important meteorological parameters impacting the module temperature, namely the GTI and the wind speed. The other four days are visualized and discussed in Appendix C.

TABLE 6.4: Summary of the error metrics for the different thermal models, both from literature and the developed model. This table refers to the clean state. The data refers to the entire test period consisting of six days.

Model	RMSE (K)	MAE (K)	MBE (K)
Ross	9.4	8.7	8.6
Sandia	4.0	3.6	3.4
Faiman	2.7	1.9	0.5
NOCT	2.9	2.1	0.2
Developed model	2.6	2.2	-1.3

Table 6.4 summarizes the error metrics of all thermal models. The developed model performs similarly to the two best models from literature, the Faiman model

and the NOCT model. The developed model has the lowest RMSE, with a value of 2.6 K, which is marginally better than the next best Faiman model while the MAE is insignificantly higher, with a value of 2.2 K. The absolute value of the MBE of the developed model is 1.3 K and hence higher than the one of the NOCT model with a value of only 0.2 K. The temperature deviation has an impact on the module's efficiency. Typically, the efficiency drops by 0.4% for a temperature increase of 1 K. The impact of temperature deviation on the yield is not the decisive factor for the objective as the model is designed for hotspot analysis. Quick hotspot identification and hotspot temperature estimation are possible with the new model and are discussed in the next Section.

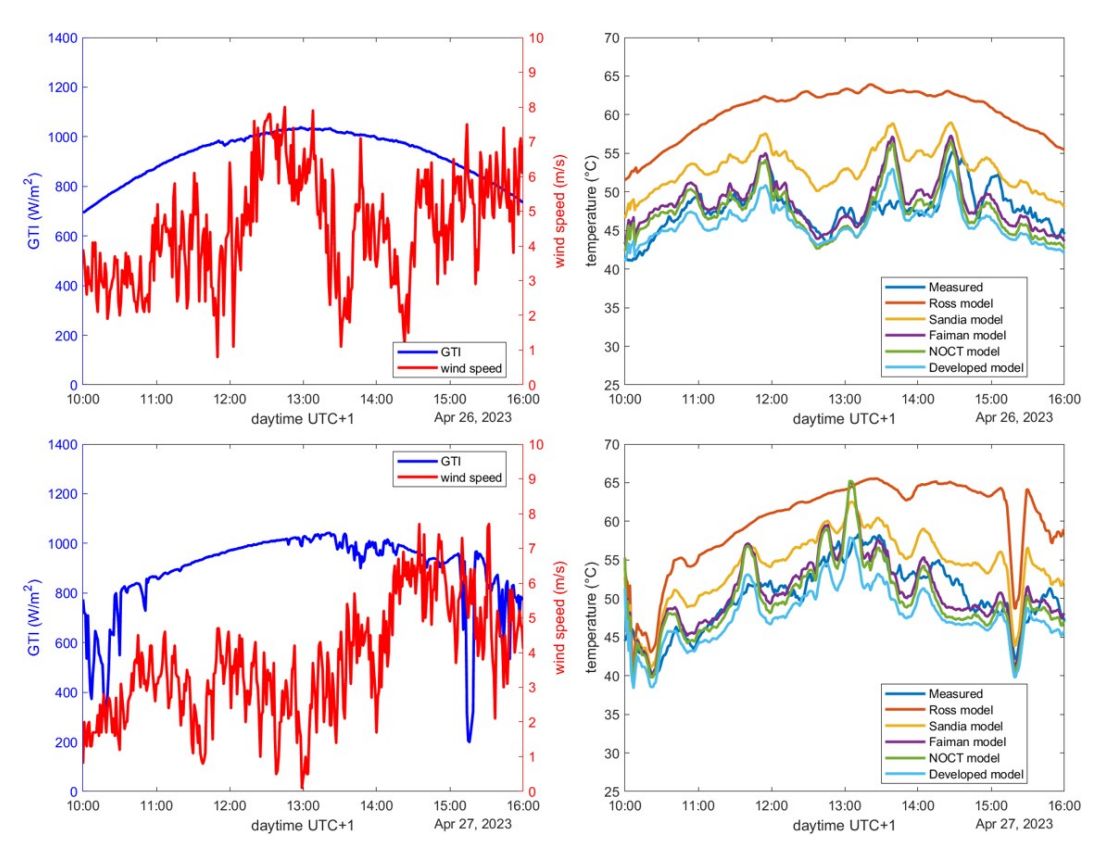


FIGURE 6.6: Comparison of the developed model with the measured temperature and the thermal models from literature discussed in Chapter 2 for the 26^{th} and the 27^{th} of April 2023.

6.3. Results 75

6.3.2 Experiments with Soiled Modules

For this experiment, one cell of the module is entirely covered with an artificial shading material as shown also in Figure 6.3. The material used is a stack of foils and its transmissivity is roughly constant over the visible spectrum. The effective transmittance is 44.6% as determined by optical measurements. The spectral transmittance is shown in Figure 6.7 (discussed below). The goal of the artificial soiling is to provoke a hotspot and make the soiled cell dissipate power. Therefore, the qualitative regime of the transmittance is more important than its absolute value. Additionally, the hotspot temperature and humidity can change the foils' optical properties over time. The experiment was performed from March 9th to March 14th, 2024. Figure 6.7 shows the

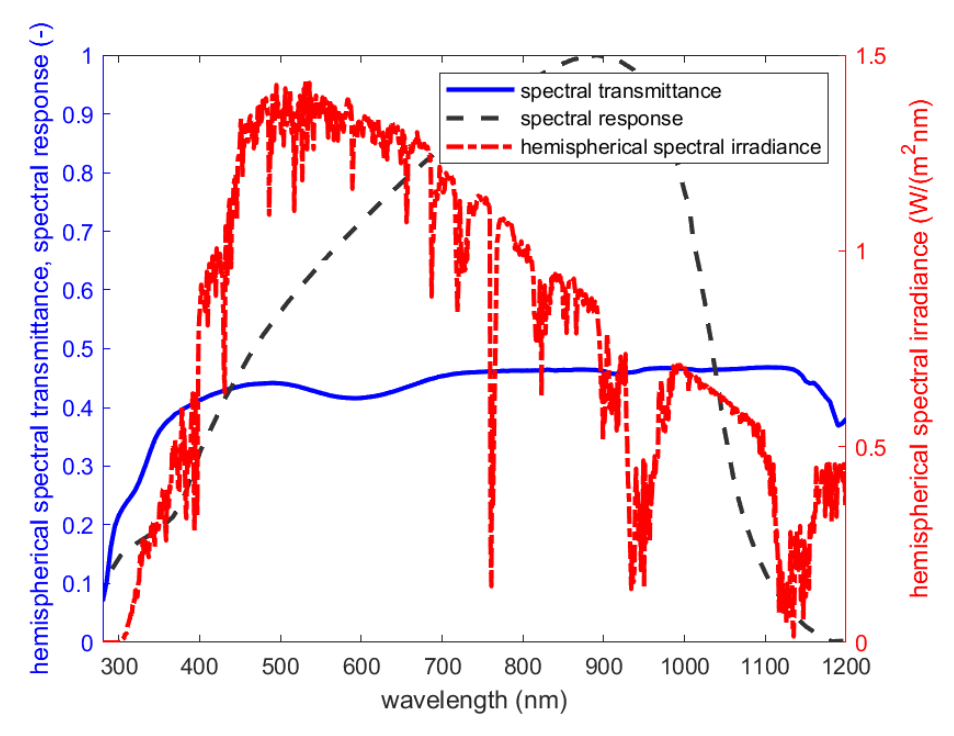


FIGURE 6.7: In blue, spectral transmittance against wavelength of the used artificial soiling. In red, solar spectrum used for averaging the spectral transmittance. In dark gray, spectral response of a mono-Si solar cell. Weighted averaging results in an effective transmittance of 44.6%.

optically measured spectral transmittance of the foils used as artificial soiling in blue. Averaging the spectral transmittance weighted by the solar spectrum shown in red (ISO9845-1 Main Spectra GTI) and the spectral response of the module shown in dark gray (Winter, Friedrich, and Sperling, 2009; Jessen et al., 2018) results in a wavelength averaged transmittance of 44.6%.

Figure 6.8 compares the measured and simulated IV curves. For example, only 4 IV curves of one day, March 12th, are shown with a time difference of 2 hours each. One can see that the shapes of the IV curves are qualitatively correct. There is a slight tendency to predict too high open circuit voltages and too low short-circuit currents. The IV-curve with the timestamp 14:00 is impacted the most. The reason is probably related to simplifications of the underlying electrical Bishop model (Bishop, 1988; Bishop, 2006). The position of the maximum power point is calculated relatively accurately. The height of the plateau of the current differs slightly between measurement and simulation. The reason might be that the transmittance of the

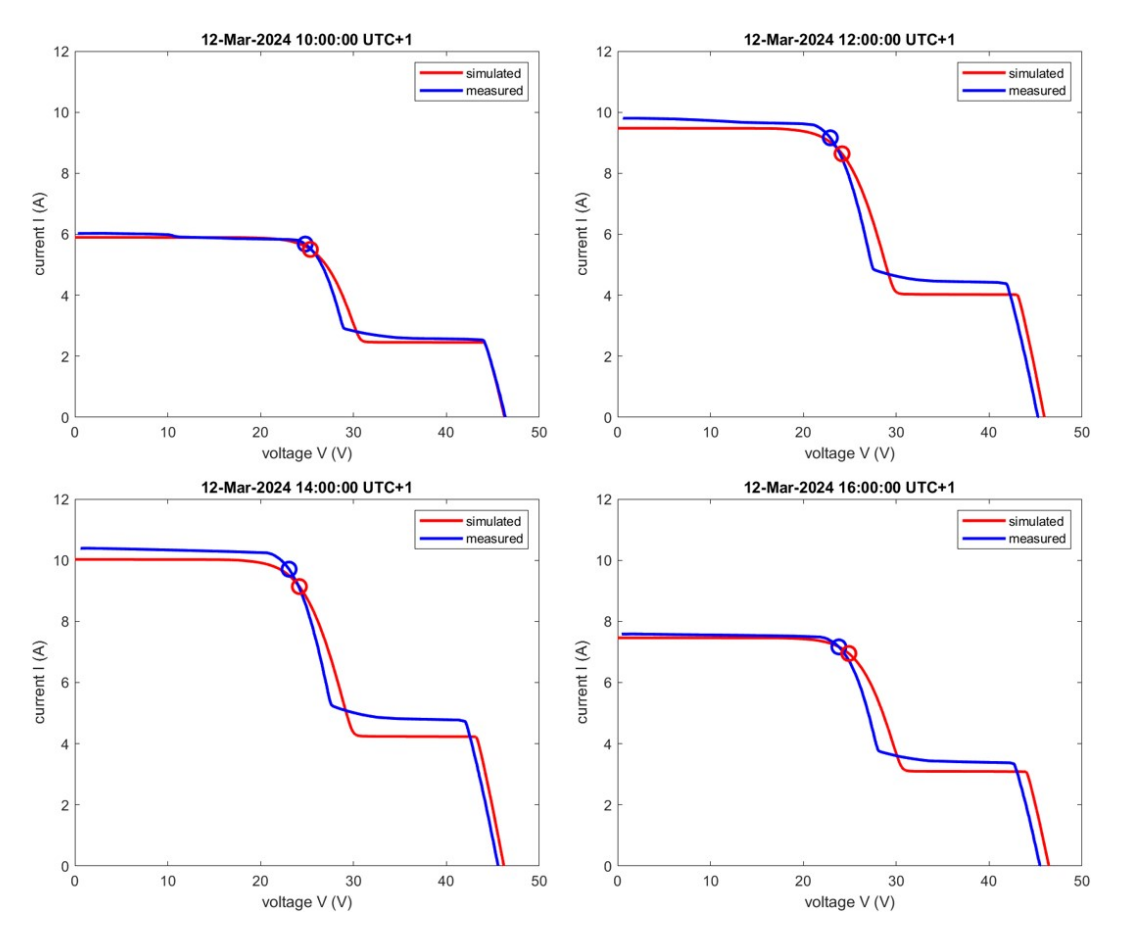


FIGURE 6.8: Measured and simulated IV curves. Exemplary, one day and 4 timestamps are chosen. 12th of March 2024. Upper left: 10:00, upper right 12:00, lower left 14:00, and lower right 16:00. The small circles indicate the maximum point points.

artificial soiling layer has slightly changed over time. As the foils used as artificial soiling heat up, they might change their transmittance. Figure 6.9 compares the measured and simulated electrical powers in a plot as a function of time. In general, the electrical power is calculated well (RMSE = $2.1 \, \text{W}$, MBE = $-0.2 \, \text{W}$, MAE = $1.6 \, \text{W}$). One sub-figure corresponds to each day, starting in the upper left with the 9^{th} of March and continuing to the 14^{th} of March in the lower right.

The right side of Figures 6.10, 6.11, and 6.12 compares the measured and simulated hotspot temperatures and the measured temperature of a clean cell. Each day is discussed individually. To explain and understand the features that occur one must have a look at the GTI, the wind speed, and the wind direction which are shown also in Figures 6.10, 6.11, and 6.12 but on the left side each. On the 9th of March, the temperature is simulated well with an RMSE of 4.8 K. This is a day with a low GTI and strong wind from the southwest direction. For the 10^{th} of March, the model predicts a hotspot with temperatures about 40 K above those of the clean cells but underestimates the temperature significantly by more than 30 K resulting in an RMSE of 32.7 K and an MBE of -30.9 K. On this day the GTI is generally pretty high and there is strong wind from the west direction. In this context a high GTI refers to the GTI reaching about $1000 \, \text{W/m}^2$ at solar noon and overall only a few clouds over the day. On the 11^{th} of March, the temperature estimation is good for the first two hours of the analyzed time interval. Afterwards, the temperature is underestimated similarly to the 10^{th} of March resulting in an RMSE of 21 K and an MBE of -16.7 K.

6.3. Results 77

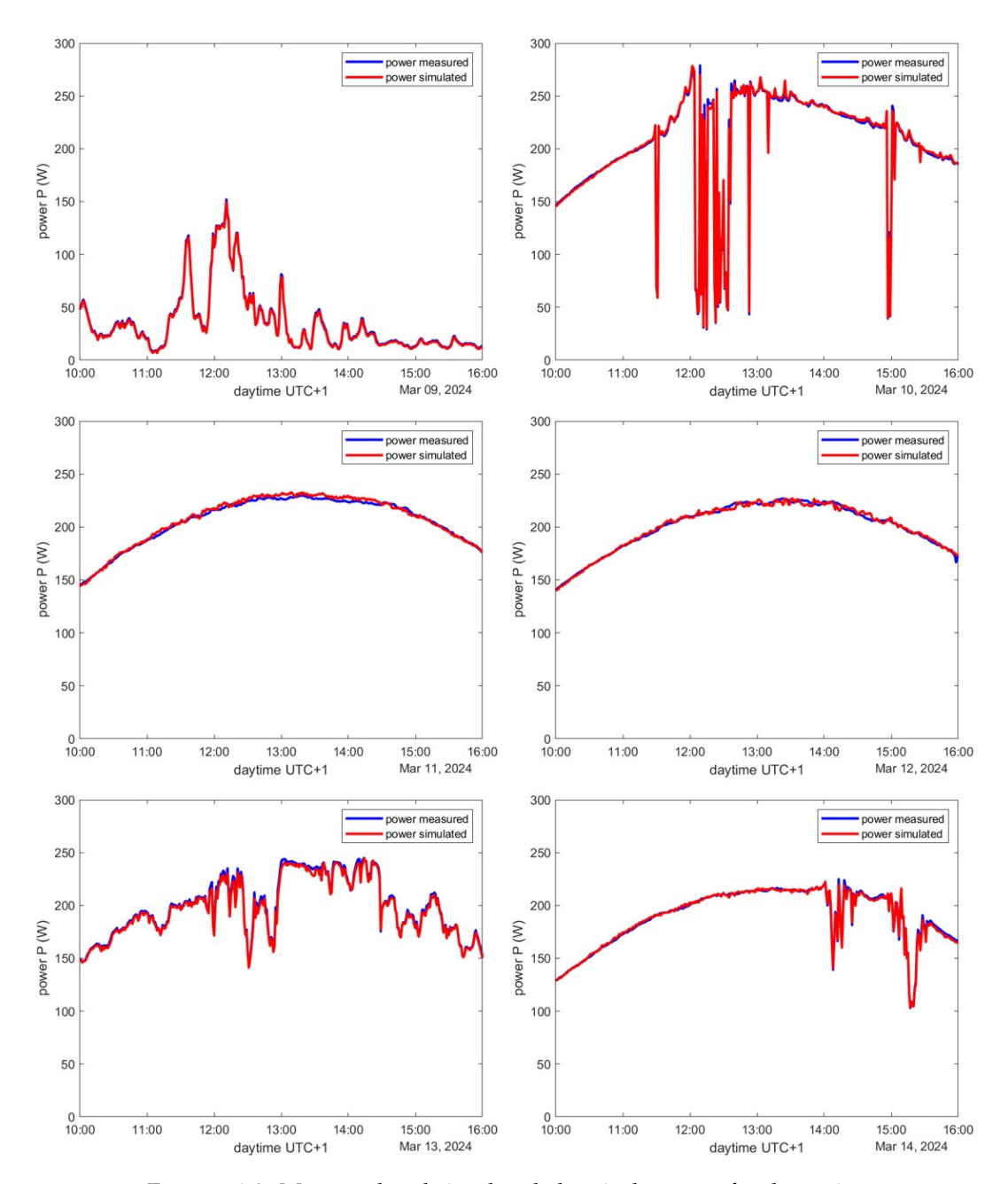


FIGURE 6.9: Measured and simulated electrical powers for the entire time considered for the soiled experiment. Each sub-figure shows the data for one day.

On the 11^{th} of March, the GTI is high and the wind from the west direction is getting continuously stronger over the day. On the 12^{th} the temperature is estimated well. In the morning the temperature is overestimated slightly while it is underestimated slightly in the afternoon, resulting in an RMSE of $12.5\,\mathrm{K}$ and an MBE of $1.5\,\mathrm{K}$. In the morning there is basically no wind and, in the afternoon, there is a slight wind coming from the west direction. The GTI is high. On the 13^{th} the temperature is calculated overall accurately with an RMSE of $7.7\,\mathrm{K}$ and an MBE of $0.9\,\mathrm{K}$. The GTI is high and there is a wind of about $5\,\mathrm{m/s}$ from the east direction. On the 14^{th} of March, the temperature is generally speaking slightly underestimated with an RMSE of $11.2\,\mathrm{K}$ and an MBE of $-6.6\,\mathrm{K}$. The GTI is high and there is a small but continuously increasing wind from the west direction. Over six days, the model performs with an

RMSE of 17.7 K, an MAE of 13.1 K, and an MBE of -9 K.

The deviations found are assumed to be mainly related to the convection modeling. In the west of the PV testbench, there is a big hall that reduces the wind coming from this direction. The meteorological station measuring the wind is not affected by this hall for west winds. This means that in the case of the wind coming from the west direction, the wind speed is systematically overestimated for the convection modeling. This leads to an overestimation of the convection and an underestimation of the temperature. In particular, this explains the deviations for the 10th and 11th of March. For the 9th of March, there is a low GTI and therefore an overall low temperature. This means that also the effect of the convection is less pronounced. For the 12th and the 14th of March, there are overall only small wind speeds present. This causes the deviations to be lower. A more representative wind measurement would most likely improve the results significantly. At the same time, there won't be wind measurements in PV parks close to each PV module in the field either. It is unlikely there will be accurate wind measurements for every location within a large PV park. Hence, the validation mimics a realistic situation and input data accuracy. Even with the observed deviations the model is capable of distinguishing accurately between hotspots and cells with a normal operation temperature.

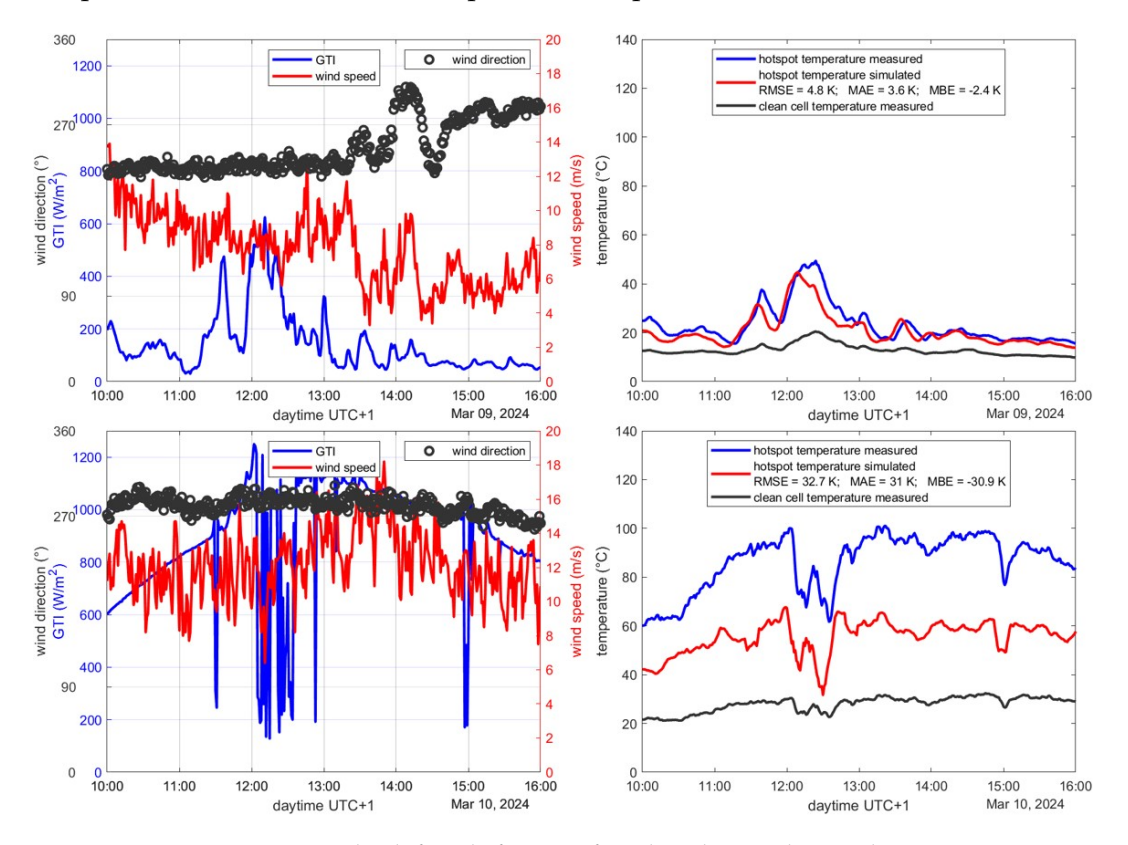


FIGURE 6.10: The left sub-figure of each column shows the most important meteorological data determining the temperature. The wind direction is given in degrees. 0° corresponds to wind coming from the North direction. Then, it is counted clockwise. Meaning e.g. 90° corresponds to wind coming from the East direction. The right sub-figure of each column compares the measured and hotspot temperature simulated by the developed model. Additionally, the temperature of a clean cell, a non-hotspot cell, is shown in dark gray. Data shown for the 9th and 10th of May 2024, between 10:00 and 16:00.

6.3. Results 79

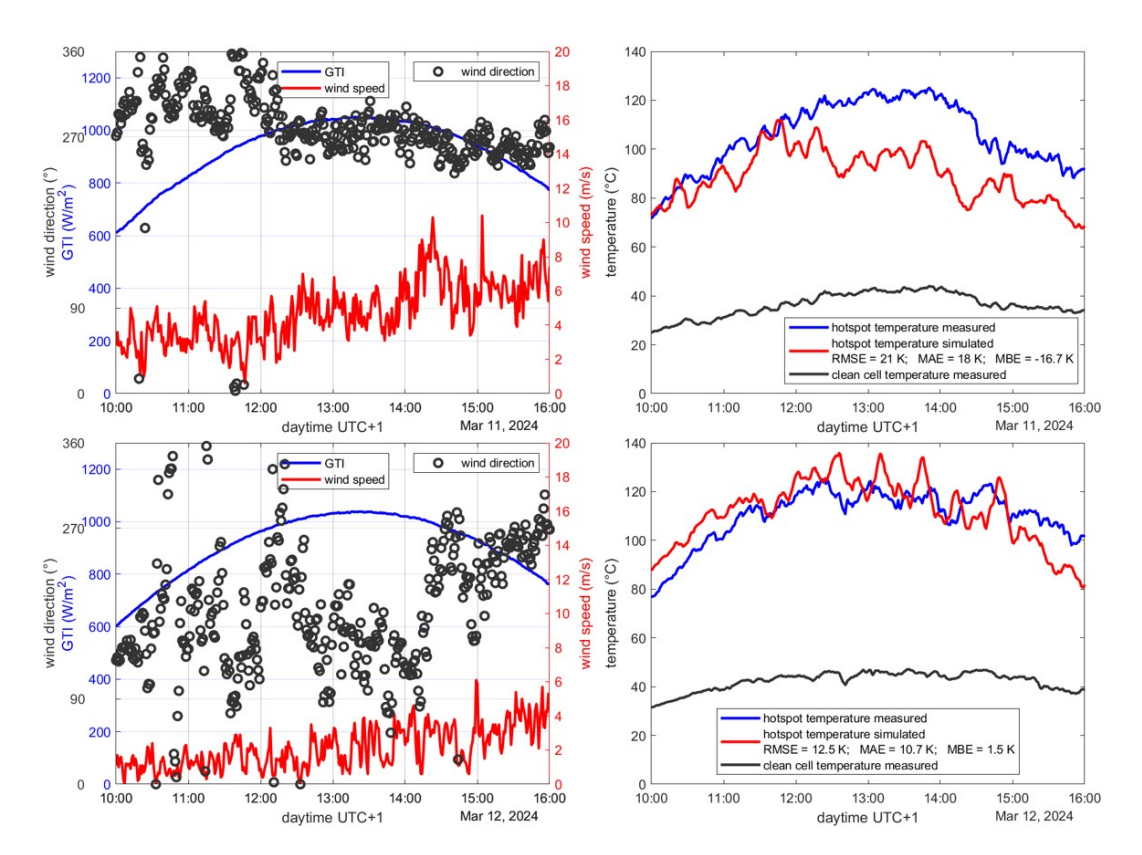


FIGURE 6.11: The left sub-figure of each column shows the most important meteorological data determining the temperature. The right sub-figure of each column compares the measured and hotspot temperature simulated by the developed model. Additionally, the temperature of a clean cell, a non-hotspot cell, is shown in dark gray. Data shown for the 11th and 12th of May 2024, between 10:00 and

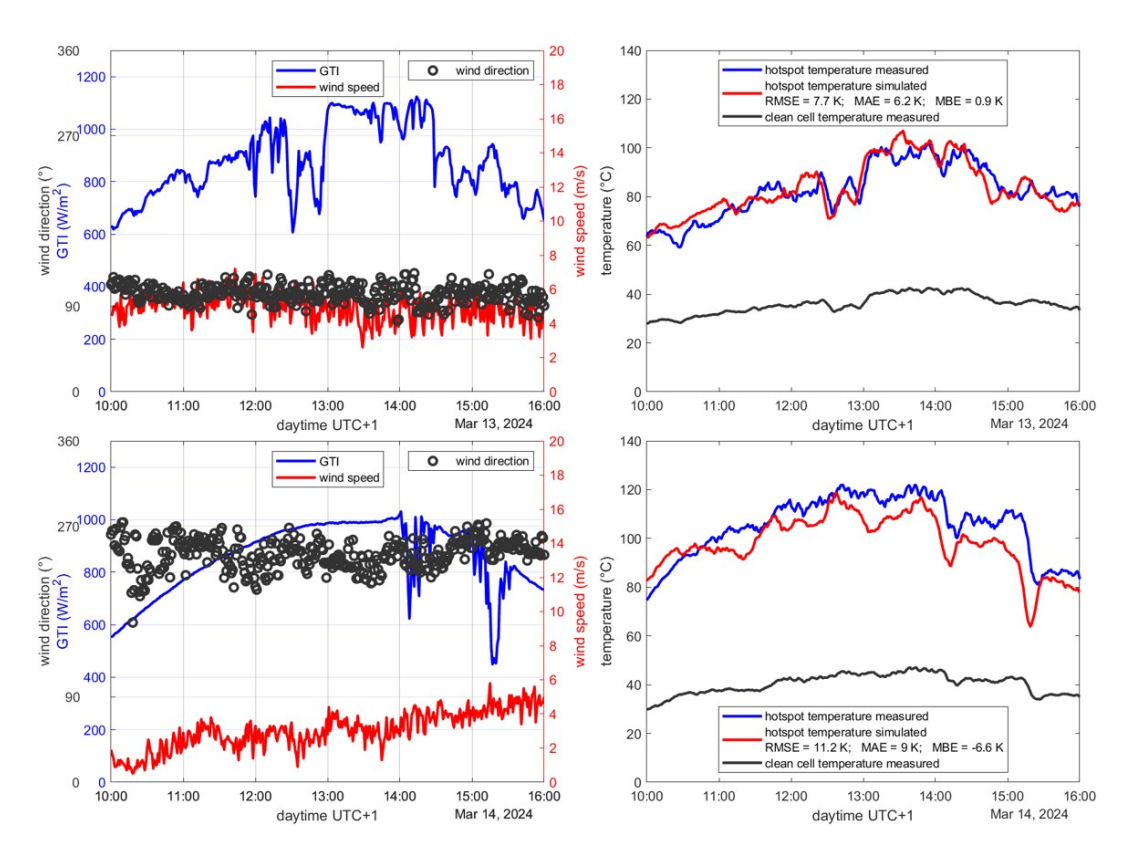


FIGURE 6.12: The left sub-figure of each column shows the most important meteorological data determining the temperature. The right sub-figure of each column compares the measured and hotspot temperature simulated by the developed model. Additionally, the temperature of a clean cell, a non-hotspot cell, is shown in dark gray. Data shown for the 13th and 14th of May 2024, between 10:00 and 16:00

6.4 Conclusions and Outlook

This Chapter has presented a new way of electrothermally modeling soiled PV modules. The model is capable of calculating the IV curves of a module, the electrical power output, and the module temperature with cell-resolution. The calculated IV curves match well with the measured ones and the power under regular operating conditions can be determined accurately (RMSE of the electrical power is $2.1 \, \text{W}$ and MBE is $-0.2 \, \text{K}$ over 6 days and the nominal module power of $390 \, \text{W}$).

The meteorological parameters considered by the thermal model are the GTI measured by a reference cell, the wind speed, the infrared radiation measured by a pyrgeometer, the ambient temperature, and the air pressure. All meteorological data are measured at a weather station 100 meters 100 m north of the testbench that contains the modules of interest. When calculating the temperature of a clean module, the model showed a similar performance to the two most accurate models, the Faiman model and the NOCT model with only minor differences in the error metrics RMSE, MAE, and MBE, out of four well-established models.

The developed model is capable of calculating the hotspot temperature of soiled or partially shaded modules. Over a test period of six days, the temperature estimation showed an RMSE of 17.7 K. At times the temperature prediction was accurate while it deviated for certain conditions. For the best individual day, the RMSE was as low as 4.8 K. The deviations have been explained and differences between the wind conditions directly next to the PV modules compared to the wind at the wind mast are assumed to be the main cause of the deviations. Such a spatial separation of the anemometer and the PV module is also to be expected in real PV plants so the experimental setup is considered to be adequate.

The model manages to correctly predict whether the soiling or shading pattern is sufficient to cause a hotspot. In case an IR image shows a hotspot, the model is capable of stating if the hotspot can be caused by soiling or shading or if it must be caused by a defect.

The developed model can be used to enhance the monitoring of PV plants. The new method is applicable for example in combination with IR monitoring flights. It can potentially be applied on large scales. Further developments of the method can go in different directions. On the one hand, the method can be applied to different kinds of modules. In particular, it could be used for half-cell modules which are nowadays often used. On the other hand, improved convection models that consider also the wind direction could be implemented to enhance the model's accuracy. Also, the developed model could be tested with image-based soiling information.

Chapter 7

Summary and Outlook

A drone camera-based measurement method for soiling on PV modules has been developed. The method is capable of detecting various soiling types and quantifying the losses caused. Electrical mismatch is also considered. In comparison to other methods from the literature, the proposed method achieves great accuracy. Additionally, the method convinces with its wide applicability. The method is not limited to a single soiling type. Also, the camera-based method allows the coverage of big areas in a short time and achieves good spatial resolution.

Chapter 4 presented a new drone-based optical method for measuring the soiling type dust. Dust is typically relatively homogeneously distributed over a given cell. Especially, in arid regions such as North Africa and the Arabian Peninsula, dust is one of the most common soiling phenomena. The method is based on detecting and quantifying the light scattering that takes place on the dust layer of the module surface. The light scattering usually results in dusty modules appearing significantly brighter than clean modules. To calibrate the method, a clean module and a homogeneously soiled module with known electrical losses are required. Both modules are photographed from different perspectives. The images of the clean module are used to calculate a calibration function, which can then specify the brightness of a clean module for different geometries. The value of this calibration function, evaluated for a given geometry, is considered a clean background signal. The images of the soiled module are used to calculate a function that indicates the scattering behavior of the dust layer for different geometries. The increase in brightness caused by the light scattering depends on the angle at which the module is viewed and the angle of incidence of the sunlight. Over various campaigns, the method predicted the soiling loss with an RMSE of 0.93 %. The average soiling loss was about 5 % for the cases analyzed. The method can distinguish between more and less soiled cells and gives a good estimate of the soiling loss. Currently, the calibration of the method is still relatively complex. The cleaning of a module does not represent a great effort. However, the electrical determination of the soiling loss of a homogeneously soiled module can be complex if this loss has to be determined with high accuracy. Further analyses of the two calibration functions can be carried out, which could make it possible to make generalized statements about the dependence on the geometry. It may be possible to perform this calibration once and then apply it to all future measurements.

Chapter 5 presented a new method for measuring inhomogeneous soiling. For example, bird droppings and leaves can be detected. The resulting power losses are quantified. The method is based on the latest work in the field of deep learning applied to object detection and segmentation. The two models SAM and YOLO are used. With reinforcement learning, these models are then optimized for the detection of objects located on top of PV modules. This ensures, for example, that gaps between cells are not labeled as soiling. Soiling on the modules is detected and the covered area

is measured. A transmission value is then assigned to each soiling spot. The spaces between the cells are excluded and the soiling is allocated to the individual cells. The optical losses are converted into electrical losses using the electrical model that was derived in this work. Various types of soiling were detected in a measurement campaign. For the first analyzed module, the deviation between the image-based method and the electrical reference is 0.5% and for the second module, the deviation is 0.7%. The soiling loss was about 15% for both cases. Future work may consist of training the model with various other types of soiling so that this can also be recognized afterwards. For example, silicon and cadmium telluride (CdTe) modules with different dark soiling can be considered. Modules of both technologies tend to look dark blue and black. Comprehensive training could lead to better recognition of dark (black) soiling on silicon modules.

Chapter 6 introduced a new electro-thermal model. This model is optimized to use the outputs of the previously developed models as input. It is capable of converting optical losses into electrical losses, i.e. to determine electrical mismatch. It can also calculate the module temperature for a clean module. Also, the temperature of a soiling-based hotspot can be calculated. In a validation campaign, the electrical power, the IV curves, and the hotspot temperature, among other things, were validated. With the help of the developed model, it is possible to determine the cause of an occurring hotspot. If a hotspot is observed on an IR image, the developed model can be used together with a cell-resolved soiling measurement to determine whether this hotspot is caused by soiling or a defect. Future work could focus on extending the electrothermal model to a series connection of modules. Half-cell modules can also be considered in the future. Another possible point is an extended consideration of the meteorological parameters. Wind speed is currently taken into account. Wind direction, on the other hand, is currently neglected. In reality, the convection that leads to the cooling of the PV module will also depend on the wind direction. Convection models can become infinitely complex.

This work has presented a promising method of measuring the impact of soiling in PV parks. Potential enhancements can go in different directions. The methods can be adapted to static camera systems as well. This would allow the continuous monitoring of PV parks with surveillance cameras. Drone flight would not be necessary anymore. On the other hand, the methods should be tested at different sites. Different sites have different modules and show different soiling types. In particular, the method can be tested with more real operating conditions to avoid the partially used artificial soiling. One aspect that is currently limiting the practicality of the method is the calibration of the dust quantification method. The operation of a soiled calibration module with individual power tracking is not desirable. Detailed studies of the scattering properties of dust might allow a simplification of the calibration.

Appendix A

Electrical Reference Measurements

Two ways are used to electrically determine the soiling losses $SL_{\rm ref}$ of the modules for the calibration and validation in this work. Firstly and more accurately, the power of the soiled module is compared to the power of the clean module. Additionally, a normalization factor has to be applied which considers that the modules have different nominal powers and have aged differently. Therefore, the ratio of powers is normalized by its value when both modules are clean (see Section 2.2.1 and (Gostein et al., 2013)).

Alternatively, the power of the soiled module can also be compared to its expected power in the clean state calculated using reference cell data (see Section 2.2.1 and (Gostein et al., 2016)). On a day when both the reference cell and the module are clean, the ratio between module power and the reference cell temperature-corrected GTI is calculated in a symmetrical time window of one hour around solar noon. The same ratio is determined for the measurement day where the module is soiled and the reference cell continues to be clean. By dividing both ratios and applying a temperature correction for the module power, the soiling ratio is obtained. The PV module temperature has to be considered as the module temperature increases as its efficiency decreases. For normal operating temperatures, a linear dependence between the module temperature and efficiency is valid. The manufacturer states the temperature coefficient in the data sheet, -0.4% per Kelvin temperature increase. The module temperature is measured with a Pt-1000 (see Chapter 3) and the module power will be temperature-corrected to an arbitrarily chosen reference temperature of 40 °C for every timestamp. The corrected power is calculated by considering the measured deviation from the reference temperature and multiplying the temperature difference with the temperature coefficient from the data sheet. In the case of determining the soiling loss by comparing the soiled modules' powers to the clean module's power, a temperature correction is not necessary because it is assumed that the clean and the soiled module have a very similar temperature and their efficiencies are assumed to have the same temperature dependence. This way it is indifferent if the modules have a different temperature on the measurement day and the reference day. As mentioned above, the reference cell data are also temperature corrected. The short circuit current increases with the temperature. In the case of the used module, the coefficient of the short circuit current increase is 0.04% per Kelvin.

For the first campaign, the soiling losses are determined by comparing to the reference cell as the power of the clean module was then not recorded continuously. For the following campaigns, the soiling is determined via the module-to-module comparison method.

For all electrical measurements, data of up to one hour around solar noon are considered. This is a tradeoff between achieving better statistics because of a large number of data points and at the same time ensuring that only low incidence angles are used. In the morning and in the evening, the sunlight falls on the module at a

high incidence angle. This changes the soiling loss as the soiling layer appears thicker for higher incidence angles (see Chapter 2). Additionally, small misalignments of the module planes, which are negligible for nearly normal incidence, typically show a higher impact in the morning and evening hours. It has been found that the module and the reference cell are sufficiently in plane so that a correction for the incidence angle is not necessary when analyzing only data close to solar noon.

A.1 First Campaign, Dust-Like Soiling

For the first campaign, the electrical reference of the soiling loss was determined by comparing the modules' power output with the GTI measured by a reference cell (see Chapter 2). Figure A.1 shows the ratio of module power to GTI for a reference day on which both devices were clean. This day is used to calibrate the modules relative to the reference cell. The GTI, the module temperature, and the wind speed at 10 m height are shown in Figure A.2 for the reference day and the day of the drone-based soiling measurement. The determined calibration factor is then used to calculate the soiling loss on the measurement day as shown in Figure A.3. Module 1 is not shown in either figure because the module was cleaned before the measurement and is therefore defined to have a soiling loss of zero. Note that for the optical calculation of the soiling loss, an angle correction was applied (see Equation 4.12). The same angle correction should be applied for the electrical measurements for the sake of consistency. This was carried out in a test run and it was found that for the electrical measurements, the angle dependence played a neglectable role as the angle of incidence was very close to zero for the time interval of interest. This is due to the modules' inclination of 30° and because the electrical measurements took place around solar noon. Furthermore, the experiments took place in April and September, which are months in which the sun reaches around 60° elevation at solar noon in Almería. Together with the 30° inclination, this leads to a nearly perpendicular incidence.

Figure A.2 also shows in the center the measured module temperature for the measurement day and the reference day. The temperature is measured at module 3 in both cases. It is assumed that the temperature is very similar for all four modules since they are of the same technology, from the same manufacturer, have the same orientation, and experience very similar operating conditions. Especially, it should be noted that the soiling is not significant enough to cause a hotspot. The lower two sub-figures of Figure A.2 show the wind speed on both days as the wind speed is a key parameter influencing the module temperature.

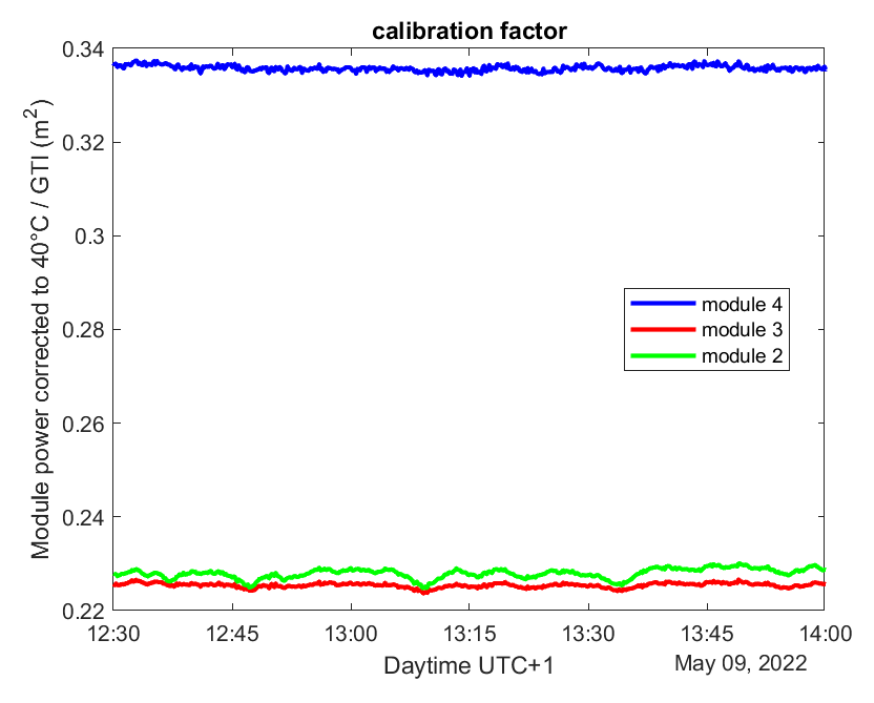


FIGURE A.1: Calibration factor for the electrical calculation of the reference soiling loss for the first campaign measured with clean devices (reference day). The powers of modules 2, 3, and 4 are divided by the GTI measured by a reference cell. The derived calibration factors are $0.228\,\mathrm{m}^2$, $0.2254\,\mathrm{m}^2$, and $0.3248\,\mathrm{m}^2$ for modules 2, 3, and 4, respectively.

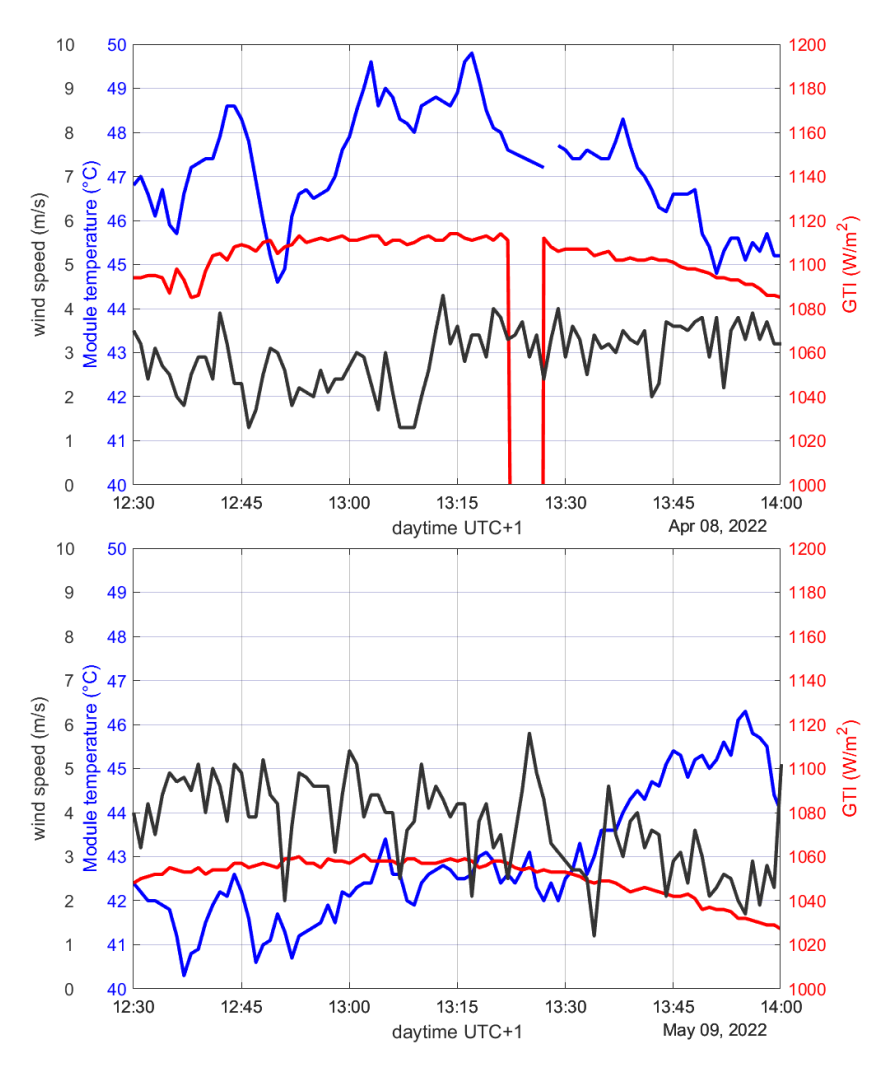


FIGURE A.2: Module temperature, GTI and wind speed of the for the first campaign. The upper sub-figure corresponds to the measurement day itself and the lower sub-figure corresponds to the clean reference day. The module temperature is used to account for the temperature correction, as the module efficiency decreases with increasing temperature. Note that, for the measurement day data between 13:23 and 13:27 is neglected.

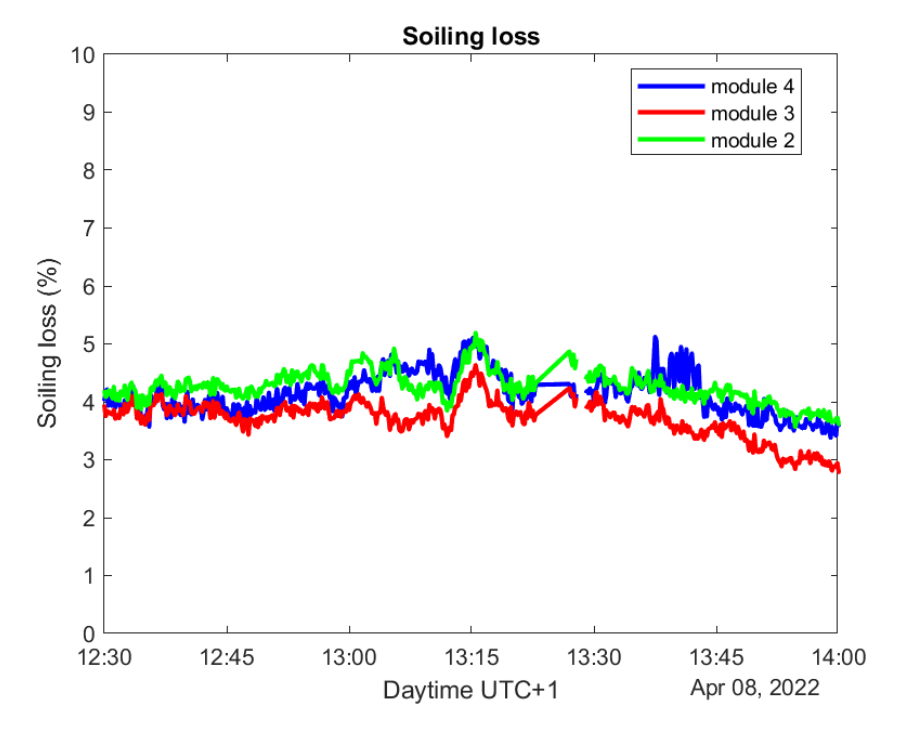


FIGURE A.3: Soiling loss for modules 2, 3, and 4 during the first campaign. The module powers are divided by the GTI and then divided by the previously determined calibration factor. The averaged soiling losses of modules 2, 3, and 4 are 4.2%, 3.7%, and 4.1%, respectively. Data between 13:22 and 13:27 were excluded as the reference cell was shaded by the scientists.

A.2 Second Campaign, Dust-Like Soiling

For the second campaign, the soiling loss was determined by comparing the powers of the soiled modules with the power of the clean module. Figure A.4 shows the ratio of powers for the case in which all modules are clean. The powers of modules 2, 3, and 4 are divided by the power of the clean module 1. Thus, the determined calibration factor is applied to obtain the soiling loss. Figure A.5 shows the calculated soiling loss for the measurement day itself.

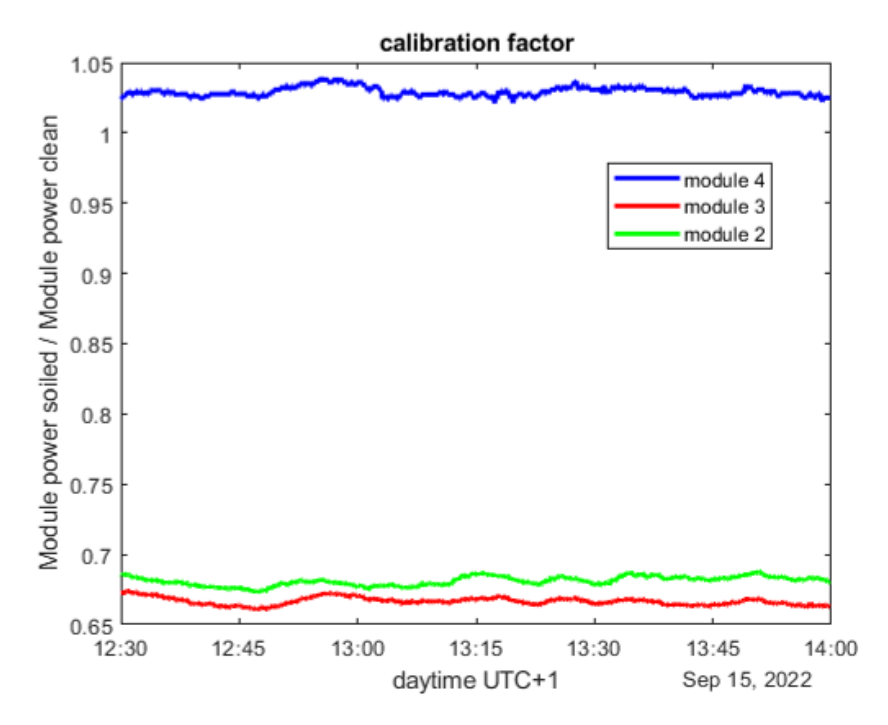


FIGURE A.4: Calibration factors for the electrical calculation of the reference soiling loss for the second campaign. The powers of modules 2, 3, and 4 are divided by the power of module 1 on a day on which all modules are clean. The derived calibration factors are 0.681, 0.6666, and 1.0291 for modules 2, 3, and 4, respectively.

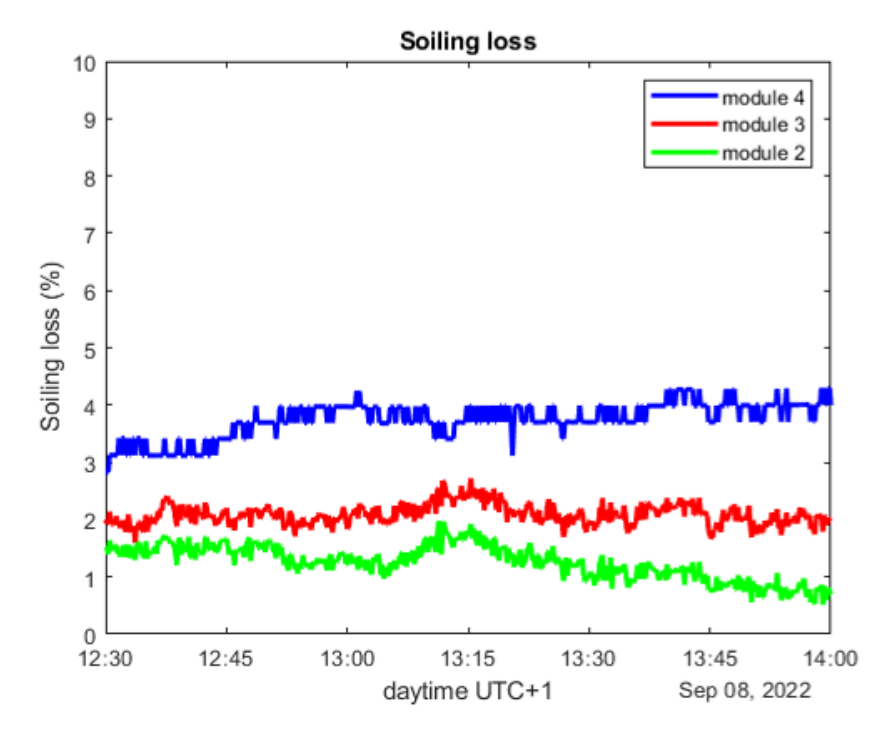


FIGURE A.5: Calculation of the soiling loss for modules 2, 3, and 4 during the second campaign. The module powers are divided by the power of module 1 and then divided by the previously determined calibration factor. The calculated soiling losses are 1.25%, 2.09%, and 3.75% for modules 2, 3, and 4, respectively.

A.3 Third Campaign, Dust-Like Soiling

The soiling loss is determined analogous to the second campaign. The corresponding Figures are A.6 and A.7.

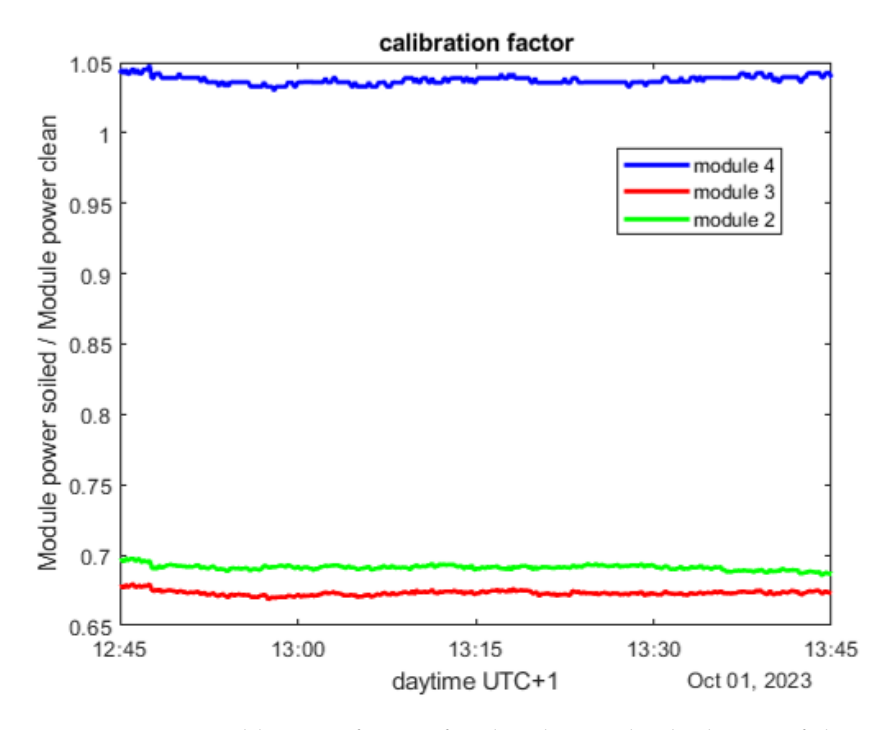


FIGURE A.6: Calibration factors for the electrical calculation of the reference soiling loss for the third campaign. The powers of modules 2, 3, and 4 are divided by the power of module 1 on a day on which all modules are clean. The derived calibration factors are 0.6911, 0.6729, and 1.0373 for modules 2, 3, and 4, respectively.

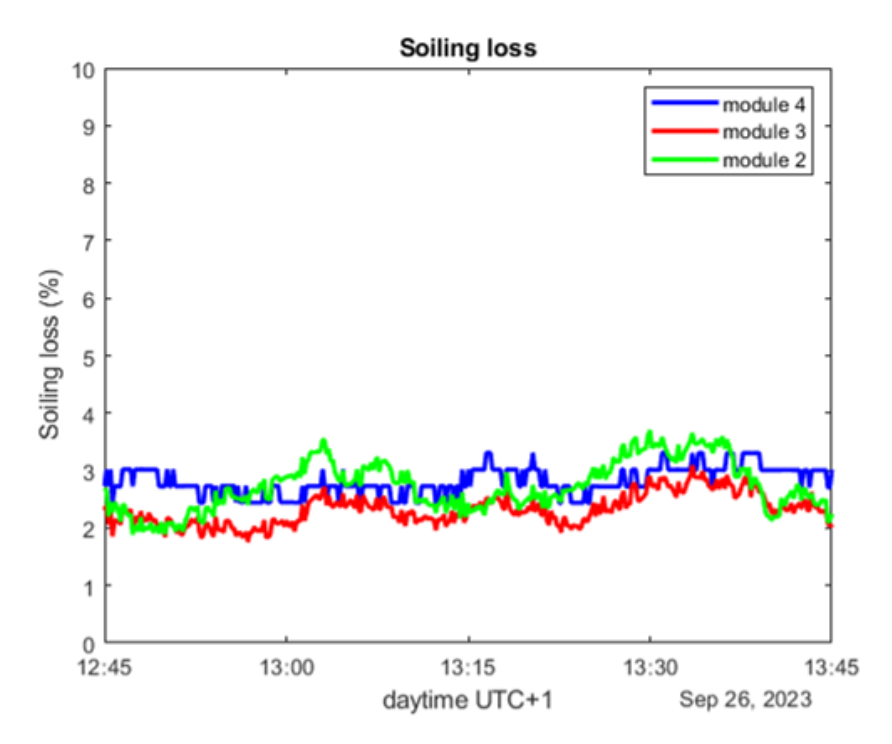


FIGURE A.7: Calculation of the soiling loss for modules 2, 3, and 4 during the third campaign. the module powers are divided by the power of module 1 and then divided by the previously determined calibration factor. The calculated losses are 2.72%, 2.32%, and 2.82% for modules 2, 3, and 4, respectively.

A.4 Experiment with Inhomogeneous Soiling

The electrical loss is determined by comparing the power of the soiled modules to a clean module, as described in Chapter 2. Figure A.8 shows the ratio of the powers to each other as a calibration factor. Modules 1 and 4 are soiled and module 2 is the clean reference. Figure A.9 shows the electrical soiling loss over time. After averaging, there is a loss of 13.9% for module 1 and a loss of 14.1% for module 4.

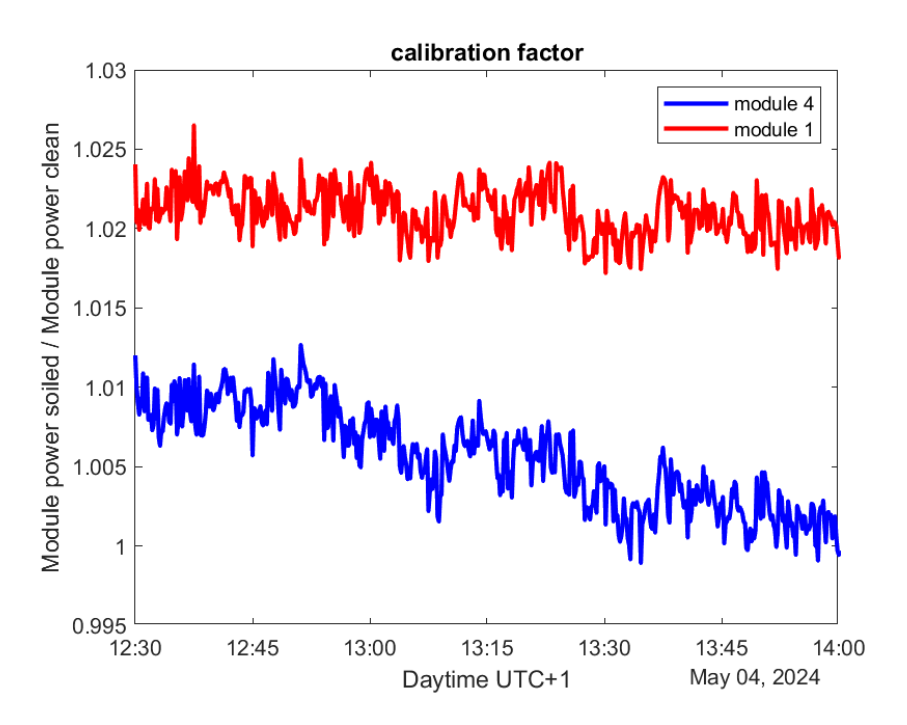


FIGURE A.8: Calibration of the power ratios for modules. The calculated calibration factor is 1.006 for module 1 and 1.021 for module 4. *Module power clean* refers to the power of module 2 which has been cleaned.

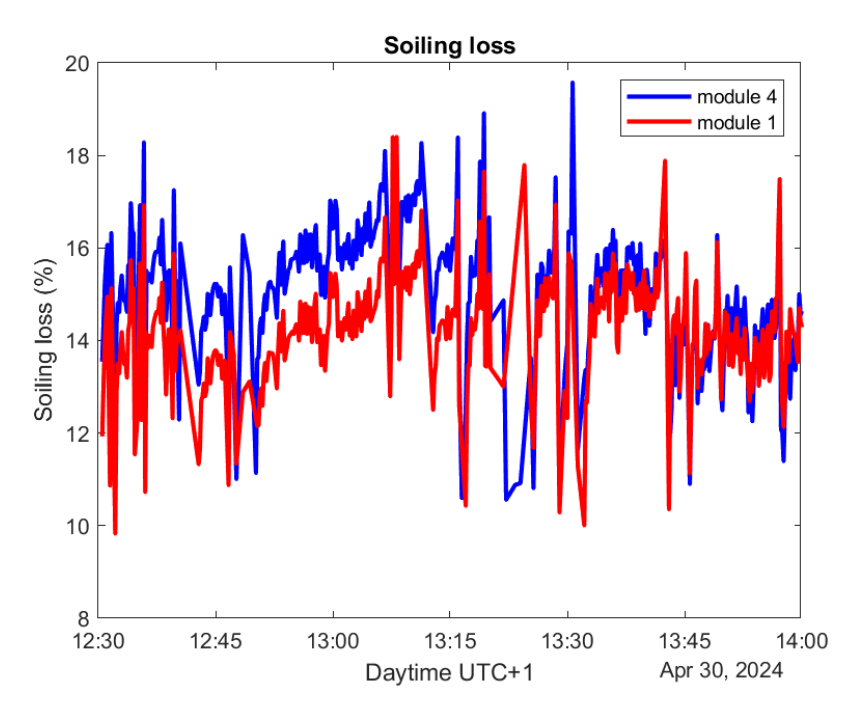


Figure A.9: Soiling loss of both modules of interest. The calculated soiling loss is 13.9% for module 1 and 14.1% for module 4.

Appendix B

Measurement Flights for the Measurement of Dust

In Chapter 4 three measurement campaigns have been discussed. For each campaign one flight has been shown. The first campaign consisted of four flights, the second campaign consisted of three flights, and the third campaign consisted of one flight only. The evaluations of the remaining flights, the evaluations that have not yet been shown in Chapter 4 are now shown in this Chapter.

B.1 First Campaign

B.1.1 Second Flight

Figure B.1 summarizes the results of the second flight of the first campaign. The soiling of the first validation module is determined with a deviation of 0.1% absolute. The soiling of the second validation module is determined with a deviation of 1.0% absolute. It should be noted that the second validation module was soiled with a different soiling type than the other modules which explains an increased deviation.

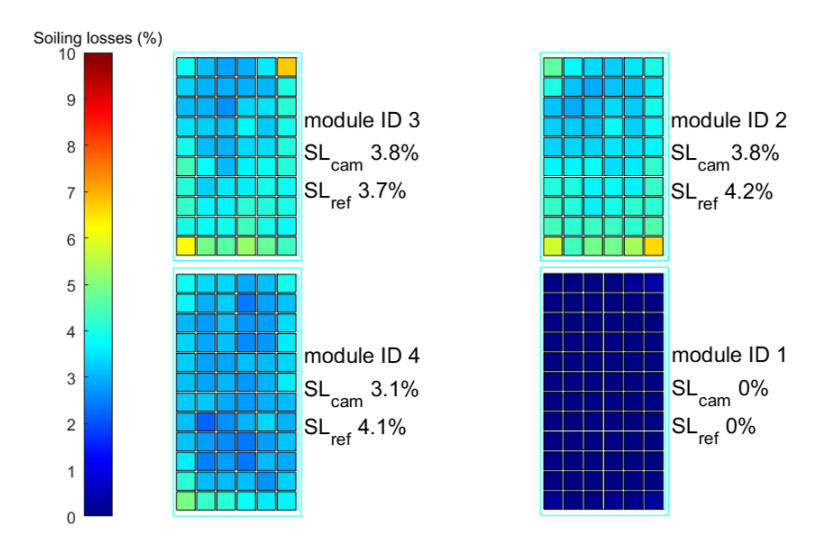


FIGURE B.1: Result plot of the second measurement flight of the first campaign. The lower right module was chosen to be the clean reference module while the upper right module was chosen to be the soiled reference module. The upper numbers label the modules. The number in the middle states the optically measured soiling loss while the lower number is the electrical reference loss.

B.1.2 Third Flight

Figure B.2 summarizes the results of the third measurement flight of the first campaign. The soiling of the first validation module is determined with a deviation of 0.1% absolute. The soiling of the second validation module is determined with a deviation of 1.0% absolute. It should be noted that the second validation module was soiled with a different soiling type than the other modules which explains an increased deviation.

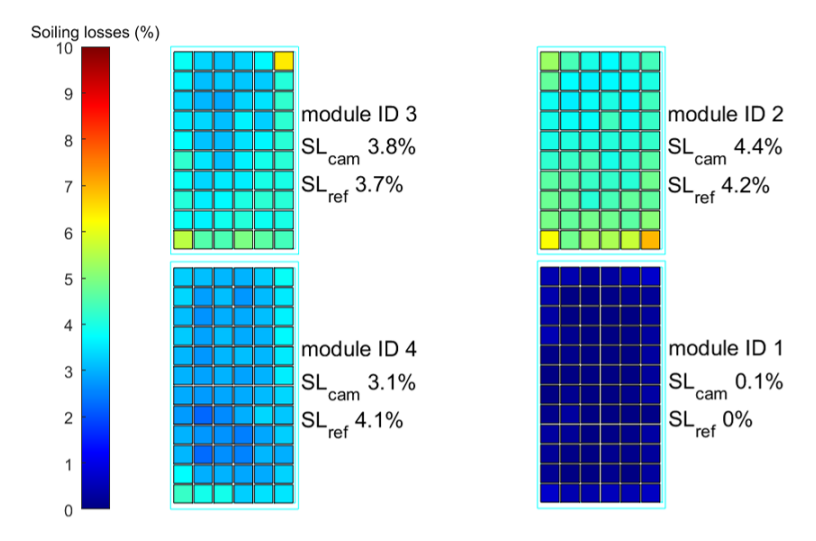


FIGURE B.2: Result plot of the third measurement flight of the first campaign. The lower right module was chosen to be the clean reference module while the upper right module was chosen to be the soiled reference module. The upper numbers label the modules. The number in the middle states the optically measured soiling loss while the lower number is the electrical reference loss.

B.1.3 Fourth Flight

Figure B.3 summarizes the results of the fourth measurement flight of the first campaign. The soiling of the first validation module is determined with a deviation of 0.4% absolute. The lower left module was used as second validation module and it was cleaned before the flight. This explains the different soiling loss compared to the other three flights of the same campaign. The soiling of the second validation module is determined with a deviation of 0.3% absolute.

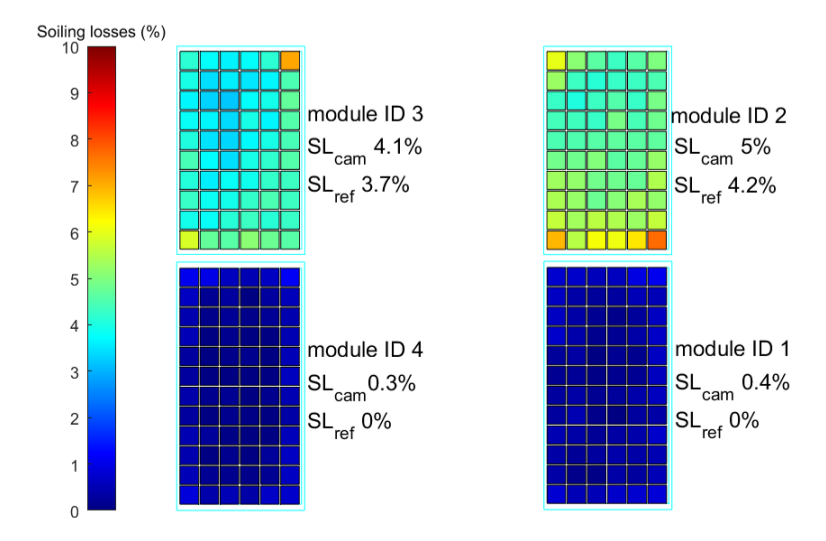


FIGURE B.3: Result plot of the fourth measurement flight of the first campaign. The lower right module was chosen to be the clean reference module while the upper right module was chosen to be the soiled reference module. The lower left module was cleaned before the flight which explains the different soiling loss compared to the other three flights of the same campaign. The upper numbers label the modules. The number in the middle states the optically measured soiling loss while the lower number is the electrical reference loss.

B.2 Second Campaign

B.2.1 Second Flight

Figure B.4 summarizes the results of the second measurement flight of the second campaign. The soiling of the first validation module is determined with a deviation of 1.0% absolute. The soiling of the second validation module is determined with a deviation of 0.4% absolute.

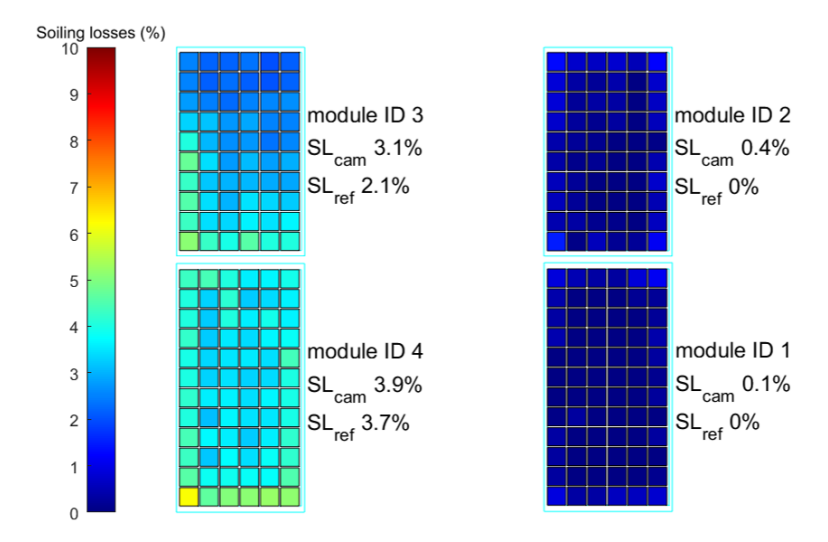


FIGURE B.4: Result plot of the second measurement flight of the second campaign. The lower right module was chosen to be the clean reference module while the lower left module was chosen to be the soiled reference module. The upper numbers label the modules. The number in the middle states the optically measured soiling loss while the lower number is the electrical reference loss.

B.2.2 Third Flight

Figure B.5 summarizes the results of the third measurement flight of the second campaign. The left sub-string of the upper left module was cleaned before the flight (two columns of cells cleaned). The soiling of the first validation module is determined with a deviation of 0.1% absolute. In case of the second validation module, the electrically and optically measured soiling losses are identical.

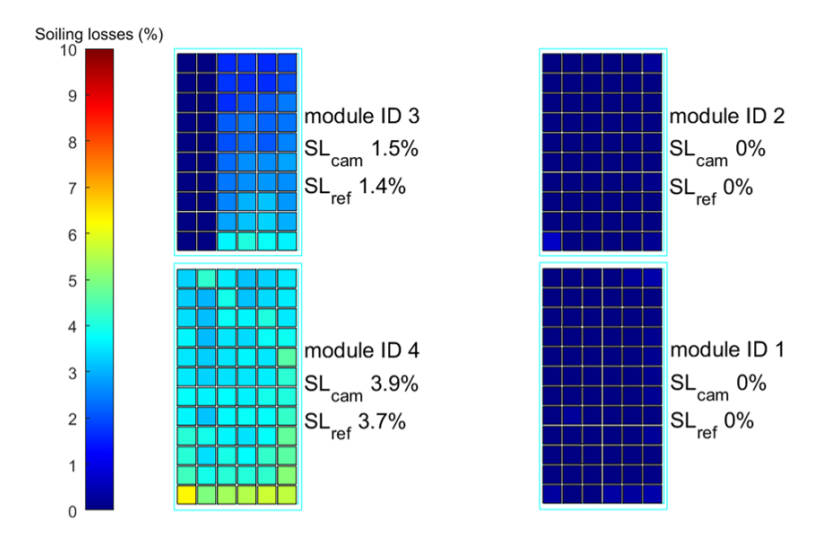


FIGURE B.5: Result plot of the third measurement flight of the second campaign. The lower right module was chosen to be the clean reference module while the lower left module was chosen to be the soiled reference module. The left sub-string of the upper left module was cleaned before the flight (two columns of cells cleaned). The upper numbers label the modules. The number in the middle states the optically measured soiling loss while the lower number is the electrical reference loss.

Appendix C

Further Validations of the Electrothermal Model

The electrothermal model has been validated in two campaigns. In the first campaign the module of interest was clean while in the second one the module was partially soiled. The first campaign consisted of six days. Two of these six days have already been discussed in the Chapter 6. For readability, the other days are discussed here.

Figures C.1 and C.2 (right) show the temperature modeled by the developed model and the models form literature and compare them to the measured temperature. The relevant meteorological parameters (measured as described in Chapter 6), namely the GTI and the wind speed, are shown on the left hand side.

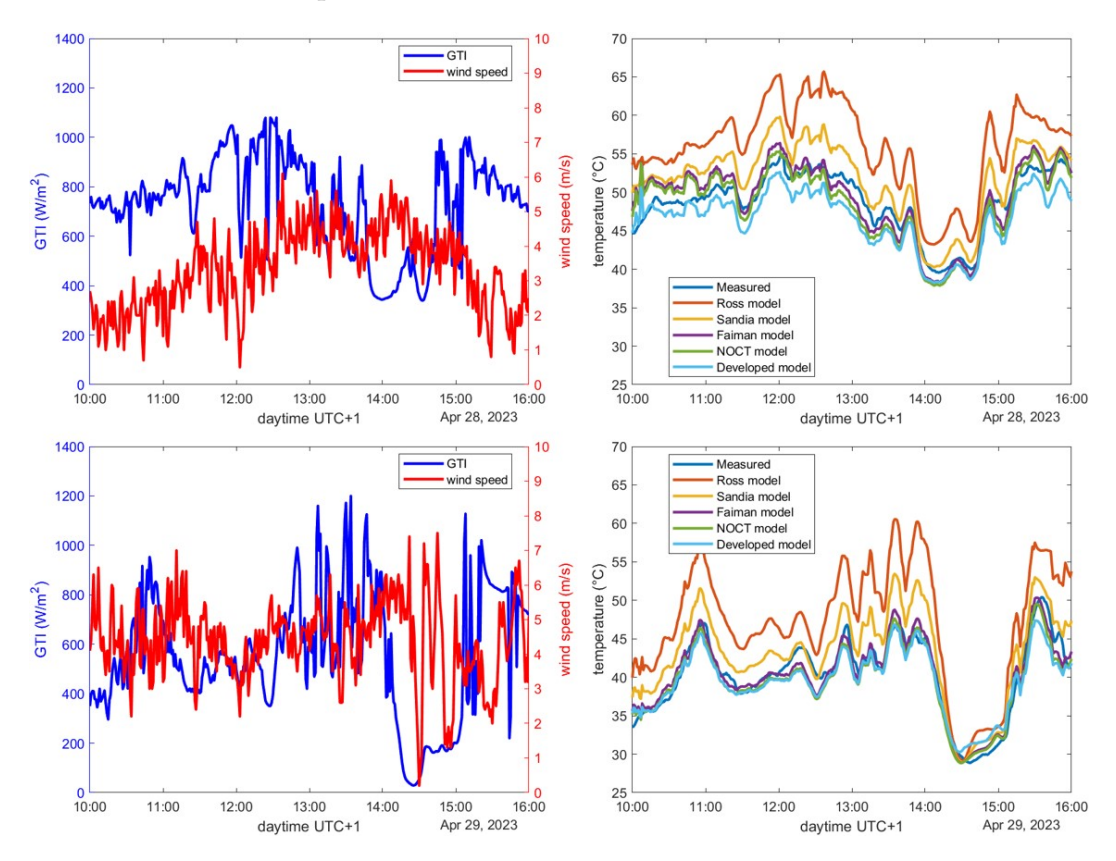


FIGURE C.1: Comparison of the developed model with the measured temperature and the thermal models from literature discussed in Chapter 2 for the 28th and the 29th of April 2023.

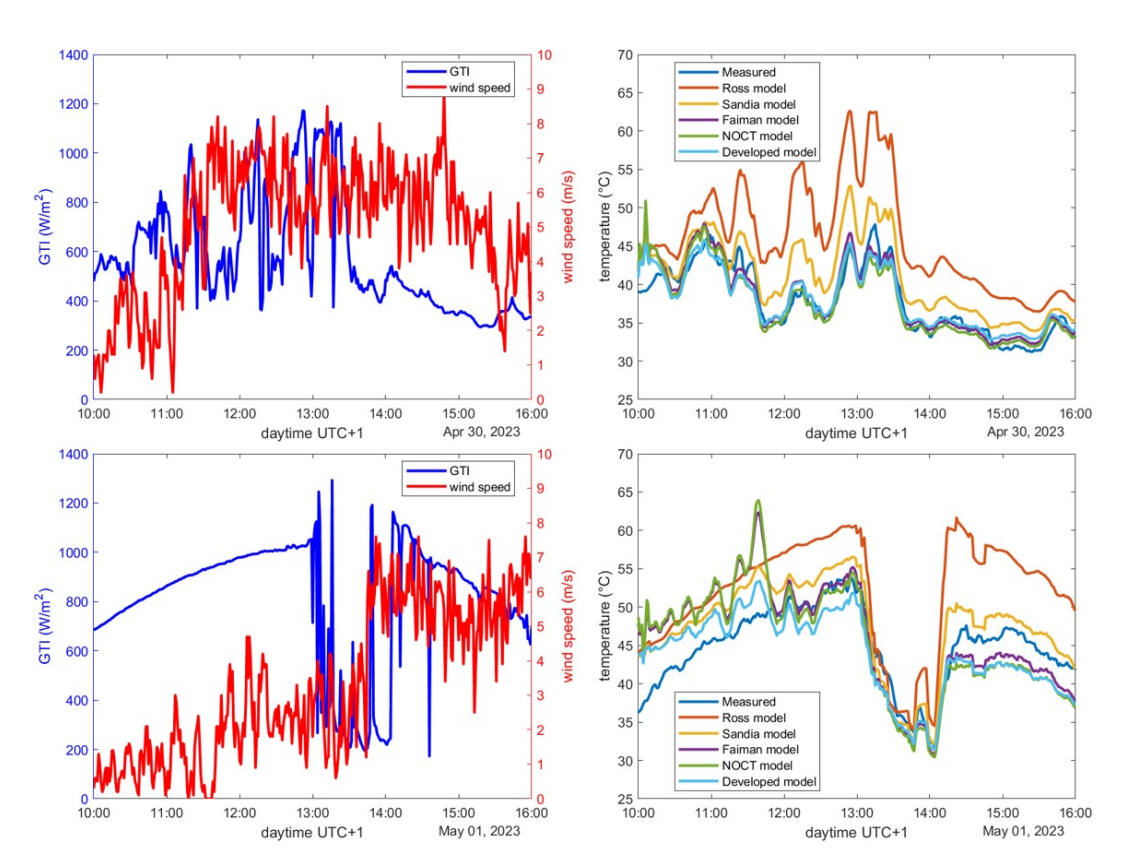


Figure C.2: Comparison of the developed model with the measured temperature and the thermal models from literature discussed in Chapter ${\color{red}2}$ for the 30th of April and the 1st of May 2023.

- Aïssa, Brahim et al. (2022). "PV-soiling field-assessment of MarsTM optical sensor operating in the harsh desert environment of the state of Qatar". In: *Solar Energy* 239, pp. 139–146.
- Akram, M Waqar et al. (2019). "CNN based automatic detection of photovoltaic cell defects in electroluminescence images". In: *Energy* 189, p. 116319.
- Akram, M Waqar et al. (2020). "Automatic detection of photovoltaic module defects in infrared images with isolated and develop-model transfer deep learning". In: *Solar Energy* 198, pp. 175–186.
- Al-Hasan, Ahmad Y and Adel A Ghoneim (2005). "A new correlation between photovoltaic panel's efficiency and amount of sand dust accumulated on their surface". In: *International Journal of Sustainable Energy* 24.4, pp. 187–197.
- Al Siyabi, Idris et al. (2021). "Effect of soiling on solar photovoltaic performance under desert climatic conditions". In: *Energies* 14.3, p. 659.
- Araghi, Alireza et al. (2017). "Forecasting soil temperature based on surface air temperature using a wavelet artificial neural network". In: *Meteorological Applications* 24.4, pp. 603–611.
- Atonometrics (2024). Mars soiling sensor. URL: https://www.atonometrics.com/products/mars-soiling-sensor (visited on 09/30/2024).
- Bell, Caleb (2023). Contributors, "Thermo: Chemical properties component of chemical engineering design library (ChEDL),"
- Beuter, Fabian (2023). "Machine-Learning-Based Soiling Detection and Segmentation on Photovoltaic Modules using Digital Image Processing". RWTH Aachen University.
- Bishop, Christopher M (2006). "Pattern recognition and machine learning". In: *Springer google schola* 2, pp. 1122–1128.
- Bishop, JW (1988). "Computer simulation of the effects of electrical mismatches in photovoltaic cell interconnection circuits". In: *Solar cells* 25.1, pp. 73–89.
- Bochkovskiy, Alexey, Chien-Yao Wang, and Hong-Yuan Mark Liao (2020). "Yolov4: Optimal speed and accuracy of object detection". In: *arXiv* preprint arXiv:2004.10934.
- Breitenstein, Otwin et al. (2011). "Can luminescence imaging replace lock-in thermography on solar cells?" In: *IEEE Journal of Photovoltaics* 1.2, pp. 159–167.
- Campos, Laura et al. (2023). "Autonomous measurement system for photovoltaic and radiometer soiling losses". In: *Progress in Photovoltaics: Research and Applications* 31.12, pp. 1336–1349.
- Cao, Yukang et al. (2024). "Improved yolov8-gd deep learning model for defect detection in electroluminescence images of solar photovoltaic modules". In: *Engineering Applications of Artificial Intelligence* 131, p. 107866.
- Caron, J Riley and Bodo Littmann (2012). "Direct monitoring of energy lost due to soiling on first solar modules in California". In: *IEEE Journal of Photovoltaics* 3.1, pp. 336–340.
- Cavieres, Robinson et al. (2022). "Automatic soiling and partial shading assessment on PV modules through RGB images analysis". In: *Applied Energy* 306, p. 117964.

Chen, Daniel et al. (2021). "Progress in the understanding of light-and elevated temperature-induced degradation in silicon solar cells: a review". In: *Progress in Photovoltaics: Research and Applications* 29.11, pp. 1180–1201.

- Chen, Xin, Todd Karin, and Anubhav Jain (2022). "Automated defect identification in electroluminescence images of solar modules". In: *Solar Energy* 242, pp. 20–29.
- Cole, RJ and NS Sturrock (1977). "The convective heat exchange at the external surface of buildings". In: *Building and Environment* 12.4, pp. 207–214.
- Conceição, Ricardo et al. (2018). "Organic soiling: The role of pollen in PV module performance degradation". In: *Energies* 11.2, p. 294.
- Cook, John et al. (2016). "Consensus on consensus: a synthesis of consensus estimates on human-caused global warming". In: *Environmental research letters* 11.4, p. 048002.
- Cordero, RR et al. (2018). "Effects of soiling on photovoltaic (PV) modules in the Atacama Desert". In: *Scientific reports* 8.1, p. 13943.
- Deitsch, Sergiu et al. (2019). "Automatic classification of defective photovoltaic module cells in electroluminescence images". In: *Solar Energy* 185, pp. 455–468.
- Devi, Archana and Sreedharan K Satheesh (2022). "Global maps of aerosol single scattering albedo using combined CERES-MODIS retrieval". In: *Atmospheric Chemistry and Physics* 22.8, pp. 5365–5376.
- Devi, Archana and Sreedharan Krishnakumari Satheesh (2021). "Global maps of aerosol single scattering albedo using combined CERES-MODIS retrieval." In: *Atmospheric Chemistry & Physics Discussions*.
- Di Tommaso, Antonio et al. (2022). "A multi-stage model based on YOLOv3 for defect detection in PV panels based on IR and visible imaging by unmanned aerial vehicle". In: *Renewable energy* 193, pp. 941–962.
- DJI (2024). Support for Mavic 2. https://www.dji.com/de/support/product/mavic-2. website. visited on 2024-08-06. URL: https://www.dji.com/de/support/product/mavic-2.
- Dunn, Lawrence et al. (2013). "PV module soiling measurement uncertainty analysis". In: 2013 IEEE 39th Photovoltaic Specialists Conference (PVSC). IEEE, pp. 0658–0663.
- Einhorn, Asher et al. (2018). "Evaluation of soiling and potential mitigation approaches on photovoltaic glass". In: *IEEE Journal of Photovoltaics* 9.1, pp. 233–239.
- El-Shobokshy, Mohammad S and Fahmy M Hussein (1993). "Degradation of photovoltaic cell performance due to dust deposition on to its surface". In: *Renewable energy* 3.6-7, pp. 585–590.
- Elminir, Hamdy K et al. (2006). "Effect of dust on the transparent cover of solar collectors". In: *Energy conversion and management* 47.18-19, pp. 3192–3203.
- Enriquez, R et al. (2012). "Ground reflectance estimation by means of horizontal and vertical radiation measurements". In: *Solar Energy* 86.11, pp. 3216–3226.
- Esquelli, Adil (2020). "Optical PV cleanliness measurement adaptation and soiling loss quantification". Technische Universität Berlin.
- Faiman, David (2008). "Assessing the outdoor operating temperature of photovoltaic modules". In: *Progress in Photovoltaics: Research and Applications* 16.4, pp. 307–315.
- Fernández, EF et al. (2019). "Soiling Spectral Deposition Detector". In: *USPTO* 312548, A1.
- Fernández-Solas, Álvaro et al. (2020). "Design, characterization and indoor validation of the optical soiling detector "DUSST"". In: *Solar Energy* 211, pp. 1459–1468.
- Ferretti, Nicoletta (2018). "PV module cleaning-market overview and basics". In: *PI Photovoltaik-Institut Berlin AG*.

Figgis, Benjamin et al. (2016). "Outdoor soiling microscope for measuring particle deposition and resuspension". In: *Solar Energy* 137, pp. 158–164.

- Gallardo-Saavedra, Sara et al. (2020). "Infrared thermography for the detection and characterization of photovoltaic defects: comparison between illumination and dark conditions". In: *Sensors* 20.16, p. 4395.
- Garcìa, MC Alonso et al. (2003). "Thermal and electrical effects caused by outdoor hot-spot testing in associations of photovoltaic cells". In: *Progress in photovoltaics:* research and applications 11.5, pp. 293–307.
- Garg, HP (1974). "Effect of dirt on transparent covers in flat-plate solar energy collectors". In: *Solar Energy* 15.4, pp. 299–302.
- Geisemeyer, I et al. (2014). "Prediction of silicon PV module temperature for hot spots and worst case partial shading situations using spatially resolved lock-in thermography". In: *Solar Energy Materials and Solar Cells* 120, pp. 259–269.
- Gillett, Nathan P et al. (2011). "Ongoing climate change following a complete cessation of carbon dioxide emissions". In: *Nature Geoscience* 4.2, pp. 83–87.
- Gilman, Paul (2015). *SAM photovoltaic model technical reference*. Tech. rep. National Renewable Energy Lab.(NREL), Golden, CO (United States).
- Gostein, Michael, J Riley Caron, and Bodo Littmann (2014). "Measuring soiling losses at utility-scale PV power plants". In: 2014 IEEE 40th Photovoltaic Specialist Conference (PVSC). IEEE, pp. 0885–0890.
- Gostein, Michael, Tim Düster, and Christopher Thuman (2015). "Accurately measuring PV soiling losses with soiling station employing module power measurements". In: 2015 IEEE 42nd Photovoltaic Specialist Conference (PVSC). IEEE, pp. 1–4
- Gostein, Michael et al. (2013). "Comparing PV power plant soiling measurements extracted from PV module irradiance and power measurements". In: 2013 IEEE 39th Photovoltaic Specialists Conference (PVSC). IEEE, pp. 3004–3009.
- Gostein, Michael et al. (2016). "Soiling measurement station to evaluate anti-soiling properties of PV module coatings". In: 2016 IEEE 43rd Photovoltaic Specialists Conference (PVSC). IEEE, pp. 3129–3131.
- Gostein, Michael et al. (2018). "Mars soiling sensor™". In: 2018 IEEE 7th World Conference on Photovoltaic Energy Conversion (WCPEC)(A Joint Conference of 45th IEEE PVSC, 28th PVSEC & 34th EU PVSEC). IEEE, pp. 3417–3420.
- Gostein, Michael et al. (2019). "Field evaluations of MarsTM optical soiling sensor". In: 2019 46th IEEE Photovoltaic Specialists Conference (PVSC).
- Hamdhan, Indra Noer and Barry G Clarke (2010). "Determination of thermal conductivity of coarse and fine sand soils". In: *Proceedings World Geothermal Congress*. Vol. 2010.
- Hassan, AH et al. (2005). "Effect of airborne dust concentration on the performance of PV modules". In: *J. Astron. Soc. Egypt* 13.1, pp. 24–38.
- He, Kaiming et al. (2016). "Deep residual learning for image recognition". In: *Proceedings of the IEEE conference on computer vision and pattern recognition*, pp. 770–778.
- Heimsath, Anna and Peter Nitz (2019). "The effect of soiling on the reflectance of solar reflector materials-Model for prediction of incidence angle dependent reflectance and attenuation due to dust deposition". In: *Solar Energy Materials and Solar Cells* 195, pp. 258–268.
- Hoang, P et al. (2014). "Coupling optical and thermal models to accurately predict PV panel electricity production". In: *Solar energy materials and solar cells* 125, pp. 325–338.

Holmgren, William F, Clifford W Hansen, and Mark A Mikofski (2018). "pvlib python: A python package for modeling solar energy systems". In: *Journal of Open Source Software* 3.29, p. 884.

- Holmgren, William F et al. (2015). "PVLIB python 2015". In: 2015 ieee 42nd photovoltaic specialist conference (pvsc). IEEE, pp. 1–5.
- IEA (Oct. 2024). Renewables 2024. https://www.iea.org/reports/renewables-2024.
- IEA-PVPS (2024). *Snapshot of Global PV Markets*. Tech. rep. International Energy Agency Photovoltaic Power Systems Programme.
- IEC, Crystalline Silicon Terrestrial Photovoltaic (2005). *Modules—Design Qualification and Type Approval*.
- Ilse, Klemens et al. (2019). "Techno-economic assessment of soiling losses and mitigation strategies for solar power generation". In: *Joule* 3.10, pp. 2303–2321.
- Ilse, Klemens K et al. (2018). "Fundamentals of soiling processes on photovoltaic modules". In: *Renewable and Sustainable Energy Reviews* 98, pp. 239–254.
- Jamil, Wan Juzaili et al. (2017). "Performance degradation of photovoltaic power system: Review on mitigation methods". In: *Renewable and Sustainable Energy Reviews* 67, pp. 876–891.
- Jessen, Wilko et al. (2018). "Proposal and evaluation of subordinate standard solar irradiance spectra for applications in solar energy systems". In: *Solar Energy* 168, pp. 30–43.
- Kandeal, AW et al. (2021). "Infrared thermography-based condition monitoring of solar photovoltaic systems: A mini review of recent advances". In: *Solar Energy* 223, pp. 33–43.
- Karimi, Ahmad Maroof et al. (2020). "Generalized and mechanistic PV module performance prediction from computer vision and machine learning on electroluminescence images". In: *IEEE Journal of Photovoltaics* 10.3, pp. 878–887.
- Karki, Sameep (2019). "Characterization, Calibration and Validation of DustIQ PV cells as Sensor for PV Usable Light". In.
- Kimber, Adrianne et al. (2006). "The effect of soiling on large grid-connected photovoltaic systems in California and the southwest region of the United States". In: 2006 IEEE 4th World Conference on Photovoltaic Energy Conference. Vol. 2. IEEE, pp. 2391–2395.
- King, David L, Jay A Kratochvil, and William Earl Boyson (2004). *Photovoltaic array performance model*. Vol. 8. Citeseer.
- Kipp & Zonen (2024). DustIQ Soiling Monitoring System. URL: https://www.kippzonen.com/Product/419/DustIQ-Soiling-Monitoring-System (visited on 09/30/2024).
- Kirillov, Alexander et al. (2023). "Segment anything". In: *Proceedings of the IEEE/CVF International Conference on Computer Vision*, pp. 4015–4026.
- Knutti, Reto and Joeri Rogelj (2015). "The legacy of our CO 2 emissions: a clash of scientific facts, politics and ethics". In: *Climatic Change* 133, pp. 361–373.
- Korevaar, Marc et al. (2017). "Novel soiling detection system for solar panels". In: 33rd European Photovoltaic Solar Energy Conference and Exhibition, pp. 2349–2351.
- Kreith, Frank and Jan F Kreider (1978). "Principles of solar engineering". In.
- Krizhevsky, A (2012). "Imagenet classification with deep convolutional neural networks/Alex Krizhevsky, Ilya Sutskever, Geoffrey E. Hinton". In: *NIPS.*—2012.—1106—1114 p.
- Kuhn, Pascal et al. (2017). "Shadow camera system for the generation of solar irradiance maps". In: *Solar Energy* 157, pp. 157–170.
- Lamaamar, Ibtissam et al. (2021). "Evaluation of different models for validating of photovoltaic cell temperature under semi-arid conditions". In: *Heliyon* 7.12.

Lee, B et al. (2008). "Thermally conductive and electrically insulating EVA composite encapsulants for solar photovoltaic (PV) cell". In: *Express Polym Lett* 2.5, pp. 357–363.

- Li, Chuyi et al. (2022). "YOLOv6: A single-stage object detection framework for industrial applications". In: *arXiv* preprint *arXiv*:2209.02976.
- Li, Xiaoxia et al. (2017). "Visible defects detection based on UAV-based inspection in large-scale photovoltaic systems". In: *IET Renewable Power Generation* 11.10, pp. 1234–1244.
- Lorenz, Andreas et al. (2017). "High-throughput front and rear side metallization of silicon solar cells using rotary screen printing". In: *Energy Procedia* 124, pp. 680–690.
- MacDougall, Andrew H et al. (2015). "Sensitivity of carbon budgets to permafrost carbon feedbacks and non-CO2 forcings". In: *Environmental Research Letters* 10.12, p. 125003.
- Martin-Sanchez, Pedro M et al. (2018). "Monitoring microbial soiling in photovoltaic systems: A qPCR-based approach". In: *International biodeterioration & biodegradation* 129, pp. 13–22.
- Matthews, H Damon and Ken Caldeira (2008). "Stabilizing climate requires near-zero emissions". In: *Geophysical research letters* 35.4.
- Matthews, H Damon et al. (2009). "The proportionality of global warming to cumulative carbon emissions". In: *Nature* 459.7248, pp. 829–832.
- Mehta, Sachin et al. (2018). "Deepsolareye: Power loss prediction and weakly supervised soiling localization via fully convolutional networks for solar panels". In: 2018 IEEE Winter Conference on Applications of Computer Vision (WACV). IEEE, pp. 333–342.
- Mesbahi, M (2018). White paper-soiling: the science & solutions.
- *Module data sheet* (2024). JAM72S09 375-395/PR. JA Solar.
- Mondal, Surajit et al. (2018). "An overview of cleaning and prevention processes for enhancing efficiency of solar photovoltaic panels". In: *Current Science* 115.6, pp. 1065–1077.
- National Oceanic and Atmospheric Administration (1976). *US Standard Atmosphere* 1976. National Oceanic and Atmospheric Administration.
- Notton, Gilles et al. (2005). "Modelling of a double-glass photovoltaic module using finite differences". In: *Applied thermal engineering* 25.17-18, pp. 2854–2877.
- Oliveira, Michele Cândida Carvalho de et al. (2018). "The causes and effects of degradation of encapsulant ethylene vinyl acetate copolymer (EVA) in crystalline silicon photovoltaic modules: A review". In: *Renewable and Sustainable Energy Reviews* 81, pp. 2299–2317. ISSN: 1364-0321. DOI: https://doi.org/10.1016/j.rser.2017.06.039. URL: https://www.sciencedirect.com/science/article/pii/S1364032117309851.
- Pavan, A Massi, Adel Mellit, and D De Pieri (2011). "The effect of soiling on energy production for large-scale photovoltaic plants". In: *Solar energy* 85.5, pp. 1128–1136.
- Peterson, Josh, Julie Chard, and Justin Robinson (2022). "Extraction of Prevailing Soiling Rates from Soiling Measurement Data". In: 2022 IEEE 49th Photovoltaics Specialists Conference (PVSC). IEEE, pp. 0684–0691.
- Pfreundt, A et al. (2019). "Post-processing thickness variation of PV module materials and its impact on temperature, mechanical stress and power". In.
- Prahl, Christoph (2019). "Photogrammetric measurement of the optical performance of parabolic trough solar fields". PhD thesis. RWTH Aachen.

Priyadarshini, B Geetha and Ashok Kumar Sharma (2016). "Design of multi-layer anti-reflection coating for terrestrial solar panel glass". In: *Bulletin of Materials Science* 39, pp. 683–689.

- Qasem, Hassan, Ashot Mnatsakanyan, and Pedro Banda (2016). "Assessing dust on PV modules using image processing techniques". In: 2016 IEEE 43rd Photovoltaic Specialists Conference (PVSC). IEEE, pp. 2066–2070.
- Qasem, Hassan et al. (2014). "Dust-induced shading on photovoltaic modules". In: *Progress in Photovoltaics: Research and Applications* 22.2, pp. 218–226.
- Qian, Jiadong et al. (2018). "Comparison of half-cell and full-cell module hotspot-induced temperature by simulation". In: *IEEE Journal of Photovoltaics* 8.3, pp. 834–839.
- Quaschning, Volker (2008). Regenerative Energiesysteme: Technologie-Berechnung-Simulation; mit 97 Tabellen und einer DVD. Hanser Verlag.
- Redmon, Joseph and Ali Farhadi (2017). "YOLO9000: better, faster, stronger". In: *Proceedings of the IEEE conference on computer vision and pattern recognition*, pp. 7263–7271.
- (2018). "Yolov3: An incremental improvement". In: arXiv preprint arXiv:1804.02767.
 Redmon, Joseph et al. (2016). "You only look once: Unified, real-time object detection".
 In: Proceedings of the IEEE conference on computer vision and pattern recognition, pp. 779–788.
- Restrepo-Cuestas, Bonie Johana and Jhon Montano (2024). "Bishop model parameter estimation in photovoltaic cells using metaheuristic optimization techniques". In: *Solar Energy* 270, p. 112410.
- Restrepo-Cuestas, Bonie Johana et al. (2022). "Parameter estimation of the bishop photovoltaic model using a genetic algorithm". In: *Applied Sciences* 12.6, p. 2927.
- Ross, RG (1981). "Design techniques for flat-plate photovoltaic arrays". In: *Proceedings of the 15th Photovoltaic Specialists Conference, Orlando, FL, USA*, pp. 12–15.
- Rossi, Daniele et al. (2014). "Modeling and detection of hotspot in shaded photovoltaic cells". In: *IEEE Transactions on Very Large Scale Integration (VLSI) Systems* 23.6, pp. 1031–1039.
- Rubio, E, Vicente Caselles, and Conrado Badenas (1997). "Emissivity measurements of several soils and vegetation types in the 8–14, μ m Wave band: Analysis of two field methods". In: *Remote Sensing of Environment* 59.3, pp. 490–521.
- Sayyah, Arash, Mark N Horenstein, and Malay K Mazumder (2014). "Energy yield loss caused by dust deposition on photovoltaic panels". In: *Solar Energy* 107, pp. 576–604.
- Shirakawa, Marcia A et al. (2015). "Microbial colonization affects the efficiency of photovoltaic panels in a tropical environment". In: *Journal of environmental management* 157, pp. 160–167.
- Siebers, Dennis Lee (1983). Experimental mixed convection heat transfer from a large, vertical surface in a horizontal flow. Stanford University.
- Simonyan, Karen and Andrew Zisserman (2014). "Very deep convolutional networks for large-scale image recognition". In: *arXiv* preprint arXiv:1409.1556.
- Skoplaki, EPJA and John A Palyvos (2009). "Operating temperature of photovoltaic modules: A survey of pertinent correlations". In: *Renewable energy* 34.1, pp. 23–29.
- Smestad, Greg P et al. (2020). "Modelling photovoltaic soiling losses through optical characterization". In: *Scientific reports* 10.1, p. 58.
- Solheim, Hans J et al. (2013). "Measurement and simulation of hot spots in solar cells". In: *Energy Procedia* 38, pp. 183–189.

Sutha, S et al. (2017). "Transparent alumina based superhydrophobic self–cleaning coatings for solar cell cover glass applications". In: *Solar Energy Materials and Solar Cells* 165, pp. 128–137.

- Szeliski, Richard (2022). *Computer vision: algorithms and applications*. Springer Nature. Tang, Wuqin et al. (2020). "Deep learning based automatic defect identification of photovoltaic module using electroluminescence images". In: *Solar Energy* 201, pp. 453–460.
- The SciPy community (2024). scipy.optimize.fsolve. URL: https://docs.scipy.org/doc/scipy/reference/generated/scipy.optimize.fsolve.html (visited on 07/29/2024).
- Tool, CJJ et al. (2002). "Influence of wafer thickness on the performance of multicrystalline Si solar cells: an experimental study". In: *Progress in Photovoltaics: Research and Applications* 10.4, pp. 279–291.
- Toolbox, The Engineering (2003). Surface Emissivity Coefficients. URL: https://www.engineeringtoolbox.com/emissivity-coefficients-d_447.html (visited on 06/14/2024).
- (2011). Plastics thermal Conductivity Coefficients. URL: https://www.engineeringtoolbox.com/thermal-conductivity-plastics-d_1786.html (visited on 06/14/2024).
- Townsend, T and P Hutchinson (2000). "Soiling analyses at PVUSA". In: *Proceedings of the Solar Conference*. American Solar Energy Society; American Institute of Architects, pp. 417–422.
- Valerino, Michael et al. (2020). "Low-cost solar PV soiling sensor validation and size resolved soiling impacts: A comprehensive field study in Western India". In: *Solar energy* 204, pp. 307–315.
- Vumbugwa, M et al. (2020). "Effects of current mismatch due to uneven soiling on the performance of multi-crystalline silicon module strings". In: *Journal of Energy in Southern Africa* 31.1, pp. 62–72.
- Wang, Chien-Yao, Alexey Bochkovskiy, and Hong-Yuan Mark Liao (2023). "YOLOv7: Trainable bag-of-freebies sets new state-of-the-art for real-time object detectors". In: *Proceedings of the IEEE/CVF conference on computer vision and pattern recognition*, pp. 7464–7475.
- Wendlandt, Stefan et al. (2010). "Hot spot risk analysis on silicon cell modules". In: 25th European Photovoltaic Solar Energy Conference and Exhibition. Valencia, Spain, pp. 4002–4006.
- Wilbert, Stefan (2009). "Weiterentwicklung eines optischen Messsystems zur Bestimmung der Formabweichungen von Konzentratoren solarthermischer Kraftwerke unter dynamischem Windeinfluss". PhD thesis. DLR/Universität Bonn.
- Winkel, Peter et al. (2024a). "Cell-Resolved PV Soiling Measurement Using Drone Images". In: *Remote Sensing* 16.14, p. 2617.
- Winkel, Peter et al. (2024b). "Electrothermal Modeling of Photovoltaic Modules for the Detection of Hot-Spots Caused by Soiling". In: *Energies* 17.19. ISSN: 1996-1073. DOI: 10.3390/en17194878. URL: https://www.mdpi.com/1996-1073/17/19/4878.
- Winter, S, D Friedrich, and A Sperling (2009). "Effects of the new standard IEC 60904-3: 2008 on the calibration results of common solar cell types". In: 24th European Photovoltaic Solar Energy Conference, pp. 21–25.
- Wolf, A, P Pohl, and R Brendel (2005). "Determination of thermophysical properties of thin films for photovoltaic applications". In: *Conference Record of the Thirty-first IEEE Photovoltaic Specialists Conference*, 2005. IEEE, pp. 1749–1752.
- Wolfertstetter, Fabian et al. (2021). "Incidence angle and diffuse radiation adaptation of soiling ratio measurements of indirect optical soiling sensors". In: *Journal of Renewable and Sustainable Energy* 13.3.

Xu, Chenyang et al. (2020). "Surface soil temperature seasonal variation estimation in a forested area using combined satellite observations and in-situ measurements". In: *International Journal of Applied Earth Observation and Geoinformation* 91, p. 102156.

- Yang, Hong et al. (2010). "Investigation of reverse current for crystalline silicon solar cells—New concept for a test standard about the reverse current". In: 2010 35th IEEE Photovoltaic Specialists Conference. IEEE, pp. 002806–002810.
- Yang, Mingda, Jim Ji, and Bing Guo (2020a). "An image-based method for soiling quantification". In: 2020 IEEE International Conference on Informatics, IoT, and Enabling Technologies (ICIoT). IEEE, pp. 89–94.
- (2020b). "Soiling quantification using an image-based method: Effects of imaging conditions". In: *IEEE Journal of Photovoltaics* 10.6, pp. 1780–1787.
- (2021). "Image-Based PV Soiling Loss Quantification under Laboratory Conditions". In: 2021 IEEE 48th Photovoltaic Specialists Conference (PVSC). IEEE, pp. 2264–2269.
- Yang, Mingda et al. (2024). "Estimating PV Soiling Loss Using Panel Images and a Feature-Based Regression Model". In: *IEEE Journal of Photovoltaics*.
- Yap, Wai Kean, Roy Galet, and Kheng Cher Yeo (2015). "Quantitative analysis of dust and soiling on solar pv panels in the tropics utilizing image-processing methods". In: *Asia-Pacific Solar Research Conference*.
- Yfantis, E and Ahmad Fayed (2014). "A camera system for detecting dust and other deposits on solar panels". In: *Advances in Image and Video Processing* 2.5, pp. 1–10.
- Zhang, Aston et al. (2021). "Dive into deep learning". In: arXiv preprint arXiv:2106.11342.
- Zheng, Daolan, E Raymond Hunt Jr, and Steven W Running (1993). "A daily soil temperature model based on air temperature and precipitation for continental applications". In: *Climate Research* 2.3, pp. 183–191.
- Zhou, Jicheng et al. (2015). "Temperature distribution of photovoltaic module based on finite element simulation". In: *Solar Energy* 111, pp. 97–103.
- Zorrilla-Casanova, J et al. (2011). "Analysis of dust losses in photovoltaic modules". In: *World renewable energy congress*. Linköping University Electronic Press Linköping, Sweden, pp. 2985–2992.